A PDE-Based 3D Approach to In-Flight Ice Accretion

Héloïse Beaugendre

Department of Mechanical Engineering

McGill University

Montreal, Québec

June 2003

A thesis submitted to McGill University in partial fulfillment of the requirements of the degree of Doctor of Philosophy.

A mes parents et à Alexis

Remerciements

J'exprime toute ma gratitude au Professeur Wagdi G. Habashi qui m'a accueillie au sein de l'équipe du CFD Lab de l'université McGill pendant mon stage de DEA et plus tard m'a offert l'opportunité de réaliser cette thèse. Ses suggestions, sa compétence scientifique et l'intérêt apportés à mon travail ont guidé cette étude sur le givrage en vol.

Je remercie les entreprises Pratt & Whitney Canada et Bombardier Aéronautique (NSERC-J. Armand Bombardier Industrial Research Chair of Multidisciplinary CFD) pour le soutien financier apporté à ce projet.

J'adresse mes remerciements au Dr. François Morency pour l'aide apportée à l'encadrement de ce travail. Sa disponibilité et ses conseils ont été de précieux atouts qui ont permis la réalisation de ce projet.

Je n'aurais pu mener à bien mon travail sur la turbulence sans les nombreux conseils de Monsieur Spalart concernant l'implémentation de son modèle.

Un gros merci à toutes les personnes qui ont pris la peine de relire ce document, et qui par leurs discussions éclairées ont permis l'avancement de ce travail.

Je ne voudrais surtout pas oublier toute l'équipe du CFD Lab et de Newmerical Technologies qui ont fait de cette expérience un moment agréable et enrichissant.

Abstract

Each year, sudden aircraft performance degradation due to ice accretion causes several incidents and accidents. Icing is a serious and not yet totally mastered meteorological hazard due to supercooled water droplets (liquid water droplets at a temperature below the dew point) that impact on aerodynamic surfaces. Icing results in performance degradations including substantial reduction of engine performance and stability, reduction in maximum lift and stall angle and an increase of drag.

A realistic ice accretion simulation is achieved if the three contributing factors: the aerodynamic flow field, the water droplet trajectories, and the thermodynamic ice accretion process, are accurately modeled. A new approach to in-flight icing analysis is formulated and validated into this work. The methodology presented in this thesis is intended to be based on modern CFD algorithms to develop a useable new ice accretion tool for aircraft and engines, including: the solution of the 3D compressible turbulent Navier-Stokes equations; the computation of the collection efficiency by an Eulerian method; and a new module for the three-dimensional ice accretion process.

To successfully complete the work, an appropriate turbulence model has been added to the existing flow solver. Therefore a part of this work has been the implementation and validation of the Spalart-Allmaras model. This turbulence model appeared to be robust and easy to use even in situation of complex 3D flow patterns encountered in icing.

The new ice accretion model is expressed with mass and heat transfer balance at the aerodynamic surface using partial differential equations and four compatibility relations to close the system. An appropriate numerical scheme based on finite volume method is derived to solve the resulting system. 2D and 3D validations of the complete in-flight system (dry air flow field/droplets/ice accretion) conclude this work.

Résumé

De nombreux accidents aéronautiques sont provoqués, chaque année, par des phénomènes liés au givrage. Lorsqu'un aéronef traverse un nuage d'eau surfondue (eau liquide à une température sous le point de congélation), il peut se former du givre sur les parties sensibles de l'appareil. Le givrage induit une détérioration des performances aérodynamiques et peut provoquer la perte de contrôle de l'appareil.

Un code numérique de simulation du givrage est généralement composé de trois modules : un module de calcul de l'écoulement d'air autour de la structure ; un module de calcul de l'impact des gouttelettes sur la surface ; et un module thermodynamique de calcul de l'accumulation de glace proprement dit. Le travail présenté dans cette thèse propose d'utiliser les techniques modernes en simulation numérique de la dynamique des fluides afin de développer une nouvelle génération de codes de givrage. Cette méthodologie innovatrice est basée sur la résolution des équations de Navier et Stokes en régime turbulent pour le calcul de l'écoulement d'air, le calcul du coefficient d'impact des gouttelettes par une approche eulérienne, et la création d'un nouveau modèle tridimensionnel d'accumulation de la glace.

Afin de rendre cette approche opérationnelle le modèle de turbulence à une équation, Spalart-Allmaras, a été rajouté au code Navier et Stokes déjà existant. Après validations, il s'avère que ce modèle robuste se prête bien aux conditions exigeantes rencontrées en givrage.

L'élaboration du nouveau module d'accrétion de glace se fait à l'aide de deux équations aux dérivées partielles. La première exprimant la conservation de la masse et la deuxième la conservation de l'énergie. Quatre relations de compatibilité, exprimées sous la forme d'inégalités, ferment le problème. Un schéma numérique approprié basé sur la méthode des volumes finis est proposé pour résoudre le système obtenu. Des validations 2D et 3D de la chaîne de givrage (écoulement/gouttes/glace) complètent le travail.

Table of contents

List of Symbols

Latin Alphabet

c	Length of the chord [m]
c_f	Friction coefficient
c_p	Pressure coefficient at the wall
$c_{p,a}$	Specific heat capacity of air [W.s/(kg.K)]
$c_{p,w}$	Specific heat capacity of water [W.s/(kg.K)]
$c_{p,ice}$	Specific heat capacity of ice [W.s/(kg.K)]
d	Droplet diameter [m]; Distance to wall in chapter 3 [m]
f	Freezing fraction
$\vec{g}$	Gravity vector [m/s^2]
h_c	Convective heat transfer coefficient [W/(m^2.K)]
h_f	Water film thickness [m]
h_i	Value of h_f at node i [m]
i	Enthalpy [J/kg]
k	Thermal conductivity of air [W/(m.K)]
k_s	Equivalent sand-grain roughness [m]
k_s^+	Non-dimensional equivalent sand-grain roughness $k_s^+ = k_s u_\tau / \nu$

$k_s / c)_{base}$	LEWICE empirical coefficient to compute the equivalent sand-grain roughness, $k_s / c)_{base}$ is set to 0.00117
l	Characteristic length [m]
m_d	Mass of the droplet [kg]
$\dot{m}_w$	Water flux at the aerodynamic surface $\dot{m}_w = LWC\, U_\infty\, \beta$ [kg/(m^2.s)]
$\dot{m}_{evap}$	Mass flux of evaporation [kg/(m^2.s)]
$\dot{m}_{ice}$	Mass flux of accumulation of ice [kg/(m^2.s)]
$\dot{m}_i$	Mass flux of accumulation of ice at node i [kg/(m^2.s)]
$\dot{m}_\beta$	Mass flux of impacted water [kg/(m^2.s)]
$\vec{n}$	Normal to the aerodynamic surface
s	Curvilinear distance from stagnation point [m]
$\vec{u}_a$	Non-dimensional velocity of air
$\vec{u}_d$	Droplet impact velocity [m/s]
$\vec{u}_f$	Liquid water film velocity [m/s]
$\bar{u}_f$	Average liquid water film [m/s]
u_i	Component i of the velocity, i=1,2,3 [m/s]
u_τ	Friction velocity [m/s]
u^+	Non-dimensional velocity in wall coordinates
$vol(C_i)$	Volume (in the sense of finite volume scheme) of cell C_i [m^2]
y^+	Non-dimensional distance from wall coordinates
A_d	Characteristic area of the droplet [m^2]

AoA	Aerodynamic angle of attack
B	Coefficient, Chapter 3
C_D	Drag coefficient
H	Total enthalpy [J/kg]
$H_{r,\infty}$	Relative humidity
$\vec{J}$	Jacobian matrix
L_{evap}	Latent heat of evaporation [J/kg]
L_{sub}	Latent heat of sublimation [J/kg]
L_{fus}	Latent heat of fusion [J/kg]
LWC	Liquid water content [kg/m^3]
$\mathrm{M}_{m(air)}$	Molar mass of air [kg/mole]
$\mathrm{M}_{m(water)}$	Molar mass of water [kg/mole]
M_∞, Ma	Mach number at freestream
MVD	Mean Volume Diameter [m]
N	Shape function
$P_{v,p}$	Saturation vapor pressure at the surface [Pa]
$P_{v,\infty}$	Saturation vapor pressure of water in ambient air [Pa]
P_{wall}	Absolute pressure above the control volume outside the boundary layer [Pa]
$\dot{Q}_{cond}$	Conductive heat flux [W/m^2]
$\dot{Q}_{conv}$	Convective heat flux [W/m^2]

$\dot{Q}_{evap}$	Evaporative heat flux [W/m^2]
$\dot{Q}_h$	Convective heat flux [W/m^2]
$\dot{Q}_{rad}$	Radiative heat flux [W/m^2]
$\dot{Q}_\beta$	Kinematic heat flux from impacting droplets[W/m^2]
R	Radius of a cylinder [m]
S	Magnitude of the vorticity [1/s], Chapter 3; Curvilinear surface [m^2], Chapter 4
$\tilde{S}$	Modified magnitude of vorticity [1/s]
T	Temperature [K]; Equilibrium temperature within the air/water film/ice/wall interface [K], Chapter 4
$\tilde{T}$	Equilibrium temperature within the air/water film/ice/wall interface [^{o}C]
$\tilde{T}_i$	Value of $\tilde{T}$ at node i [^{o}C]
T_c	Freezing point [$T_c = 273.15K$]
T_r	Recovery temperature [K]
T_w	Wall temperature [K]
T_∞	Freestream temperature [K]
$\tilde{T}_{d,\infty}$	Droplets temperature at freestream [^{o}C]
U	Maximum velocity in the pipe [m/s]
U_∞, V_∞	Freestream air velocity [m/s]
V	Turbulent Navier-Stokes vector of unknowns
$\vec{V}_r$	Droplet velocity relative to the fluid velocity [m/s]

W	Weight function

Greek Alphabet

α	Ratio of the volume occupied by water over the total volume of the fluid element
β	Local collection efficiency
β_{TOT}	Total collection efficiency
γ	Ratio of specific heat
$\vec{\gamma}_d$	Droplet acceleration vector [m/s^2]
γ_j	Mass-diffusion coefficient for substance j in a mixture [kg/(m.s)]
δ	Boundary layer thickness [m]
σ	Boltzman constant [$=5.670\times10^{-8}$ W/(m^2.K^4)]
ε	Solid emissivity, Chapter 4; Artificial viscosity parameter, Chapter 3
κ	von Karman constant
θ	Momentum thickness [m]
μ	Dynamic viscosity coefficient [kg/(s.m)]
ν	Kinetic viscosity [m^2/s]
ν_T	Turbulent Kinetic viscosity [m^2/s]
$\tilde{\nu}$	Dimensionless turbulent viscosity
ρ	Density [kg/m^3]
ρ_a	Density of air [kg/m^3]
ρ_{ice}	Density of ice [kg/m^3]

ρ_w	Density of water [kg/m^3]
$\vec{\tau}_{wall}$	Local wall shear stress tensor [N/m^2]

Characteristic Numbers

Fr	Froude number	$Fr = \frac{U_\infty}{\sqrt{l\, g_0}}$
K	Inertia parameter	$K = \frac{\rho\, d^2 U_\infty}{18 l \mu}$
Le	Lewis number	$Le = \frac{\mathrm{Pr}}{S_c}$
Pr_∞	Prandtl number	$\mathrm{Pr}_\infty = \frac{\mu_\infty c_{p\infty}}{k_\infty}$
Re_∞	Reynolds number	$\mathrm{Re}_\infty = \frac{\rho_\infty l_\infty U_\infty}{\mu_\infty}$
Re_d	Droplet Reynolds number	$\mathrm{Re}_d = \frac{\rho d U_\infty \lvert \vec{u}_a - \vec{u}_d \rvert}{\mu}$
Re_k	Local roughness Reynolds number	$\mathrm{Re}_k = \frac{u_k k_s}{\nu}$
Re_θ	Reynolds number based on θ	$\mathrm{Re}_\theta = \frac{u_e \theta}{\nu}$
S_c	Schmidt number	$S_c = \frac{\mu}{\gamma_j}$

Subscripts

d	Droplet
e	Edge of the boundary layer

f	Liquid water film
sur	Surface conditions
$,t$	Turbulence trip term
$tran$	Transition
T	Turbulent
w	Water
∞	Freestream value

List of Figures

List of Tables

Introduction

When an aircraft/helicopter/UAV or any other flying object traverses a cloud containing supercooled water droplets (liquid water droplets at a temperature below the dew point), ice may accrete on its surface, figure 0.1. Although the problem has been recognized since the Wright Brothers first flew, each year sudden aircraft performance degradation due to ice accretion still causes several incidents and accidents[1]. Experiments conducted in icing tunnels indicate that for the same geometry, depending on speed and altitude, ice can accrete in many different places and with a wide variety of shapes and surface roughness. The amount and shape of ice accreting depend on several factors: the droplets mean diameter and size distribution, the cloud's Liquid Water Content (LWC), the ambient temperature, the instantaneous shape of the aircraft (slat, flap, ailerons deflected), the speed of the aircraft, its altitude and the time and intermittency of the exposure.

When supercooled water droplets hit the aircraft, a range of icing types[2] may occur, figure 0.2. At very low temperatures, droplets will instantaneously freeze on contact with the surface, leading to rime ice with shapes that are still "quite aerodynamic" but with a rough surface. The other extreme occurs when the temperature is near the freezing point of water. In this case, liquid water and ice melt on the structure and form glaze ice ("horns", "lobster tails") that tends to substantially distort the aerodynamic profile of the wing. Both types of ice could be present on the same aircraft at different locations, and both types severely degrade aerodynamic performance, the first by sapping the flow's energy and the second by separating the flow. In between these two extremes, other ice accretions are labeled mixed-ice.

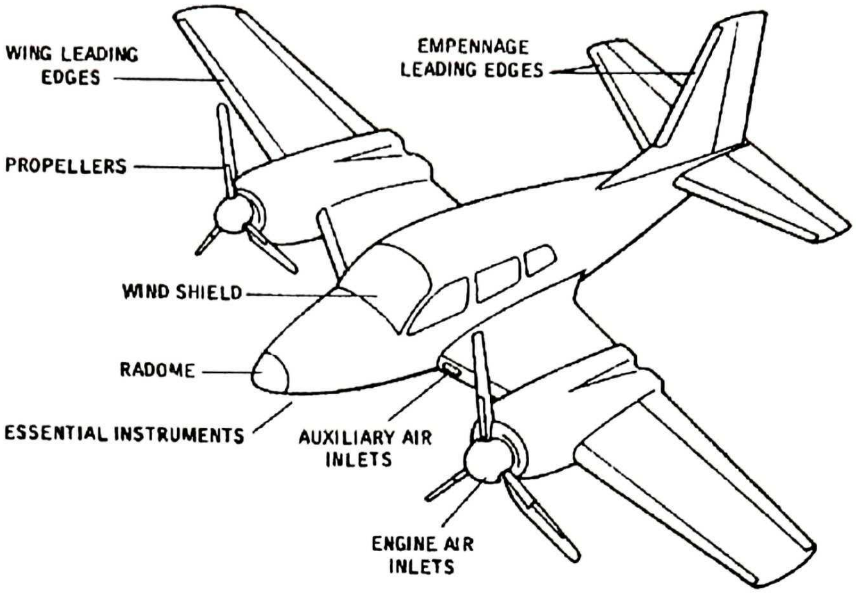

Figure 0.1: Area of the aircraft that may require ice protection, source: FAA, Technical Report ADS-4, December 1963.

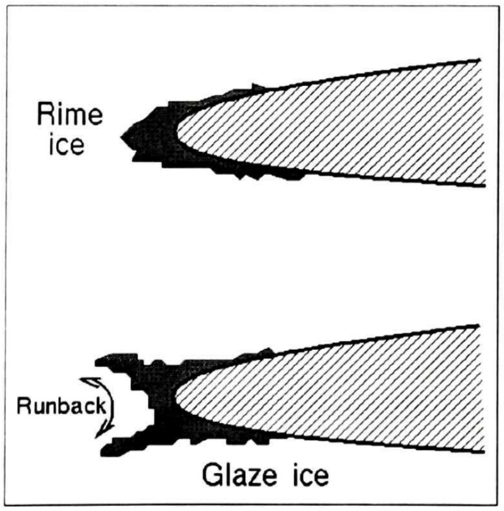

Figure 0.2: Range of icing types that may occur when supercooled water droplets hit the aircraft.

Because of the enormous amounts of thermal or mechanical energy that would be required, complete prevention of ice formation or its complete removal, is not economically feasible. Furthermore anti- or de-icing hot air, bled from engines, is often needed during climb, when the diversion of this power can least be afforded especially for smaller aircraft. Therefore, in practice, some areas of the aircraft are anti-iced, some are only de-iced and a large part is left unprotected.

In-flight ice accretion can be minimized or prevented by[3, 4]:

- Chemical systems: chemical systems (antifreeze) lower the freezing point of water so that it will not freeze.
- Mechanical de-icing:
    - Pneumatic boots: the ice accreted is removed cyclically by using pneumatic boots made of a flexible, rubber-like material, which, when inflated, breaks the ice off the surface. This is mostly used on turboprops and on the leading edge of some engine nacelles. Boots have problems removing small amounts of ice.
    - Pneumatic impulse devices: work on the same principle as pneumatic boots, while eliminating the problem of small amount of ice by using a number of small tubes instead of one large one. These devices are built into the aircraft during construction and work by flexing the metal surface using air.
    - Electroimpulse: a series of electromagnets are pulsed in cycles, flexing the metal surface. These systems may cause problems with metal fatigue.
    - Electro expulsive: An electric current runs through parallel layers of flat, copper ribbon. A repelling magnetic field is created, causing a high

acceleration to break the ice into tiny particles that fall from the airplane's surface.

- Thermal anti- or de-icing[5, 6]: ice is melted by heating. If sufficient heat is added to prevent supercooled water droplets from freezing, the process is called anti-icing. If heat is added to melt the ice after freezing, it is called de-icing. The following technologies are used:
  - Piccolo tubes or S- and D-ducts: hot air is taken from the engine's first stage compressor exit and redirected through a piccolo tube encased in the leading edge area to impact onto the leading edge of wings or S- and D-duct to impact the leading edge of nacelles.
  - Electrothermal pad: electrothermal systems use electrical heater elements which are laminated to the surface to be deiced. These heater elements consist of metal ribbons which emit heat when electrical current is passed through them. This ribbon is surrounded by insulation and is covered with top metal layer for protection.

The boot is not an anti-icing device, it is a de-icer. A minimum ice thickness, labeled initial ice, is needed for the boot to be effective before it is ever activated or cycled once more. Moreover, since a boot cannot operate continuously, inter-cycle ice may form, and after each boot cycling residual ice also remains. With thermal de-icers and even mechanical ones the water may runback along the protected surface and freeze further aft on an unprotected part.

While the shape of the ice has considerable impact, observations have shown that even a small amount of ice, depending on location on the aircraft, can result in substantial degraded aerodynamics by reducing maximum lift and stall angle and increasing drag. The influence of roughness is more important[7] in the case of small amounts of ice. Ice shapes that can form between two de-icing cycles or in the case of de-icing system failure are usually composed of small ice protuberances only a few millimeters in thickness but can cause dramatic drag increase, especially on laminar wing airfoils[7].

Given the adverse effects of icing, commercial airplane manufacturers have to demonstrate, through a rigorous and lengthy certification process, that their airplanes can continue safely flying into known-icing conditions. On the other extreme, except for one European and a Russian helicopter, no other helicopter is certified to fly into known icing and pilots are instructed to immediately exit any icing conditions. Certification can be carried out through a combination of flight tests, wind and icing tunnel tests and numerical simulation. Because not all the natural icing conditions required by the certification process can be explored via flight tests, additional tests are performed in dry air with simulated ice shapes obtained from icing tunnel simulations or icing computer codes.

In real operational conditions, ice may accrete with many different shapes, sizes and locations. The challenge facing researchers and aircraft designers is then to be able to predict the physical characteristics of the ice accretion for any ambient conditions (flight and meteorological) and determine which is the worst-case scenario terms of performance degradation. While numerical simulation is known to be cheaper and faster than the least expensive flight test or icing tunnel campaign, it has been highly underused for in-flight icing. Many reasons can be invoked, but a "disconnect" has traditionally existed between the icing and Computational Fluid Dynamics (CFD) communities: none was really interested in the other. In general, the field remains stuck in 2D, non CAD (Computer Aided Design)-based analysis, incompressible and inviscid approaches, with little current capability or upgrade potential to simulate the aerodynamically complex situations that lead to or are caused by the formation of ice.

As an aid to the certification process, such CFD codes are mostly used to predict 2D sectional ice shapes, which are then manufactured from a light material and attached as disposable profiles on the test aircraft to investigate it for stability and control under icing encounters. Such methods, presented in chapter 1, are based on either a 2D or 3D inviscid (incompressible linear potential or Euler) flow codes to compute the airflow solution, on Lagrangian tracking techniques for droplet impingement calculations, and on a 1D model for mass and heat transfer balance at the surface to predict ice shapes. The United States (NASA National Aeronautics and Space Administration)[8], France (ONERA[2] Office National d'Etudes et de Recherches Aérospatiales) and Canada (Bombardier Chair, Ecole Polytechnique[9] and NRC National Research Council Canada, among others) have developed proprietary codes based on these classical approaches. England[10], Italy[11, 12] and other countries are still attempting to develop indigenous codes. The conclusion is that CFD has been underused. One can ensure a more complete coverage of the combined flight and icing envelopes with the help of CFD simulations. CFD can solve the equations of physics of the 3D motion of air and water droplets to:

- Predict flow around the complete aircraft,
- Predict droplet impact regions,
- Predict ice accretion shapes,
- Predict performance degradation.

A new approach to in-flight icing analysis is formulated and validated into this work. This "CFD methodology", developed in chapter 2, is intended to be based on modern CFD algorithms with respect to true geometries (Computer Aided Design, CAD) and be modular. The main objective of this work is thus to develop a useable new ice accretion tool for aircraft and engines, including:

- Models based on partial differential equations, rather than a control volume approach;
- Increased geometric fidelity by solving in 3D;
- Increased flow fidelity by basing the flow on a Navier-Stokes solver;
- Increased modularity, by developing an ice accretion module that can be tacked to any CFD solver, and any impingement analysis.

Already a 3D Navier-Stokes flow solver and a 3D droplet impingement solver have been completed outside of the present thesis. But because ice shapes are strongly influenced by convective heat transfer fluxes, an appropriate turbulence model with transition from laminar to turbulent flow and with roughness representation has to be added to this flow solver. Therefore a part of this work, chapter 3, has been the implementation and validation of the one-equation Spalart-Allmaras model.

A new thermodynamic approach for predicting 3D ice shapes is formulated in chapter 4, including:

- A fully three-dimensional approach to icing;
- A new physical model based on a partial differential equations system for mass and energy conservation;
- An appropriate numerical scheme to solve the system of equations.

The new physical model will be shown to be close to the well-known shallow water equations and will be called SWIM, for Shallow Water Icing Module. In this thesis, the development of SWIM, in the framework of the code ICE3D (ICE3D-SWIM), and its validation, are presented.

Preliminary validation results of this in-flight icing system are presented in chapter 5 and compared to available 2D test cases. In chapter 6, two three-dimensional ice accretion simulations are presented. The results obtained are compared to numerical and/or experimental results when available.

Chapter 1

Background Material

The aim of an in-flight icing accretion code is to accurately predict the ice accretion shapes and their effect(s) when an aircraft flies through a cloud containing supercooled water droplets, freezing rain or freezing drizzle. A realistic[13] simulation is achieved if the three contributing factors: the aerodynamic flow field, the water droplet trajectories, and the thermodynamic ice accretion process, are as accurately modeled as possible. Current icing thermodynamic models are quite similar in that they use the Messinger model and typically follow the same solution structure (figure 1.1):

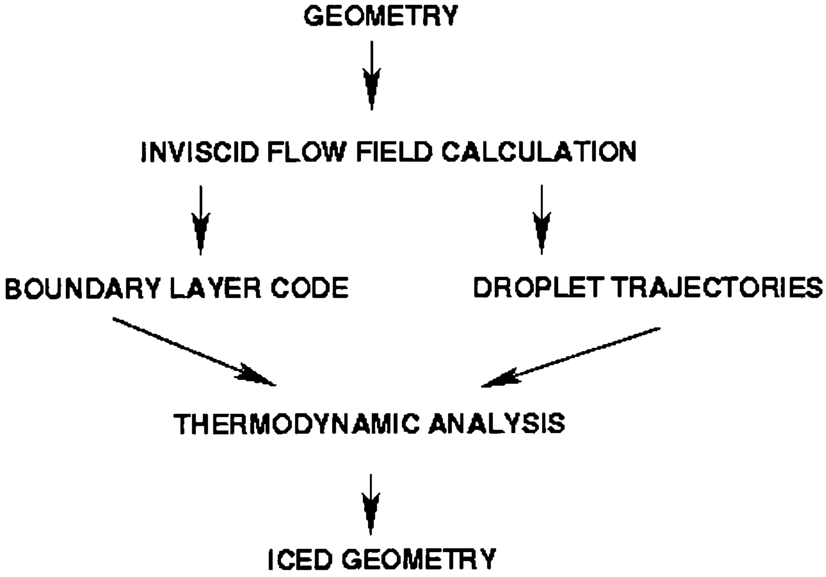

Figure 1.1: Structure of traditional icing codes.

The flow field around the geometry is first calculated enabling the trajectories of the cloud water droplets to be computed. This is used to determine the amount and impact location of water on the surface. Once the collection efficiency has been determined, the next step is to predict whether this water will freeze. For a given temperature, a heat and mass thermodynamic balance over each section of the "meshed" surface geometry will determine the amount of water that will freeze, run back or evaporate within each element. The convective heat transfer is traditionally computed by solving the integral boundary layer equations and using an equivalent sand-grain roughness to account for the roughness of the iced surface. The mass rate of evaporation is then computed using the convective heat transfer coefficient and the saturation vapor pressure at the surface. Thus, an ice profile is gradually obtained from the predicted ice growth rates. The best-known codes using this structure are NASA's LEWICE[14] and the ONERA[15] code, two national codes not available to foreign users, and several proprietary codes that often mimic these two, such as MTRAJ / TRAJICE2 / SPINNICE / ICECREMO[16] (DERA, now QinetiQ), MULTI-ICE / HELICE (CIRA) and CANICE[17] (Bombardier Chair, Ecole Polytechnique). This chapter will serve to describe the classical approaches[18] used by the LEWICE and ONERA codes (which are quite similar except in minor details, and are representative of all other codes) to solve each of these phenomena and serve as an introduction and a justification for the work undertaken in this thesis.

1.1. Flow field determination

The first step in an ice accretion simulation process is the accurate determination of the velocity field. Excluding codes in development, most current ones determine an inviscid flow field, and couple it to a boundary layer code for viscous effects. The inviscid velocity field is obtained by solving either the linear potential flow equation[14-17] (Panel method[19, 20]: incompressible) or the Euler equations[15] (compressible). If the intention is not to limit CFD only to ice shape prediction, then performance degradation becomes an important item. In this case, the most suitable method ought to be able to handle the computation of the flow both around the clean airfoil and over the contaminated one, which may have irregular non-aerodynamic shapes due to ice accretion.

1.1.1. LEWICE

The simplest model to solve an inviscid flow field is the panel method, pioneered by Hess and Smith in the 1960's. Panel methods solve the incompressible, inviscid, irrotational flow and utilize the superposition of fundamental solutions of the linear Laplace equation, based on one or more singularities types such as sources, sinks, doublets and vortices. The panel method first discretizes a body by a finite number of panels (segments in 2D), over each of which acts an unknown singularity value or a distribution. The local potential induced by all singularities is calculated at n control points on the surface with the no-penetration condition used to balance this against the potential induced by the free stream. This results in a $n \times n$ full matrix that is then solved for the unknown strengths of the singularities needed to achieve the no-penetration condition. Special techniques are called for when the system is large, otherwise solution costs get prohibitive. Compressibility corrections (such as the Prandtl-Glauert compressibility correction) up to Mach 0.5 are added to the classical Panel method. While LEWICE was first based on a 2D panel method[14], numerous modified versions are now in use, like three-dimensional[21] version of the panel method (LEWICE3D, in which the flow prediction is 3D, while icing calculations are done in 2D along straight cuts given by the 3D solution). In truth, this can only be called a 2.5D solution, as ice accretion do not account for the spanwise effects. Another version also is in use where the pseudo-viscous field is solved by viscous-inviscid interaction[22] methods, etc.

1.1.2 ONERA code

In the ONERA[15, 23] code, the inviscid flow field might be modeled either by the linear potential flow equation or by the Euler equations. For the first model, a 3D panel method code (ECOPAN) is used with compressibility corrections up to Mach 0.5 (the Prandtl-Glauert compressibility correction). For the Euler equations a 3D finite element method is used. This code requires the creation of a volumetric C-grid. Stabilization is obtained through artificial viscosity and a multigrid method is used for convergence acceleration.

1.1.3 Conclusions: advantages and limitations

Both methods require a "mesh", a skeletal one on the body surface for panel methods, and a volumetric one on the entire domain for the Euler approach.

2D panel methods are very fast and efficient for simple 2D, nearly incompressible, icing calculations. In 3D, however, the on-surface velocity computation is fast, but for out-of-the-surface velocities CPU-time can increase rapidly as all panels must be summed up. Global compressibility corrections can be added to approximately Mach 0.5, but it is not possible to take into account local compressibility effects, say due to the growth of an ice horn.

The Euler method overcomes compressibility limitations, as it is valid for subsonic, transonic and supersonic flows.

However, none of the methods discussed above directly takes into account the viscous effects. If the computation of the boundary layer (described in the following section) allows the representation of most of the viscous effects of the flow, it cannot give an accurate representation when flow is separated. According to experiments, while it is unusual that ice accretes in a region of separation, separation can strongly modify the flow pattern around the geometry and thus modify the impingement, as well as the convective heat transfer distribution on the body, indirectly affecting the ice shape.

Moreover it is not possible to use the same mesh and these inviscid codes to analyze performance degradation due to icing. Usually, to study aerodynamic penalties caused by icing, a new mesh is generated and a Navier-Stokes flow solver is used.

1.2. Boundary layer code[14-17]

The flow field determination, presented in the previous section, is based on inviscid calculations. Therefore the boundary layer equations are subsequently solved, usually in integral form, to determine the convective heat transfer coefficient on the iced geometry. Sometimes the boundary layer code is also coupled with the inviscid code, as in the work initiated by Cebeci[22], to improve accuracy. When ice accretes on a body surface, a surface roughness forms on the body enhancing the convective heat transfer coefficient. It is, therefore, necessary to define a rough wall model to simulate the iced wall effect on the boundary layer. The transition point has to also be determined, as the roughness of the iced geometry acts like a trip from laminar to turbulent flow.

1.2.1. LEWICE

The boundary layer method applied in LEWICE is required to determine the convective heat transfer coefficient in the laminar and turbulent regions and also to detect the transition from laminar to turbulent flow. The equivalent sand-grain roughness is included in the turbulent skin friction coefficient definition and the Reynolds analogy is used to retrieve the convective heat transfer coefficient. The following sections present the equations used in LEWICE[14].

1.2.1.1. Transition point

A boundary layer calculation starts at the stagnation point and considers the flow to be laminar until the boundary layer transition. The criterion for transition over a rough surface, defined by Von Doenhoff[24], presumes that the flow becomes turbulent when the local roughness Reynolds number is greater than 600:

$$\mathrm{Re}_k = \frac{u_k k_s}{\nu} \geq 600 \tag{1.1}$$

where k_s is the equivalent sand-grain roughness height, u_k is the velocity at $y = k_s$. The velocity u_k is defined by the following formula:

$$\frac{u_k}{u_e} = \frac{2k_s}{\delta} - 2\left(\frac{k_s}{\delta}\right)^3 + \left(\frac{k_s}{\delta}\right)^4 + \frac{1}{6}\frac{\delta^2}{\nu}\frac{du_e}{ds}\frac{k_s}{\delta}\left(1 - \frac{k_s}{\delta}\right)^3 \tag{1.2}$$

where δ is the boundary layer thickness. It can be shown that the boundary layer thickness is related to the laminar momentum thickness by:

$$\delta \approx 8.5\theta_l$$

The laminar momentum thickness can be evaluated using the Thwaites[25, p. 315] formula:

$$\theta_l^2 = \frac{0.45}{u_e^6}\int_o^s u_e^5 ds \tag{1.3}$$

where it is assumed that the velocity at the edge of the boundary layer, u_e, is the surface velocity calculated by the potential flow or the Euler equations.

1.2.1.2. Laminar convective heat transfer

If the boundary layer is still laminar at a surface distance s from the stagnation point, the convective heat transfer coefficient is obtained from the following relation by Smith and Spalding[25, pp. 327-329] as:

$$h_c = 0.296\frac{\lambda}{\sqrt{\nu}}\left[u_e^{-2.88}\int_0^s u_e^{1.88}ds\right] \tag{1.4}$$

where λ is the thermal conductivity of air.

1.2.1.3. Turbulent convective heat transfer

If the boundary layer is turbulent at a surface distance s from the stagnation point, the convective heat transfer coefficient is obtained from the Stanton number by:

$$h_c = St\rho u_e c_p \tag{1.5}$$

$$St = \frac{c_f/2}{P_{rt} + \sqrt{c_f/2}\left(1/St_k\right)} \tag{1.6}$$

where $P_{rt} = 0.9$ is the turbulent Prandtl number and St_k is the roughness Stanton number[26] defined as:

$$St_k = 1.156\left[\frac{u_\tau k_s}{\nu}\right]^{-0.2}$$

where the shear velocity is:

$$u_\tau = u_e\sqrt{c_f/2},$$

and the skin friction coefficient is

$$c_f/2 = \frac{0.168}{\left[\ln\left(864\frac{\theta_t}{k_s}\right)\right]^2}.$$

The turbulent momentum thickness is evaluated using:

$$\theta_t = \left[\frac{0.0156}{u_e^{4.11}} \int_{s_{tran}}^{s} u_e^{3.86} ds \right]^{0.8} + \theta_l\left(s_{tran}\right). \tag{1.7}$$

Since one first has a laminar boundary layer, the turbulent boundary layer begins at the transition point, $s = s_{tran}$, and the laminar momentum thickness, already existing, $\theta_l\left(s_{tran}\right)$ given by equation (1.3), must be added.

1.2.1.4. Comment

In 2D, the boundary layer code is built on the same panels used by the inviscid flow calculation. In 3D the approach requires considerably more effort. LEWICE3D[21] computes first the pathlines of the 3D flow and the 2D boundary layer is built on the streamlines of interest.

1.2.2. ONERA code

In the ONERA code[15, 23], the three-dimensional boundary layer equations are calculated using a finite volume code. To improve the boundary layer calculations, the "geometric" grid on which the inviscid flow calculations have been performed has been found too coarse, and ONERA made the grid denser close to the flow singularities, the stagnation lines. Therefore a finer grid (figure 1.2) called the aerodynamic grid is built and used to compute the three-dimensional boundary layer.

The transition caused by roughness is detected using the local roughness Reynolds number, with the same transition criterion as LEWICE given by equation (1.1). The roughness model is, however, different than LEWICE and uses the Van Driest formulation. The increase of the convective heat transfer is modeled by an increase of the smooth wall turbulent shear stress. The turbulent shear stress is expressed using the mixing length formulation:

$$\tau_t = \rho F^2 l_m^2 \left[\left(\frac{\partial u}{\partial y} \right)^2 + \left(\frac{\partial w}{\partial y} \right)^2 \right] \tag{1.8}$$

where the mixing length after Michel *et al.* is defined by:

$$l_m = \delta \kappa_r \tanh\left(\frac{\kappa y}{\kappa_r \delta} \right) \tag{1.9}$$

with $\kappa_r = 0.085$ and $\kappa = 0.41$.

The turbulent damping factor, F, near a smooth wall is:

$$F = 1 - \exp\left(\frac{l_m \sqrt{\tau \rho}}{26 \kappa \mu} \right). \tag{1.10}$$

The roughness effect is simulated by modifying F to reduce its damping effect and increase the turbulent shear stress. The modification is given by the Van Driest roughness model:

$$F = 1 - \exp\left(\frac{l_m \sqrt{\tau \rho}}{26 \kappa \mu} \right) + \exp\left(\frac{60 y}{26 k_s} \right) \tag{1.11}$$

where k_s is still the equivalent sand-grain roughness height.

Using this roughness model, the thermal structure of the boundary layer is obtained and the convective heat transfer coefficient is defined as:

$$h_c = k \left(\frac{\partial T}{\partial y} \right)_{y=0} \Big/ (T_w - T_r) \tag{1.12}$$

where k is the thermal conductivity of air.

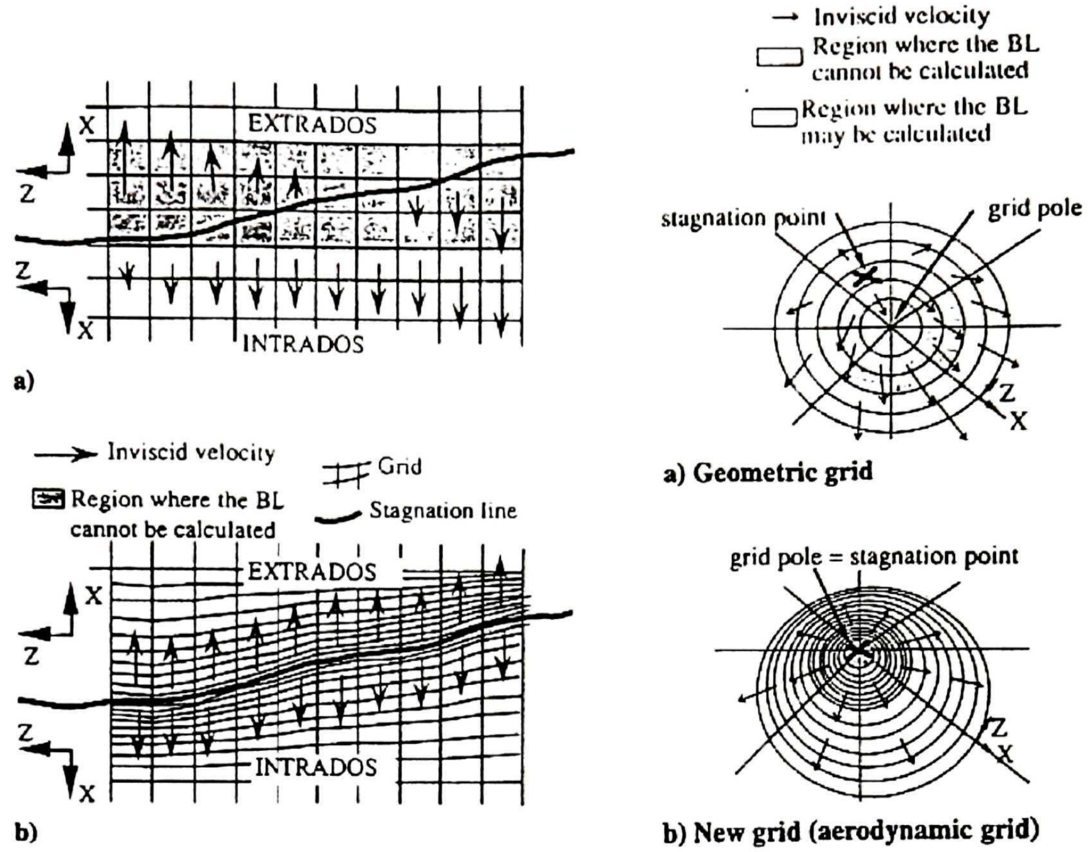

a) Geometric grid

b) New grid (aerodynamic grid)

Figure 1.2[23]: Left side of the figure: ONERA aerodynamic grid on a separation line body (airfoil). X is the curvilinear abscissa along the profile, Z is the span direction. If the boundary layer had to be calculated on a) the geometric grid a large region around the stagnation line would not be calculate; on the contrary b) the aerodynamic grid enables the boundary-layer calculation to start close to the stagnation line.

Right side of the figure: ONERA aerodynamic grid on stagnation point body, nose. Grid pole moves to be coincident with the stagnation point permitting boundary-layer calculation to start as close as wanted to the pole.

1.2.3. Conclusions: advantages and disadvantages

According to Hedde[15], the roughness models used by the LEWICE and ONERA codes give similar satisfactory results for typical roughness heights encountered in icing simulations. However, both models have difficulty predicting the convective heat transfer for high Reynolds numbers.

In 2D, the boundary layer code is solved on the same mesh used by the inviscid flow calculation and the duo (inviscid code + boundary layer) is effective and very fast. In 3D, however, the approach requires, in both icing codes, the computation of the streamlines. The approach in the ONERA code is the creation of yet another grid: the "aerodynamic grid"; while LEWICE3D carries out 2D boundary layer calculations on each streamline of interest.

1.3. Droplet solution

Computing impingement is the second step of an ice simulation process. This information is required to predict the amount (total collection efficiency, β_{TOT}), the distribution (local collection efficiency, β) and the limits (impingement limits) of the water that impacts the aerodynamic body. The total collection efficiency is defined as the ratio of the actual mass of impinging water to the maximum value that would occur if the droplets followed straight-line trajectories, figure 1.3.

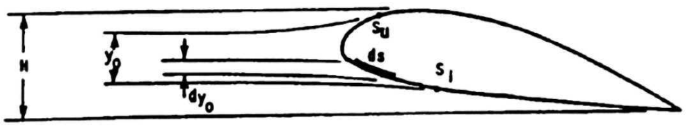

s_u = Upper – Surface Impingement Limit
s_l = Lower – Surface Impingement Limit
H = Forward Projection of the Airfoil Height

Figure 1.3: Definition of total and local collection efficiency as in LEWICE.

Total collection efficiency:
$$\beta_{TOT} = \frac{y_0}{H} \tag{1.13}$$

where y_0 is the vertical distance between the droplet release points of the upper and lower surface tangent trajectories.

The local collection efficiency, β , is also defined in figure 1.3 and can be written as:

$$\beta = \frac{dy_0}{ds} \qquad (1.14)$$

It is related to the total collection efficiency by the equation:

$$\beta_{TOT} = \frac{1}{H}\int_{s_l}^{s_u} \beta ds \qquad (1.15)$$

where s_u and s_l are the upper and lower surface impingement limits, respectively.

The droplet trajectory is the solution of a partial differential equation representing the force balance on the droplet. The motion of a particle is analyzed as a point mass particle that is acted on by the flow field. The forces involved are: inertial, drag, buoyancy and gravitational forces. All methods are based on fundamental assumptions like:

- The influence of water droplets on the flow field can be ignored
- There are no grazing collisions, no bouncing, no splashing, no coalescence, no breakup and no droplet eccentricity.

Important factors are the droplets size and the liquid water content of the cloud. The droplet size will influence the balance between inertia and drag forces. Small droplets will almost follow the flow streamlines until impact; while large droplets, less affected by the flow field, will more or less follow their own inertia before impacting.

1.3.1. Particle tracking techniques

Most impingement solutions in the literature are based on Lagrangian particle tracking techniques[14-18]. A particle is launched from the freestream and followed until it hits the body. The LEWICE and ONERA code approaches are succinctly presented below.

1.3.1.1. LEWICE

Equations

If droplets are considered rigid spheres, say for radii less than $500.0\mu m$ [27], the only forces acting on them are those of drag and gravity. Then, one has to solve the following equation:

$$m_d \vec{\gamma}_d = \frac{C_D}{2} \rho_a A_d \left\| \vec{V}_r \right\| \vec{V}_r + m_d \vec{g} \tag{1.16}$$

where $\vec{\gamma}_d$ is the droplet acceleration, m_d the mass of the droplet, A_d a characteristic area of the droplet, $\vec{g}$ the gravity vector, ρ_a the air density and $\vec{V}_r$ the droplet velocity relative to the fluid velocity. The drag coefficient C_D is a function of the droplet Reynolds number $\mathrm{Re}_d = \dfrac{\left\| \vec{V}_r \right\| d}{\nu}$.

Computational approach

Droplets trajectories are integrated via a Runge-Kutta method. For simplicity, lets take the example of a 2D calculation. The initial particle location (x_0, y_0) and velocity must be determined, either by the user or by the code. A particle should be released far upstream of the body where the flow field velocity is the same as the free stream conditions. The program will select an x-coordinate assuming flow in x direction, by searching the position where the local flow field velocity u_l and the free stream u_∞ velocity satisfy the condition:

$$\left|1-\frac{u_l}{u_\infty}\right|_{y_{0\min}}^{y_{0\max}} \leq \varepsilon \tag{1.17}$$

where ε, $y_{0_{\min}}$, $y_{0_{\max}}$ are input by the user to define a trial launching area at infinity. $y_{0_{\min}}$, $y_{0_{\max}}$ are the initial guesses for the y-coordinate of the upper and lower surface tangent trajectory release points. Equation (1.17) is tested over the range $y_{0_{\min}} \leq y_0 \leq y_{0_{\max}}$.

One way of solving the problem is LEWICE's[14] methodology: with the initial coordinate x set, the search is narrowed by determining two trajectories that pass below and above the body. The vertical distances, from which the particles are released ($y_{0_{\min}}, y_{0_{\max}}$), are specified by the user. Using these upper and lower trajectories as limit boundaries, the upper and lower impingement limits can be determined. For example, when searching for the upper impingement limit, the trajectory of a particle released from $y_{0/1} = \frac{(y_{0_{\min}} + y_{0_{\max}})}{2}$ is computed. If it passes over the body, the next trajectory is calculated from $y_{0/2} = \frac{(y_{0_{\min}} + y_{0/1})}{2}$. If it hits the body, the next trajectory is calculated from $y_{0/2} = \frac{(y_{0/1} + y_{0_{\max}})}{2}$. Successive halving of the range $y_{0_{\min}}$ to $y_{0_{\max}}$ continues until the upper impingement limit is found. Convergence of this iterative procedure is obtained when the difference between the y_0 of two trajectories, one that misses the body and one that hits the body is less than a tolerance specified by the user. Knowing the upper and lower limits, the range of vertical positions between these two limits can be divided into a specified number of increments. The trajectory of each particle leaving an increment position will be computed and will be used to compute the local collection efficiency.

Comments

In 3D, an unstructured collection efficiency calculation method was added to LEWICE3D by Bidwell[21]. The user specifies an upstream release region (a vertical quadrilateral) which encompasses the region of interest and a minimum cell size. The region is then recursively subdivided (trajectories are released at the vertices of the subdivided region) in areas where particle trajectories become close or hit the body until the minimum cell size requirement is met. The collection efficiency for each panel is then equal to the number of particles that hit the panel times the area of the minimum upstream cell size divided by the area of the panel. According to Bidwell this method is more computationally expensive than traditional methods but large, and/or complex problems are easier to setup.

1.3.1.2. ONERA

In the ONERA[15, 23] code gravity forces are neglected. The only force acting on the droplet is assumed to be the aerodynamic drag:

$$m_d \vec{\gamma}_d = \frac{\pi}{8} d^2 C_D(\mathrm{Re}_d)\rho_a \left\| \vec{V}_r \right\| \vec{V}_r$$

where d is the droplet diameter.

The droplets trajectories are computed using an explicit scheme[15]. This calculation requires the knowledge of the local velocity at any point in the space. As the Euler (or linear potential) method gives the velocity field at each node of a three-dimensional grid in the space around the body, a triple linear interpolation allows the calculation of the velocity anywhere inside a mesh element. Hence the impact position of a droplet might be determined. The definition of the local collection efficiency requires an evaluation of the area between four impact points (P1, P2, P3 and P4, figure 1.4). Such a process is not an easy task to implement in 3D, when the wall body surface is curved as it implies:

- Knowing the exact coordinates position of the impact points
- Determining the area between four points on a two-dimensional curved surface embedded in 3D.

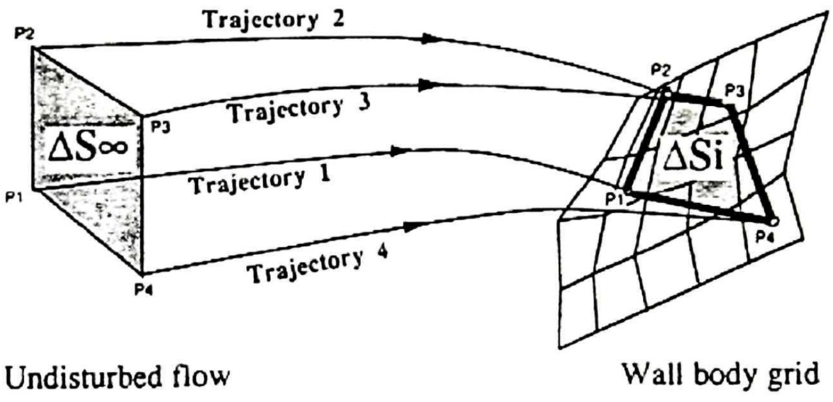

Figure 1.4[23]: Calculation of the local collection efficiency by ONERA, projection of the surface elements ΔS_∞ along the droplet trajectory lines on the body wall ΔS_i.

Values of β are defined on the body wall at the center of each surface element ΔS_i, figure 1.4. Therefore, an interpolation of β has to be done to obtain value of β in each cell of the grid used to establish the thermodynamic balance.

1.3.2. Conclusions: advantages and limitations

Particles tracking techniques have been developed, but although very efficient in 2D and on simple geometries, these codes encounter major difficulties on complex geometries such as non-axisymmetric nacelles, high-lift wings, engine intakes or systems that combine external and internal flows. In 3D, Lagrangian methods quickly become computationally expensive. Indeed, the more complex is the body geometry the more droplets trajectories have to be computed to obtain reliable collection efficiency and impingement limits. The spatial marching scheme used by Lagrangian methods suffers from a major limitation, the tedious determination of launching areas for droplets to impact. Furthermore, the definition of the local collection efficiency can quickly become fastidious.

1.4. Thermodynamic module[14-18]

The vast majority of ice accretion modules are based on the Messinger[28] model, developed in 1953. The equations that model the freezing process are determined after applying the first law of thermodynamics for mass and energy balance on a control volume and yield, panel by panel, the fraction of the water that freezes, runs back or evaporates. The control volume analyzed extends from the body surface to the liquid water film/air interface. The lower boundary of the control volume is initially on the clean geometry and moves outward with the iced geometry. In practice, a control volume is created on each segment (panel) defining the body geometry. The mass and energy equations resulting will be described.

1.4.1. Mass balance

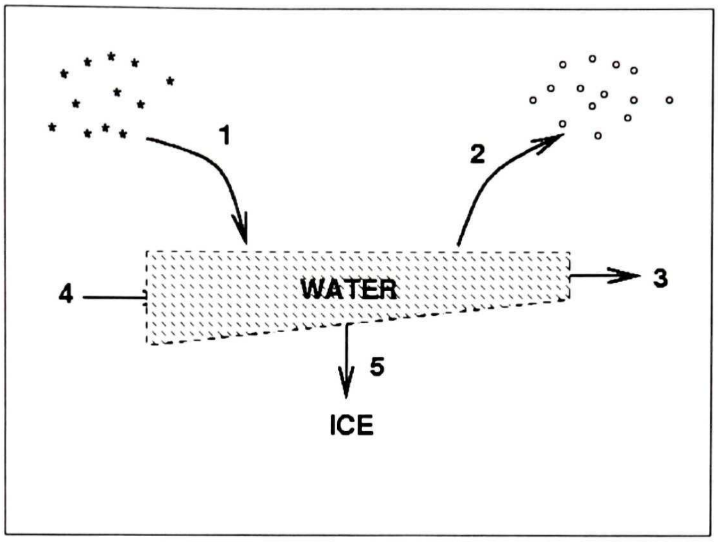

1.	Impinging water	$\dot{m}_\beta$
2.	Evaporation	$\dot{m}_{evap}$
3.	Water flow out of CV	$\dot{m}_{rout}$
4.	Water flow into CV	$\dot{m}_{rin}$
5.	Ice accumulation leaving the CV	$\dot{m}_{ice}$

Figure 1.5: Mass balance for a control volume.

The evaluation of all masses entering and leaving the control volume is shown in figure 1.5. A mass balance can be derived from these terms by:

$$\dot{m}_\beta + \dot{m}_{rin} - \dot{m}_{evap} - \dot{m}_{rout} = \dot{m}_{ice} \tag{1.18}$$

Calculation starts at the stagnation point ($s = 0.0$), where there is no water inflow, i.e. $\dot{m}_{rin} = 0.0$. The freezing fraction, f, is defined as the fraction of impinging liquid that freezes within the region of impingement. In this formulation, f is defined as the fraction of the total liquid entering the control volume that freezes within the control volume, equation (1.19). If all the water freezes, then f=1, if no water freezes, then f=0.

$$f = \frac{\dot{m}_{ice}}{\dot{m}_\beta + \dot{m}_{rin}} \tag{1.19}$$

Substituting equation (1.19) into equation (1.18), the mass balance can be expressed as:

$$\dot{m}_{rout} = (1 - f)\left(\dot{m}_{\beta} + \dot{m}_{rin}\right) - \dot{m}_{evap} \tag{1.20}$$

1.4.2. Energy balance

The same control volume approach is used for the energy balance on the icing surface. The first law of thermodynamics for the control volume can be expressed as: energy inflow rate = energy outflow rate + energy storage rate. The modes of energy transfer are illustrated in figure 1.6.

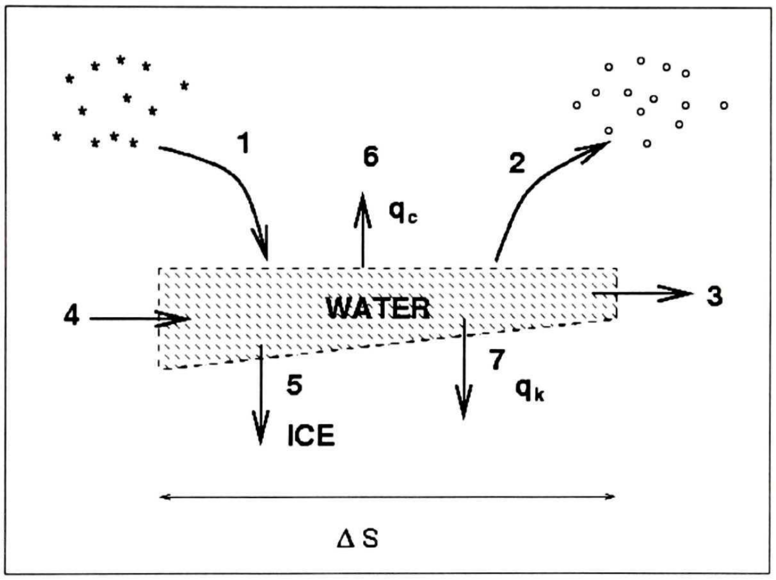

1.	Impinging water	$\dot{m}_{\beta} i_{w,T}$
2.	Evaporation	$\dot{m}_{evap} i_{v,sur}$
3.	Water flow out of CV	$\dot{m}_{rout} i_{w,sur}$
4.	Water flow into CV	$\dot{m}_{rin} i_{w,sur}$
5.	Ice accumulation leaving the CV	$\dot{m}_{ice} i_{ice,sur}$
6.	Convection	$q_c \Delta s$
7.	Conduction	$q_K \Delta s$

$$\dot{m}_{\beta} i_{w,T} + \dot{m}_{rin} i_{w,sur} = \dot{m}_{evap} i_{v,sur} + m_{rout} i_{w,sur} + \dot{m}_{ice} i_{ice,sur} + q_c \Delta s + q_K \Delta s$$

Figure 1.6: Energy balance for a control volume.

Adopting the convention that the energy entering the control volume is positive, the terms are summed in the following manner:

$$\dot{m}_{\beta} i_{w,T} + \dot{m}_{rin} i_{w,sur(i-1)} = \dot{m}_{evap} i_{v,sur} + m_{rout} i_{w,sur} + \dot{m}_{ice} i_{ice,sur} + q_c \Delta s + q_K \Delta s \qquad (1.21)$$

The evaluation of the terms of the energy equation has been made by various authors, like Sogin[29], Lowzowski[30], and Cansdale and Gent[31]. The resulting form of the energy equation is:

$$\begin{aligned}
&\dot{m}_{\beta}\left[c_{p,w}(T_s - 273.15) + \frac{u_{\infty}^2}{2}\right] + \dot{m}_{rin}\left[c_{p,w(i-1)}\left(T_{sur(i-1)} - 273.15\right)\right] + q_K \Delta s = \\
&\dot{m}_{evap}\left[c_{p,w}(T_{sur} - 273.15) + L_v\right] + \left[(1-f)\left(\dot{m}_{\beta} + \dot{m}_{rin}\right) - \dot{m}_{evap}\right] c_{p,w}\left(T_{sur} - 273.15\right) \\
&+ f\left(\dot{m}_{\beta} + \dot{m}_{rin}\right)\left[c_{p,ice}\left(T_{sur} - 273.15\right) - L_f\right] + h_c\left[T_{sur} - T_e - \frac{r_c u_e^2}{2c_{p,a}}\right]\Delta s
\end{aligned} \qquad (1.22)$$

where $c_{p,w}$, $c_{p,ice}$, $c_{p,a}$ are the specific heat capacities of water, of ice and of air, respectively; T_s, T_{sur}, T_e are the temperatures of the droplets, at the surface and at the edge of the boundary layer, respectively; h_c is the convective heat transfer coefficient; L_v, L_f are the latent heat of vaporization, and the latent heat of fusion; q_K, r_c, u_e, u_{∞} are the thermal conductivity of structure, the recovery factor, the velocity at the edge of the boundary layer and the free stream velocity.

1.4.3. Differences

The LEWICE and the ONERA codes use similar approaches and equations to solve the ice accretion phenomenon. Some differences can be observed in the evaporation model and in the way these codes handle three-dimensional calculations.

LEWICE

In LEWICE the mass transfer rate of evaporation is analogous to the convective heat transfer rate and can be written[14] as:

$$\dot{m}_{evap} = \frac{h_c}{c_{p,a}}\left(\frac{P_r}{S_c}\right)^{0.667} \frac{P_{v,p}/T_{sur} - H_{r,\infty}\left(P_e/T_e\right) P_{v,s}/P_s}{\left(1/0.622\right)P_e/T_e - P_{v,p}/T_{sur}} \tag{1.23}$$

This term accounts for compressibility effects, as Cansdale[31] term, and is similar to the term derived by Sogin[29].

For 3D calculations[21], the ice accretion model is basically LEWICE2D applied along surface streamlines cuts defined by a 3D flow calculation.

ONERA code

Inside the ONERA[23] code the evaporation term is defined using Jakob's formulation, assuming that the saturation vapor pressure at the edge of the boundary layer is the same as at freestream:

$$\dot{m}_{evap} \cong \left(\frac{1}{Le}\right)^{2/3} \frac{h_c}{c_{p,a}} \frac{\mathrm{M}_{m(water)}}{\mathrm{M}_{m(air)}} \frac{T_\infty}{\overline{T}} \frac{P_{v,p} - P_{v,\infty}}{P_\infty} \tag{1.24}$$

where $\overline{T} = \left(T_{sur} + T_\infty\right)/2$ is a mean temperature.

To simplify the thermodynamic balance in 3D a new body grid is generated by ONERA[10] along the runback paths; this grid is called the thermodynamic grid (figure 1.7) and is built on the complete geometry. In a three-dimensional icing model, runback water occurs on surfaces, it is then necessary to calculate the runback paths to know where the water will freeze. An order of magnitude study by Hedde *et al.*[23] shows that, for usual aircraft speed, the runback water closely follows the wall air streamlines. On the thermodynamic grid the thermodynamic balance is nearly the same as on a two-dimensional model. In this new grid, there is no runback across lateral grid edges. But the difference with a classical 2D ice accretion code is that one or more runback lines may disappear or appear to keep the cell size within a given range, figure 1.8. When one or more lines disappear, the flow from two or more cells is mixed into one cell conserving heat and mass. On the other hand, when one or more lines appear, the flow from one cell is split between the children cells. Each child cell receives a flow that is proportional to the length of the edge common with the parent cell.

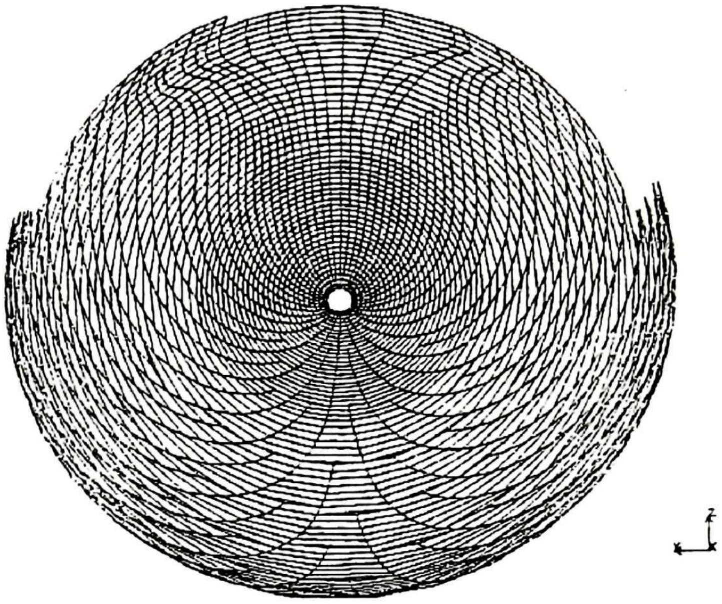

Figure 1.7[23]: ONERA thermodynamic grid build along the streamlines (runback paths).

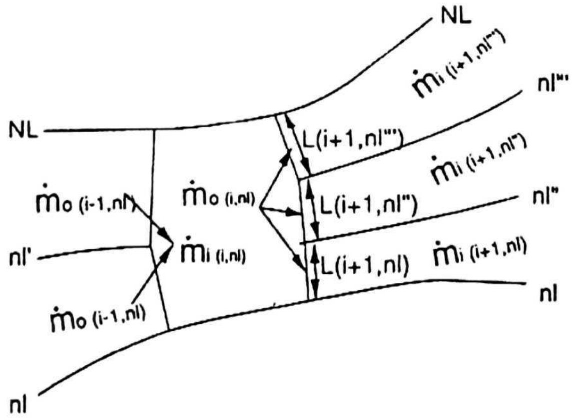

Figure 1.8[23]: To maintain a quasi-constant cell width, ONERA runback paths lines may disappear or appear, running back water is therefore mixed or split.

1.4.4. Creation of the iced grid

Given the icing rate, the ice shape is created by the deformation of a grid (figure 1.9). It can be either the "thermodynamic grid", or after interpolation of the icing rate the original geometric grid. The deformation of the original grid allows the user to re-inject it in the icing code and to perform a multi-stepping ice growth.

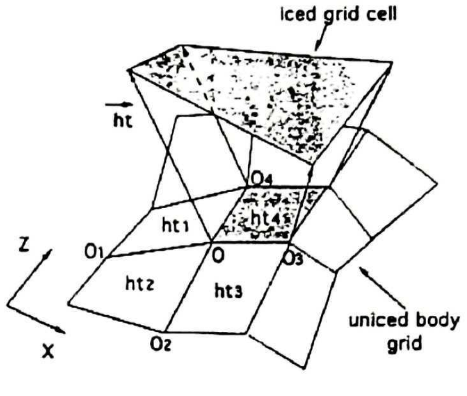

Figure 1.9[23]: Generation of an iced grid.

1.4.5. Conclusions: advantages and disadvantages

In 2D, these icing codes are very efficient, fast and do not require large computer resources. Moreover, extensive validations of these codes are publicly available and remain a precious source of information.

In the literature, even for three-dimensional calculations, it is basically the two-dimensional version of the thermodynamic code that is applied on the streamlines[21, 23] of interest. ONERA even builds a new grid, the "thermodynamic grid", following the runback paths (the streamlines) to be able to predict where the water will or will not freeze, but on this grid runback across lateral grid edges is not possible. For other codes, the complete body geometry is not always studied, in some cases only parts of it.

1.5. Conclusions

Current codes constitute valuable tools to identify important physical phenomena behind the ice accretion process. Lots of efforts have been put in the validation of the 2D version of these codes. The low amount of computer resources (CPU-time) required by the 2D codes allows the user to run multiple cases, choosing different parameters, and to validate against experiments done in icing tunnels. These analytical models also serve in the preliminary design phase of anti- and de-icing devices.

For 3D complex geometries, these codes encounter major difficulties. For example, communications and exchanges between the three modules of a solution process (flow field + boundary layer, impingement solution, and ice accretion) are impossible, or at best painful, because each task requires the creation of a special mesh and uses a different class of solvers. Interpolation and extrapolation must be used to make these modules communicate and hence numerical imprecision, human error and time waste can occur. In 3D, it is also not clear that these classical approaches need less computer resources. The particle tracking techniques are suitable for 2D simple geometries but not adapted to complex 3D geometries. Moreover none of these approaches is truly 3D from the flow field solution to the ice accretion solution. The ice accretion module remains 2D but built on streamlines or runback paths, without the possibility to predict across lateral grid edges water runback.

It is believed that only a Navier-Stokes flow solver can take into account the viscous effects on complex airflow solutions and only a 3D thermodynamic icing module can predict runback across lateral thermodynamic grid edges. Therefore it is our intention to develop a modern in-flight icing system based on the resolution of the viscous flow field (with the Navier-Stokes equations), on an Eulerian impingement calculation to simplify the determination of the local collection efficiency even on 3D complex geometries, and on a 3D thermodynamic icing module to be able to predict runback across lateral grid edges.

The same mesh will be used by the three modules to compute the airflow solution, the droplets solution and the ice accretion shape and no limitation whatsoever would exist as to geometric complexity. In addition, because of the pervasive nature of CFD in the aerospace industry, both for external and internal flows, any icing system must use same generation tools as aerodynamics analysis systems, in order for ice protection to become a concurrent engineering process with aerodynamics design.

Chapter 2

The CFD In-flight Icing Methodology

Modern computational fluid dynamics (CFD) techniques can overcome many of the difficulties encountered by traditional icing approach. The main objective of the research presented in this thesis is to develop a new modular ice accretion tool and methodology based on modern CFD algorithms. The approach suggested here views icing accretion simulation as the solution, using partial differential equations, of the 3D compressible turbulent Navier-Stokes equations, the collection efficiency by an Eulerian method, and the three-dimensional mass balance and heat transfer at the aerodynamic surface. As shown in figure 2.1, the three modules are set in an interactive loop. Each system of PDEs (airflow/impingement/accretion) is solved independently, with selected variables exchanged and updated between modules when required. The following methods are used for the numerical solution of the icing problem:

- Both the flow and droplets solvers are discretized using a weak-Galerkin finite element method on structured, unstructured or hybrid meshes.
- A Newton-generalized minimal residual (GMRES) algorithm is used to solve each nonlinear system of equations.
- In the ice accretion module, a finite volume approach is found more appropriate.
- The movement of the walls caused by ice growth is done inside the flow solver through an Arbitrary Lagrangian Eulerian (ALE) scheme, using the ice growth

rate to specify the wall nodes movement. This could be complemented by a mesh optimization method.

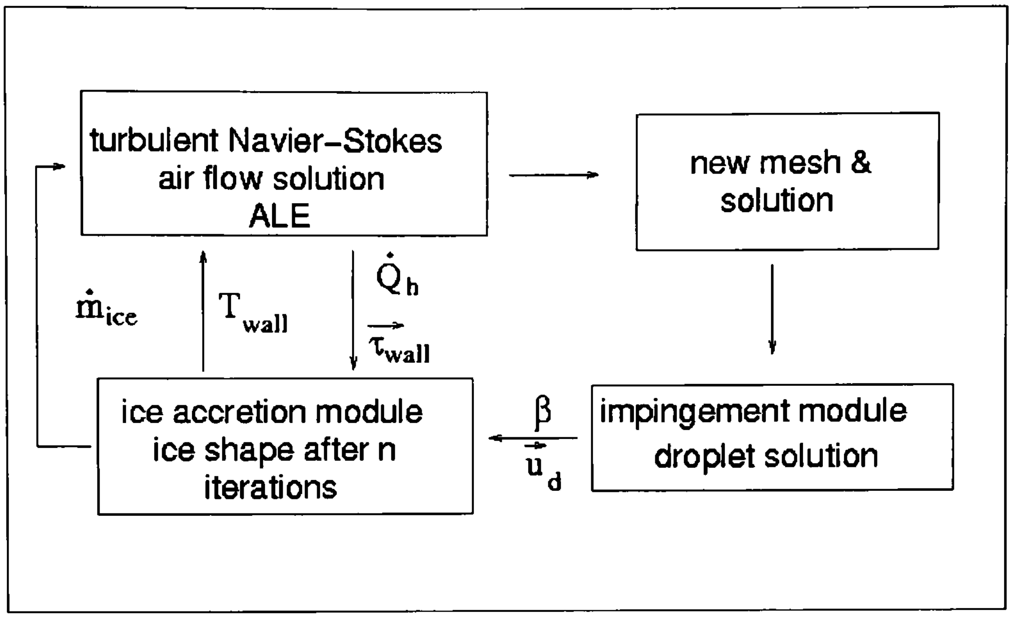

Figure 2.1:Module interactions within an in-flight icing code.

In this chapter, the three modules (airflow/impingement/accretion) used to perform the ice accretion will be briefly described, and a global icing methodology will be presented.

2.1. Airflow solver

In our approach we suggest solving the compressible Navier-Stokes equations[32], thus fully and directly accounting for the influence of the viscosity and turbulence. A 3-D Navier-Stokes flow solver, FENSAP[32], was already available. The contribution from this thesis to this flow solver is the implementation of the one-equation Spalart-Allmaras turbulence model, with a special representation of the surface to account for roughness. The equation, its discretization, and the validation of the model with and without roughness, are described in chapter 3.

Why 3D?

It is evident that in the aerospace industry most aerodynamic analysis activities have become based on CAD systems, shared between various departments. This is done to maintain geometric fidelity and permit concurrent engineering all the way from analysis to manufacturing. Thus, icing analysis methods not based on CAD systems perpetuate the compartmentalization of the aerodynamic and icing activities and are not able to capitalize on the wealth of dry air solutions obtained by aerodynamicists.

Besides physical fidelity being increased in 3D, 3D aerodynamics is not a simple extrapolation of 2D aerodynamics: for example a wing of finite span is not aerodynamically equivalent to a stacking of airfoils, figure 2.2.

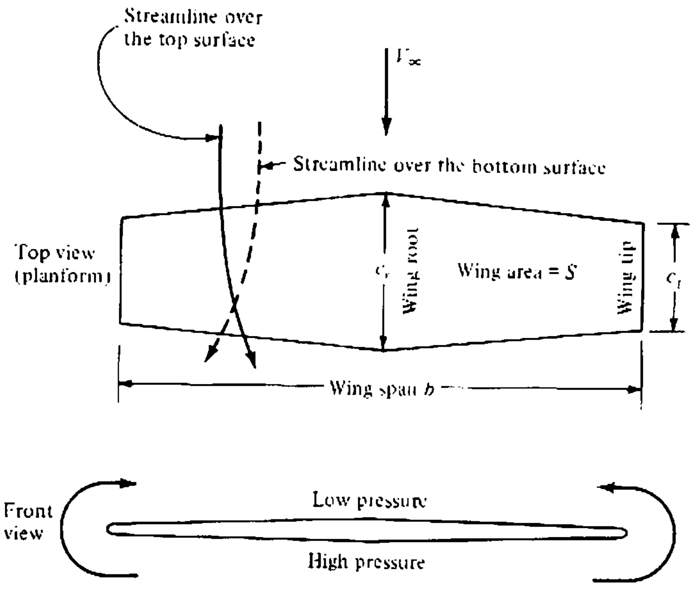

Figure 2.2: Sketch of the curvature of the streamlines over the top and bottom of a finite wing, source Anderson (Ref. 19).

The physical mechanism for generating lift on the wing is the existence of a high pressure on the bottom surface and a low pressure on the top surface. The net difference of the pressure distribution creates the lift. However, as a by-product of this pressure imbalance, the flow near the wing tips tends to curl around the tips going from high pressure to low pressure. As a result, on the top surface of the wing, there is generally a spanwise component of flow from the tip toward the wing root. Similarly, on the bottom surface of the wing, there is generally a spanwise component of flow from the root toward the tip. When the flow "leaks" around the wing tips it creates a circulatory motion which trails downstream the wing, a trailing vortex is created at each wing tip (figure 2.3).

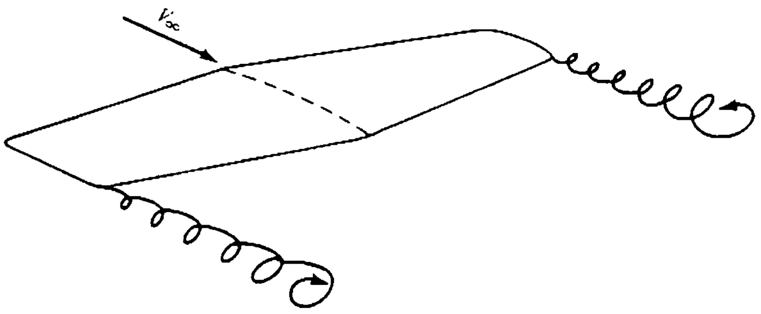

Figure 2.3: wing-tip vortices, source Anderson (Ref. 19).

These wing-tip vortices downstream of the wing induce a small downward component of air velocity in the neighborhood of the wing. The downward component is called downwash. The downwash, combined with the free stream velocity, creates a relative wind (figure 2.4), which will reduce, by a different amount along the span, the angle of attack seen by each section. Relations exist to derive the local angle of attack seen by the airfoil. Therefore, using this correction, it is possible to use 2D calculations, for most parts of a finite wing, except at tips and body-wing junctions. Nevertheless, there is no guarantee that the same correction applies to droplets of various sizes. In addition, even if the local angle is corrected, the spanwise velocity is not accounted for.

Moreover a body-wing junction, a body-tail junction, a non-axisymmetric nacelle, a helicopter air intake are truly 3D geometries. Thus, to simulate ice accretion on complete aircraft or on geometries that present strong 3D characteristics, a 3D code is an absolute necessity and is presently lacking.

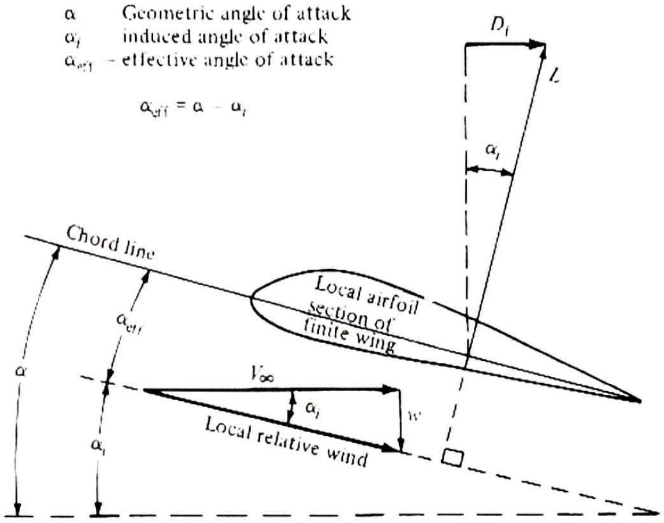

Figure 2.4: Effect of downwash over an airfoil of a finite wing, source Anderson (Ref. 19).

Moreover, some ice shapes characteristics, like the scalloping effects[33] that are not currently predictable by any icing code, seem to be partially due to 3D flow patterns. At least, this physical phenomenon is observed on finite or infinite swept wings but not on airfoils. In fact, it is the cross-flow (along the leading edge) that seems to cause scallops. As a consequence, when scalloping effects are encountered, the numerical ice shape predicted on airfoils will not be representative of the experimental ice shape[34] measured at the same positions on the wing. This can have an important impact because until now, 2D codes are used to predict ice shapes to be attached to an aircraft during certification[34]. Of course, it is easy, when desired, to degrade a 3D code to 2D, a compressible code to nearly incompressible, a Navier-Stokes code to Euler, a turbulent code to laminar, while the reverse is not possible.

2.2. Impingement module

To compute droplets impingement, an Eulerian model[35] is proposed as an alternative to the traditional Lagrangian particle tracking approach. A Bourgault *et al.* Eulerian model, for airflows containing water droplets is thought to be more suitable for use with a field solver such as finite element or finite volume. Droplets velocity and volume fraction of water have to be computed only at the nodes where the airflow variables are known, so no particle has to be tracked through the mesh as in a Lagrangian method. Droplets impingement on complex 3D geometries[36], or on multi-element airfoils, is done in an automatic way, without a painful determination of launching areas. In fact, as the entire impingement field is predicted, shadow zones (zones of very low impingement) are automatically determined for the placement of probes, etc.

No modification of the Navier-Stokes equations is needed when droplets are present, because the loading, i.e. the ratio of the bulk density of the droplets over the bulk density of the air, is of the order of 10^{-3} in icing. It is usually agreed that a loading smaller than 0.1 is well modeled by a one-way coupling[37].

The variables $\alpha(x,t)$ and $\vec{u}_d(x,t)$ are mean values of the ratio of the volume occupied by water over the total volume of the fluid element and of the droplets velocity over the element, given a small fluid element around any specific location x in space at time t. The following assumptions are made:

- a continuous medium;
- droplets are spherical without any deformation or breaking;
- no droplets collision, coalescence or splashing;
- no heat and mass exchange between the droplets and the surrounding air;

- turbulence effects on droplets are neglected;
- the only forces acting on droplets are drag, gravity and buoyancy.

The continuity and momentum droplets equations are written using non-dimensional variables:

$$\frac{\partial \alpha}{\partial t} + \nabla \cdot \left(\alpha \vec{u}_d \right) = 0 \tag{2.1}$$

$$\frac{\partial \vec{u}_d}{\partial t} + \vec{u}_d \cdot \nabla \vec{u}_d = \frac{C_D \operatorname{Re}_d}{24K} \left(\vec{u}_a - \vec{u}_d \right) + \left(1 - \frac{\rho_a}{\rho} \right) \frac{1}{Fr^2} \vec{g} + \frac{\rho_a}{\rho} \left(\frac{\partial \vec{u}_a}{\partial t} + \vec{u}_a \cdot \nabla \vec{u}_a \right) \tag{2.2}$$

where:

$\vec{u}_a$ = non-dimensional velocity of air,

$\vec{u}_d$ = non-dimensional velocity of droplets,

ρ = density of water, ρ_a = density of air,

d = droplets diameter,

$\operatorname{Re}_d = \dfrac{\rho d U_\infty \left| \vec{u}_a - \vec{u}_d \right|}{\mu}$ is the droplets Reynolds number, $Fr = \dfrac{U_\infty}{\sqrt{l g_0}}$ is the Froude number, and $K = \dfrac{\rho d^2 U_\infty}{18 l \mu}$ is an inertia parameter,

where l is the characteristic length (typically the airfoil chord length).

The drag coefficient for spherical droplets depends on the droplet Reynolds number according to equations (2.3) or (2.4):

$$C_D = \frac{24}{\operatorname{Re}_d} \left(1 + 0.15 \operatorname{Re}_d^{0.687} \right), \ \operatorname{Re}_d \le 1000 \tag{2.3}$$

$$C_D = 0.4 \text{ for } \operatorname{Re}_d > 1000 \tag{2.4}$$

The last terms on the right-hand-side of the momentum equations account for gravity and buoyancy effects. The system models the evolution of droplets having the same nominal diameter. A characteristics analysis[35] shows that boundary conditions are needed on the inflow boundaries for all variables and that no boundary conditions are needed on surface walls or on the outflow boundaries. An initial solution is to take $\vec{u}_d = (\cos(AoA), \sin(AoA))$ and $\alpha = 1$ everywhere except near the airfoil surface, where both variables are forced to zero. Here AoA stands for Angle of Attack.

The discretization of the equations is made through a weak-Galerkin finite element method. Stabilization terms, streamline upwinding (SUPG)[38] terms, are added to remove possible oscillations in the droplets solution.

An important parameter that controls the accretion of ice on an airfoil is the local collection efficiency β, i.e. the normalized flux of water on the aerodynamic surface. Within the Eulerian approach, the collection efficiency is computed on every face belonging to the aerodynamic surface using:

$$\beta = -\alpha \vec{u}_d . \vec{n} . \tag{2.5}$$

The water flux $\dot{m}_w$ at the airfoil surface would then be:

$$\dot{m}_w = LWC\, U_\infty\, \beta . \tag{2.6}$$

Some special care is required for the computation of the normal $\vec{n}$ to the aerodynamic surface at a node, but apart from that, the recovery of the collection efficiency can be coded very simply even for multi-element airfoils and complex 3D geometries.

Equations (2.1) to (2.6) are derived for a uniform droplets diameter d. Clouds, however, usually contain a distribution of droplet diameters. The computation of flows containing droplets of different sizes can be done by splitting the diameters distribution into a finite number of classes and by solving each class independently. If the percentage of droplets in the ith class is given by p_i the overall collection efficiency would be:

$$\beta = \sum_i p_i \beta_i ,$$

with β_i the ith class collection efficiency. Hence, the droplets code does not have to be modified to handle poly-dispersed droplets, as long as the change of air momentum due to droplets is neglected.

A typical and most accepted icing cloud distribution is the Langmuir-D distribution. An example of this distribution for a MVD of $16\mu m$ is given in table 2.1. Using a droplet distribution, the impingement limits are more accurately[39] predicted, and usually the maximum value of the collection efficiency is larger for the monodispersed droplets[39].

Percentage LWC (%)	Ratio of diameters	Droplet diameter (μm)
0.05	0.31	5.0
0.10	0.52	8.3
0.20	0.71	11.4
0.30	1.00	16.0
0.20	1.37	21.9
0.10	1.74	27.8
0.05	2.22	35.5

Table 2.1:Langmuir D distribution of droplet diameters for a MVD of $16\mu m$.

2.3. Ice accretion module

The third component, a modern ice accretion module, based on a totally rethought approach for ice formation, completes the necessary triad of: flow solution – impingement solution – ice accretion solution. A new thermodynamic approach for predicting 3D ice shapes is formulated. A fully three-dimensional approach to icing is taken. In chapter 4, the new physical model, based on partial differential equations for mass and energy conservation is derived and an appropriate numerical scheme is proposed to solve the system of equations. The 2D validation of the complete system is presented in chapter 5, and 3D results in chapter 6.

2.4. Methodology

System-based ice accretion computations are obtained through an interactive process, figure 2.5. For geometric fidelity, a 3D CAD-based mesh is generated around the surface to study. A 3D turbulent airflow solution is first computed. Then, using the same mesh and the velocity field from the airflow solution, the droplet impingement is computed. Finally, with the airflow solution (friction forces & heat fluxes) and with the droplet solution (collection efficiency & droplet velocity), the surface node displacement due to ice accretion is calculated on the same mesh.

Two approaches, figure 2.6, are used to calculate ice accretion with time: the one-shot ice growth and the multi-stepping ice growth. With a one-shot ice accretion, the ice accretion shape is computed using only the original airflow and droplet solutions. With a multi-stepping approach the airflow solution and the droplet solution are updated during the ice accretion process after a certain time of ice accretion. The multi-stepping approach should be more accurate. Indeed, the updated airflow solution will take into account the geometric deformations due to ice growth and the droplet impingement will also be strongly affected by the body deformations. However, a truly time-accurate unsteady technique is impractical so far, as it would require the calculation of the airflow and droplet solution after each time step of the ice accretion module and thus demand large computer resources. Instead, a quasi-steady approach is proposed so that the computed ice shapes can be compared to the experimental and numerical solutions, which usually involve a few minutes of ice accretion.

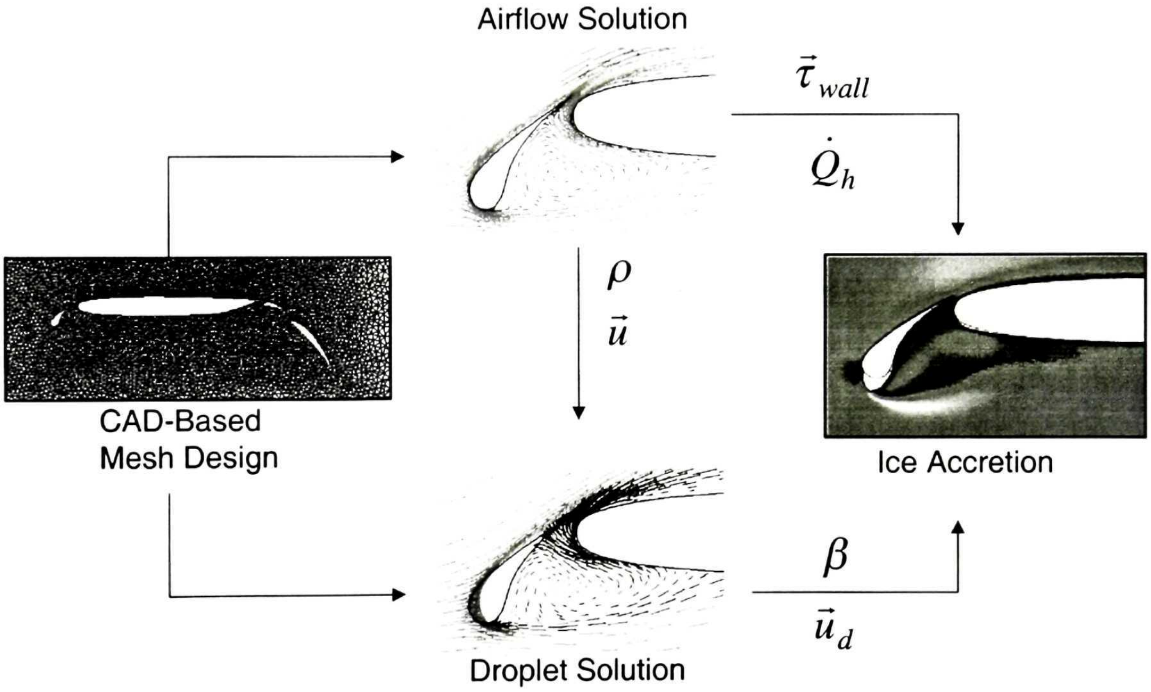

Figure 2.5: CFD methodology.

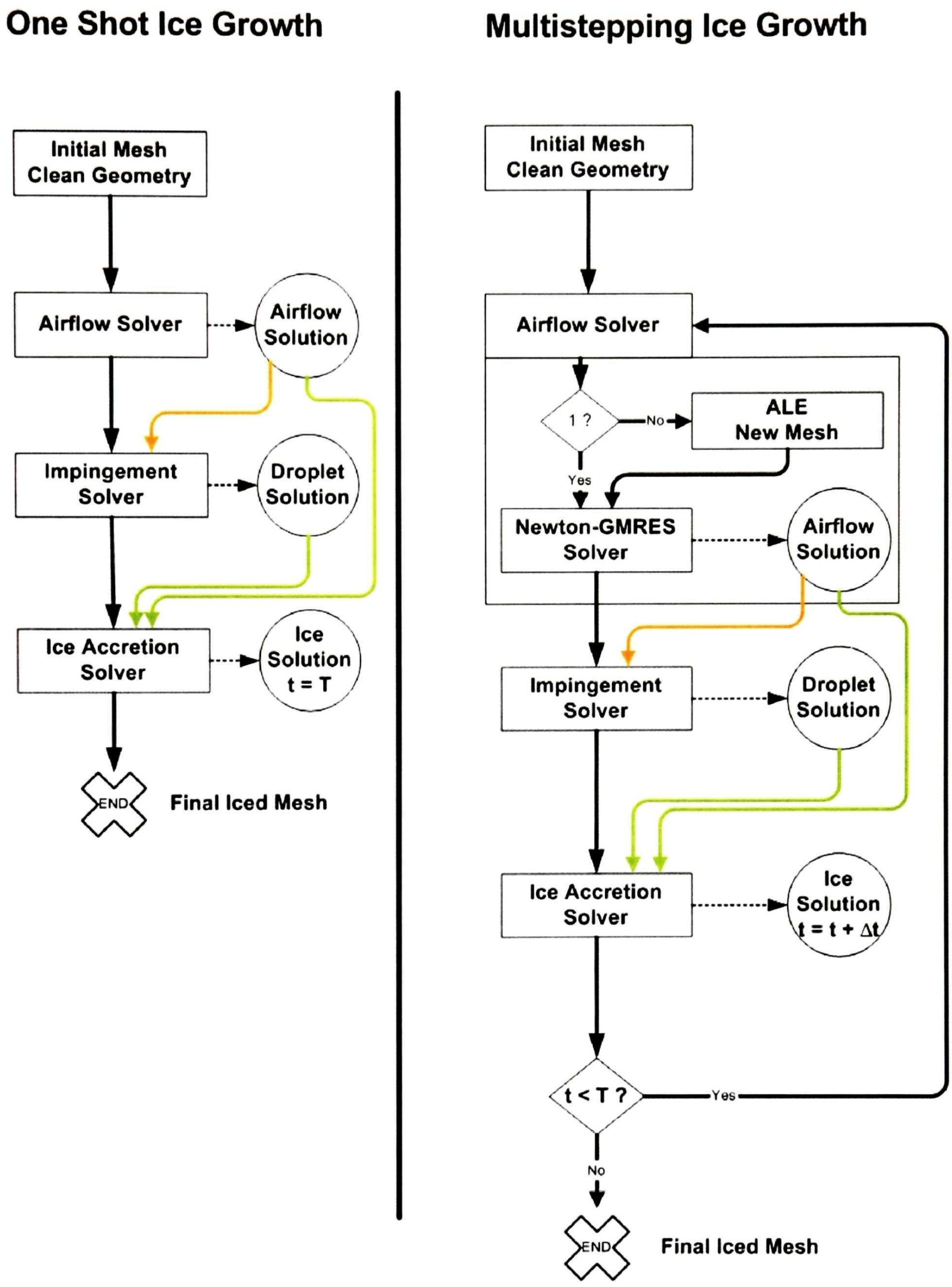

Figure 2.6: Two methodologies for ice accretion: the one-shot approach and the multi-stepping approach.

Chapter 3

Spalart-Allmaras Turbulence Model

Currently, the only industrially practical way to simulate turbulent flows is to solve the Reynolds-Averaged Navier-Stokes (RANS) equations together with a turbulence model. Modeling turbulence has become an intrinsic task in CFD[40, 41]. In aerodynamics, simple algebraic turbulence models have been widely used with fair success. However, the algebraic models are not suitable to handle complex flow situations like separation, wakes, etc. In icing, separated flows occur most of the time because of the surface roughness and the complex ice shapes resulting from the impact of droplets. An icing requirement is to accurately predict convective heat fluxes on smooth and rough surfaces in a situation of complex turbulent flows.

The Spalart-Allmaras model proposes an alternative to simple algebraic models or complex transport-equation models by creating a "local" type transport-equation, which is more sophisticated than algebraic models, but more robust and easier to use than the traditional two-equation or higher degree models.

This chapter describes the implementation and validation of the Spalart-Allmaras turbulence model in FENSAP. FENSAP is a 3D code based on the compressible turbulent Navier-Stokes equations. The spatial discretization of the entire code (FENSAP + Spalart-Allmaras model) is carried out by FEM and the governing equations are linearized by a Newton method. To advance the solution in time, an implicit scheme is used, along with a GMRES procedure to iteratively solve the resulting matrix system.

We first recall the non-dimensional form of the Navier-Stokes and energy equations used in FENSAP[42] and then describe the one-equation turbulence model. The basic functionality of the new model is tested by solving the flat-plate turbulent boundary layer flow. The validation of roughness inside the Spalart-Allmaras model is then done on rough flat-plates and rough pipe flows.

FENSAP Governing Equations (Navier-Stokes and energy)

The Reynolds-averaged Navier-Stokes equations used in FENSAP can be stated in the following manner:

Continuity Equation

$$\frac{\partial \rho}{\partial t} + (\rho u_i)_{,i} = 0$$

Momentum Equations, $i = 1,\ldots,3$

$$\frac{\partial \rho u_i}{\partial t} + \left(\rho u_i u_j\right)_{,j} = -p_{,i} + \frac{1}{\mathrm{Re}_\infty}\left[\mu\left(u_{i,j} + u_{j,i} - \frac{2}{3}\delta_{ij} u_{k,k}\right)\right]_{,j}$$

Energy Equation

$$H = H_\infty$$

or

$$\frac{\rho c_p \partial T}{\partial t} + \left(\rho c_p u_j T\right)_{,j} = (\gamma - 1) M_\infty^2 \frac{Dp}{Dt} + \frac{1}{\mathrm{Re}_\infty \mathrm{Pr}_\infty}\left(\kappa T_{,j}\right)_{,j} + \frac{(\gamma-1) M_\infty^2}{\mathrm{Re}_\infty}\left(u_i \tau_{ij}\right)_{,j}$$

where $\tau_{ij} = \mu\left(u_{i,j} + u_{j,i}\right) + \lambda \delta_{ij} u_{k,k} \quad (2\mu + 3\lambda = 0)$.

The Reynolds number is defined as:

$$\mathrm{Re}_\infty = \frac{\rho_\infty l_\infty U_\infty}{\mu_\infty}.$$

The Prandtl number is defined as:

$$\mathrm{Pr}_\infty = \frac{\mu_\infty c_{p\infty}}{k_\infty}.$$

and the equation of state for ideal gas is used to close the system

$$p = \frac{\rho T}{\gamma M_\infty^2}.$$

3.1. The one-equation turbulence model

3.1.1. The basic Spalart-Allmaras (S-A) model

The Spalart-Allmaras[43, 44] turbulent kinematic viscosity ν_T is obtained from the modified viscosity, $\tilde{\nu}$, which is solved from the partial differential equation (3.1). This equation has a form similar to the equations for basic flow variables: density, momentum and temperature. The major difference is that the turbulence equation also contains strong source terms. The equation in non-dimensional form and without transition is:

$$\frac{\partial \tilde{\nu}}{\partial t} + u_j \frac{\partial \tilde{\nu}}{\partial x_j} = c_{b1} \tilde{S} \tilde{\nu} + \frac{1}{\sigma \mathrm{Re}_\infty} \left[\frac{\partial}{\partial x_k} \left((\nu + \tilde{\nu}) \frac{\partial \tilde{\nu}}{\partial x_k} \right) + c_{b2} \frac{\partial \tilde{\nu}}{\partial x_k} \frac{\partial \tilde{\nu}}{\partial x_k} \right] - c_{w1} f_w \frac{1}{\mathrm{Re}_\infty} \left(\frac{\tilde{\nu}}{d} \right)^2 \quad (3.1)$$

The first term on the right-hand-side represents the turbulence production, the second term represents diffusion and the last term is the destruction. The modified magnitude of vorticity is:

$$\tilde{S} = S + \frac{1}{\mathrm{Re}_\infty} \frac{\tilde{\nu}}{\kappa^2 d^2} f_{v2}$$

where S is the magnitude of the vorticity

$$S = \sqrt{2\Omega_{ij}\Omega_{ij}} \qquad \Omega_{ij} = \frac{1}{2}\left(\frac{\partial u_i}{\partial x_j} - \frac{\partial u_j}{\partial x_i}\right)$$

and d is the distance to the nearest wall. The functions f_{v1} and f_{v2} are defined as

$$f_{v1} = \frac{\chi^3}{\chi^3 + c_{v1}^3} \qquad f_{v2} = 1 - \frac{\chi}{1 + \chi f_{v1}}$$

where $\chi = \frac{\tilde{\nu}}{\nu}$ with ν the laminar viscosity. The destruction term is formed with:

$$f_w = g\left(\frac{1 + c_{w3}^6}{g^6 + c_{w3}^6}\right)^{\frac{1}{6}}$$

where

$$g = r + c_{w2}\left(r^6 - r\right) \qquad r = \frac{\tilde{\nu}}{\kappa^2 d^2 \operatorname{Re}_\infty S + \tilde{\nu} f_{v2}}$$

The closure coefficients of the model are:

$$c_{b1} = 0.1335 \quad c_{b2} = 0.622 \quad c_{v1} = 7.1 \quad \sigma = \frac{2}{3}$$

$$c_{w1} = \frac{c_{b1}}{\kappa^2} + \frac{(1 + c_{b2})}{\sigma} \quad c_{w2} = 0.3 \quad c_{w3} = 2 \quad \kappa = 0.41$$

The kinematic turbulent viscosity is obtained from:

$$\nu_T = \tilde{\nu} f_{v1}.$$

3.1.2. Laminar region and tripping

The basic model is applicable to turbulent flow without laminar boundary layer and transition region. In aerodynamic problems, there are typically both laminar and turbulent regions. The position of the transition point(s) cannot be predicted reliably using current turbulence model, and must be known a priori or an educated guess (with numerical methods) must be made.

The final model, equation (3.2), provides control over the laminar regions of the shear layers, a control with two functions: keeping the flow laminar where desired and tripping transition where desired. The subscript t will stand for "trip". This word means that the transition point is imposed by an actual trip, or occurs naturally but the position is obtained via a separate method.

There is a problem in modeling the laminar boundary layers, since $\tilde{\nu} = 0$ is an unstable solution of the turbulence equation in thin shear layers. In a boundary-layer code the zero solution is easily maintained, but in a Navier-Stokes code exactly-zero values are rarely preserved. The model is then sensitive to numerical errors upstream of the trip. The flow turns turbulent at a rate that depends on numerical details and has little to do with the boundary layer's true propensity to transition. The solution to that problem is to modify the production term so that $\tilde{\nu} = 0$ is a stable solution in shear layers upstream of the tripping points. This is done by multiplying the production term by $\left(1 - f_{t2}\right)$ where

$$f_{t2} = c_{t3} e^{\left(-c_{t4} \chi^2\right)}$$

The proposed values for c_{t3} and c_{t4} are $c_{t3} = 1.1$, $c_{t4} = 2$. A modification, involving f_{t2}, is also made in the destruction term to maintain the balance. These modifications ensure that a laminar solution is obtained upstream of the tripping points. The transition is initiated near the tripping points by adding a source term that will be non-zero only in small areas near the tripping points. This source term is $f_{t1} \Delta U^2$ and the model becomes:

$$\begin{aligned}\frac{\partial\tilde{\nu}}{\partial t}+u_j\frac{\partial\tilde{\nu}}{\partial x_j} &= \frac{1}{\sigma\mathrm{Re}_\infty}\frac{\partial}{\partial x_k}\left[(\nu+\tilde{\nu})\frac{\partial\tilde{\nu}}{\partial x_k}\right]+c_{b1}(1-f_{t2})\tilde{S}\tilde{\nu} \\ &- \left[c_{w1}f_w-\frac{c_{b1}}{\kappa^2}f_{t2}\right]\frac{1}{\mathrm{Re}_\infty}\left(\frac{\tilde{\nu}}{d}\right)^2+\frac{c_{b2}}{\sigma\mathrm{Re}_\infty}\frac{\partial\tilde{\nu}}{\partial x_k}\frac{\partial\tilde{\nu}}{\partial x_k}+\mathrm{Re}_\infty\left(f_{t1}\Delta U^2\right)\end{aligned} \tag{3.2}$$

with

$$f_{t1}=c_{t1}g_t e^{\left(-c_{t2}\frac{w_t^2}{\Delta U^2}\left[d^2+g_t^2d_t^2\right]\right)} \qquad g_t=\min\left(0.1,\frac{\Delta U}{S_t\Delta x_t}\right)$$

Here, S_t, is the magnitude of vorticity at the tripping point, ΔU is the norm of the difference between the velocity at the tripping point and at the far field point being considered, d_t is the distance from the field point to the nearest tripping point. Suitable values for the constants are $c_{t1}=1$ and $c_{t2}=2$.

3.1.3. Weak-Galerkin finite element formulation

The weak-Galerkin finite element formulation is obtained by integrating equation (3.2), in non-dimensional form, with respect to the weight function W, and integrating the spatial terms using the divergence theorem (3.3). This effectively transfers the order of differentiation from the spatial terms (convective) to the weight function allowing for the use of lower-order elements (3.4).

Let ϑ_h be the trial solution space,

$$\vartheta_h=\left\{\ \tilde{\nu}\,/\,\tilde{\nu}(.,t)\in H^1(\Omega)^m, t\in[0,T], \tilde{\nu}\,/_{\Omega^e}\in P_k(\Omega^e)^m, \tilde{\nu}(\cdot,t)=f\ on\ \Gamma_f\right\}$$

and ω_h the weighting function space:

$$\omega_h=\left\{\ W\,/\,W(.,t)\in H^1(\Omega)^m, t\in[0,T], W\,/_{\Omega^e}\in P_k(\Omega^e)^m, W(\cdot,t)=0\ on\ \Gamma_f\right\}$$

Note that for our equation m=1 and k=1. The weak formulation is then given by:

Find $\tilde{\nu} \in \vartheta_h$ such that:

$$\int_{\Omega} W \left\{ \frac{\partial \tilde{\nu}}{\partial t} + u_j \frac{\partial \tilde{\nu}}{\partial x_j} - \frac{1}{\sigma \mathrm{Re}_\infty} \frac{\partial}{\partial x_k} \left[(\nu + \tilde{\nu}) \frac{\partial \tilde{\nu}}{\partial x_k} \right] - c_{b1} (1 - f_{t2}) \tilde{S} \tilde{\nu} \right. + \left. \left[c_{w1} f_w - \frac{c_{b1}}{\kappa^2} f_{t2} \right] \frac{1}{\mathrm{Re}_\infty} \left(\frac{\tilde{\nu}}{d} \right)^2 - \frac{c_{b2}}{\sigma \mathrm{Re}_\infty} \frac{\partial \tilde{\nu}}{\partial x_k} \frac{\partial \tilde{\nu}}{\partial x_k} - \mathrm{Re}_\infty \left(f_{t1} \Delta U^2 \right) \right\} d\Omega = 0 \tag{3.3}$$

$\forall W \in \omega_h$

$$\int_{\Omega} W \left\{ \frac{d\tilde{\nu}}{dt} - \frac{dx_k}{dt} \frac{\partial \tilde{\nu}}{\partial x_k} + u_j \frac{\partial \tilde{\nu}}{\partial x_j} - c_{b1} (1 - f_{t2}) \left[S + \frac{1}{\mathrm{Re}_\infty \kappa^2 d^2} f_{v2} \tilde{\nu} \right] \tilde{\nu} + \left[c_{w1} f_w - \frac{c_{b1}}{\kappa^2} f_{t2} \right] \frac{1}{\mathrm{Re}_\infty} \left(\frac{\tilde{\nu}}{d} \right)^2 - \frac{c_{b2}}{\sigma \mathrm{Re}_\infty} \frac{\partial \tilde{\nu}}{\partial x_k} \frac{\partial \tilde{\nu}}{\partial x_k} - \mathrm{Re}_\infty \left(f_{t1} \Delta U^2 \right) \right\} d\Omega + \int_{\Omega} W_{,j} \left\{ \frac{1}{\sigma \mathrm{Re}_\infty} (\nu + \tilde{\nu}) \frac{\partial \tilde{\nu}}{\partial x_k} \right\} d\Omega - \int_{\Gamma} W \left\{ \frac{1}{\sigma \mathrm{Re}_\infty} (\nu + \tilde{\nu}) \frac{\partial \tilde{\nu}}{\partial x_j} n_j \right\} d\Gamma = 0 \tag{3.4}$$

3.1.4. Discretization

The element stiffness matrix, after the Newton linearization (setting $\tilde{\nu} = \tilde{\nu} + \Delta \tilde{\nu}$), takes the form:

$$[C_{\tilde{\nu}}][\Delta \tilde{\nu}] = -[r_{\tilde{\nu}}]$$

where the residual is:

$$r_{\tilde{\nu}} = \int_{\Omega} W \left\{ \frac{d\tilde{\nu}}{dt} - \frac{dx_k}{dt} \frac{\partial \tilde{\nu}}{\partial x_k} + u_j \frac{\partial \tilde{\nu}}{\partial x_j} - c_{b1} (1 - f_{t2}) \left[S + \frac{1}{\mathrm{Re}_\infty \kappa^2 d^2} f_{v2} \tilde{\nu} \right] \tilde{\nu} + \left[c_{w1} f_w - \frac{c_{b1}}{\kappa^2} f_{t2} \right] \frac{1}{\mathrm{Re}_\infty} \left(\frac{\tilde{\nu}}{d} \right)^2 - \frac{c_{b2}}{\sigma \mathrm{Re}_\infty} \frac{\partial \tilde{\nu}}{\partial x_k} \frac{\partial \tilde{\nu}}{\partial x_k} - \mathrm{Re}_\infty \left(f_{t1} \Delta U^2 \right) \right\} d\Omega + \int_{\Omega} W_{,j} \left\{ \frac{1}{\sigma \mathrm{Re}_\infty} (\nu + \tilde{\nu}) \frac{\partial \tilde{\nu}}{\partial x_k} \right\} d\Omega - \int_{\Gamma} W \left\{ \frac{1}{\sigma \mathrm{Re}_\infty} (\nu + \tilde{\nu}) \frac{\partial \tilde{\nu}}{\partial x_j} n_j \right\} d\Gamma$$

The coefficient of the stiffness matrix is:

$$\begin{aligned}
C_{\tilde{\nu}} \quad = \quad & \int_{\Omega} WN\left\{\frac{k}{\Delta t} - c_{b1}\left(1-f_{t2}\right)S - 2c_{b1}\left(1-f_{t2}\right)\frac{f_{v2}}{\mathrm{Re}_{\infty}\,\kappa^{2}d^{2}}\tilde{\nu} + \frac{2}{\mathrm{Re}_{\infty}}\left[c_{w1}f_{w} - \frac{c_{b1}}{\kappa^{2}}f_{t2}\right]\frac{\tilde{\nu}}{d^{2}}\right\}d\Omega \\
+ \quad & \int_{\Omega} WN_{,j}\left\{-\frac{dx_{k}}{dt} + u_{j} - 2\frac{c_{b2}}{\sigma\,\mathrm{Re}_{\infty}}\frac{\partial\tilde{\nu}}{\partial x_{j}}\right\}d\Omega + \int_{\Omega} W_{,j}N\left\{\frac{1}{\sigma\,\mathrm{Re}_{\infty}}\frac{\partial\tilde{\nu}}{\partial x_{j}}\right\}d\Omega + \int_{\Omega} W_{,j}N_{,j}\left\{\frac{\nu+\tilde{\nu}}{\sigma\,\mathrm{Re}_{\infty}}\right\}d\Omega \\
- \quad & \int_{\Gamma} WN\left\{\frac{1}{\sigma\,\mathrm{Re}_{\infty}}\frac{\partial\tilde{\nu}}{\partial x_{j}}n_{j}\right\}d\Gamma - \int_{\Gamma} WN_{,j}\left\{\frac{\left(\nu+\tilde{\nu}\right)}{\sigma\,\mathrm{Re}_{\infty}}n_{j}\right\}d\Gamma
\end{aligned}$$

In a weak-Galerkin formulation, the shape functions N and the weight functions W are identical.

The linearized terms for $\frac{dx_k}{dt}$ arise from the ALE formulation (to take into account the mesh movement due to ice growth). We add a corrective term to the time derivative in the equation to account for the movement of the grid in time. Let $f\left(x(t), y(t), z(t); t\right)$ be any function defined in space at all times. The time derivative of f is:

$$\begin{aligned}
\frac{df}{dt} &= \frac{\partial f}{\partial t} + \frac{\partial f}{\partial x}\frac{dx}{dt} + \frac{\partial f}{\partial y}\frac{dy}{dt} + \frac{\partial f}{\partial z}\frac{dz}{dt} \\
&= \frac{\partial f}{\partial t} + \nabla f \cdot \vec{x}_{t}
\end{aligned}$$

In the governing equations, the partial time derivative operator becomes:

$$\frac{\partial}{\partial t} \quad = \quad \frac{d}{dt} - \vec{x}_{t}.\nabla$$

where it is understood that $\frac{d}{dt}$ designates the time derivative taken along the trajectory of a node.

These terms are omitted in the construction of the stiffness matrix (they are only included in the residual). Numerical experiments indicate that neglecting these terms has minimal effect on the overall convergence rate of the continuity and momentum equations, so the same behavior is expected for the turbulence equation. Only $\frac{k}{\Delta t}$, corresponding to the time discretization of $\frac{d\Delta\tilde{V}}{dt}$, remains in the matrix.

3.1.5. Artificial viscosity

Numerical methods used to solve PDEs (convection type and fluid flow problems) suffer from inherent numerical oscillations when centered type discretization is used for the advection terms. The big challenge is to enhance the stability of the scheme without smearing the discontinuities (like shocks) and boundary layers. We propose here a new artificial viscosity method[45] (ISOD) based on diffusion along iso-values surfaces (or curves in 2D). The formulation of the method is done in FEM and applied to all equations: continuity, momentum, energy and turbulence. The main idea is to add a Laplacian operator in the perpendicular plane to the gradient direction of the solution. This approach simultaneously stabilizes the scheme and enhances its capability to crisply capture both shocks and boundary layers. This is due to the fact that the perpendicular plane to the gradient (the diffusion plane) is tangent to the iso-values curves or surfaces. Therefore, the smoothing effect along the iso-values ensures the stability of the scheme, avoiding the negative or cross-diffusion effects of classical artificial viscosity methods.

The ISOD weak formulation is obtained by adding to the governing equations an integral formulation of an adequate diffusion tensor. This tensor propagates the artificial viscosity on the perpendicular plane to the iso-values.

Let V be the vector of unknowns,

i.e.: $V=\begin{bmatrix}p\\u\\v\\w\\T\\\tilde{v}\end{bmatrix}$

We choose p instead of ρ so that our formulation is valid for both compressible and uncompressible flows. The term added to the system of equations is:

$$\sum_e\left(\int_{\Omega^e}\nabla W\cdot\left(B^\varepsilon\nabla V\right)d\Omega-\int_{\partial\Omega^e\cap\Gamma}W\left(B^\varepsilon V\right)\cdot\vec{n}d\Gamma\right)$$

where $B_g^\varepsilon=\varepsilon\left(I-A_g\right)$

$$A_g\left(V\right)=\begin{bmatrix}\lambda_{1,1}(V) & 2\lambda_{1,2}(V) & 2\lambda_{1,3}(V)\\2\lambda_{2,1}(V) & \lambda_{2,2}(V) & 2\lambda_{2,3}(V)\\2\lambda_{3,1}(V) & 2\lambda_{3,2}(V) & \lambda_{3,3}(V)\end{bmatrix}$$

$$\lambda_{i,j}(V)=\frac{(\partial_{xi}V)(\partial_{xj}V)}{(\|\nabla V\|)^2}$$

The superscript g designates that we deal with the global (reconstructed) derivatives (versus local derivatives). In our FEM we use an implicit formulation, so the tensor $B_g^\varepsilon(V)$ is estimated at time step n when we compute for V^{n+1}. This linearization makes sense since we diffuse along the iso-values of the solution at a given time step to prevent oscillations of the next time step solution.

3.2. Results

3.2.1. Validations of the basic model

Flow calculation around a flat plate at $\mathrm{Re}_\theta \approx 10^4$ has been performed to compare the solution obtained with FENSAP and the solution obtained with a finite difference boundary layer code, published in AIAA paper 92-0439[43] Both methods have been performed using the Spalart-Allmaras model. The comparison presented in figure 3.1 is only made to validate the coding inside FENSAP and check the calibration of the model closure coefficients.

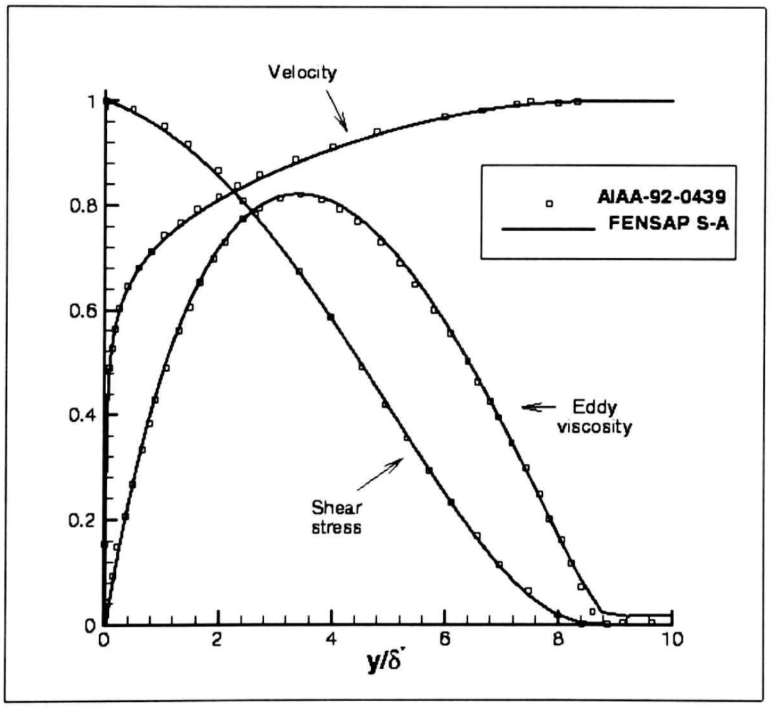

Figure 3.1: Profiles in a flat-plate boundary layer at $\mathrm{Re}_\theta \approx 10^4$, outer coordinates. U normalized with U_∞, τ with τ_{wall} and ν_t with $0.025U_\infty\delta^*$. Comparison of the Spalart-Allmaras model in FENSAP and the calibration results contained in the AIAA paper 92-0439 (figure 4).

The velocity profile in inner coordinates $u^+ = f(y^+)$ is seen in figure 3.2 for three different Reynolds numbers: $\mathrm{Re}_\infty = 1.4\times10^6$, $\mathrm{Re}_\infty = 2.7\times10^6$ and $\mathrm{Re}_\infty = 5\times10^6$. The logarithmic curves show clearly that the velocity profiles obtained with FENSAP using the S-A model are in good agreement with the linear velocity profile for the viscous sublayer, the log-law for the logarithmic region and the experiments[46] for the wake.

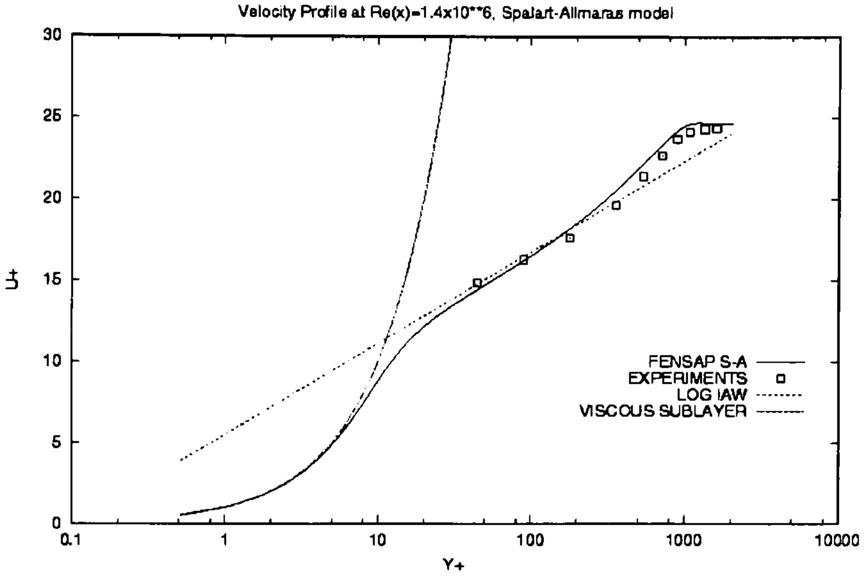

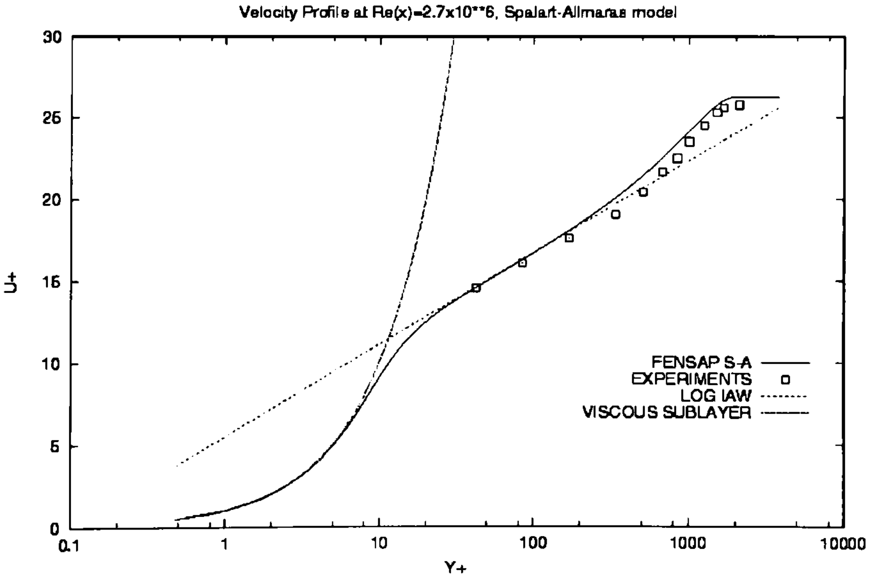

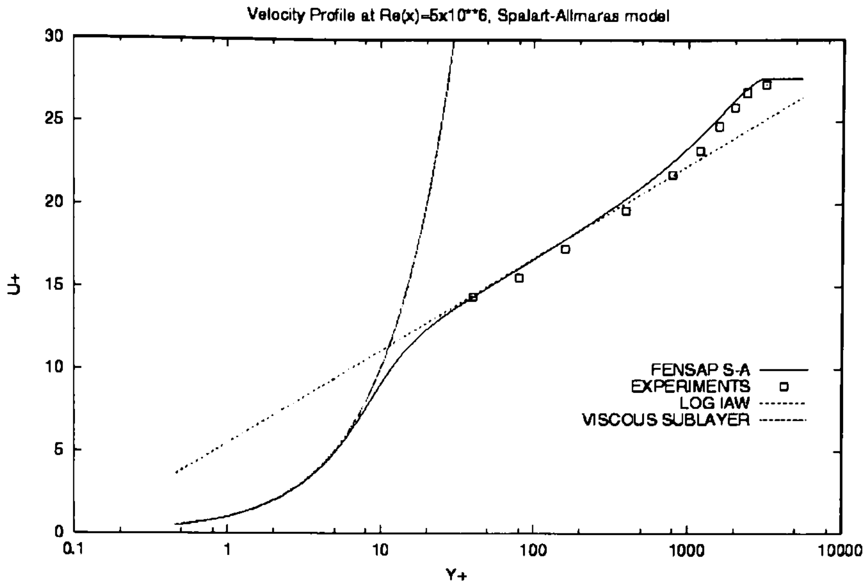

Figure 3.2: Velocity profiles in a Flat-plate boundary layer in inner coordinates (u^+, y^+) for three Reynolds number: $\mathrm{Re}_\infty = 1.4\times10^6$, $\mathrm{Re}_\infty = 2.7\times10^6$, $\mathrm{Re}_\infty = 5\times10^6$. Comparison with theoretical law and experimental data.

To test the model in flow fields with pressure gradients and streamline curvature, two transonic flows over a RAE 2822 airfoil are performed. This flow regime is not completely relevant to the icing problem, since icing conditions deal with lower Mach numbers. The intention here is more to increase the confidence in the model. The first test case is set at Mach number 0.725 and the second at Mach number 0.75. Both test cases include a shock wave. The grid spacing in the direction normal to the wall is fixed at $5\times10^{-6}c$ which correspond on average at $y^+ \approx 1$. A 3D C-type mesh of one element thickness containing 44654 nodes is shown in figure 3.3. The Mach number contours corresponding to the test cases are presented in figure 3.4.

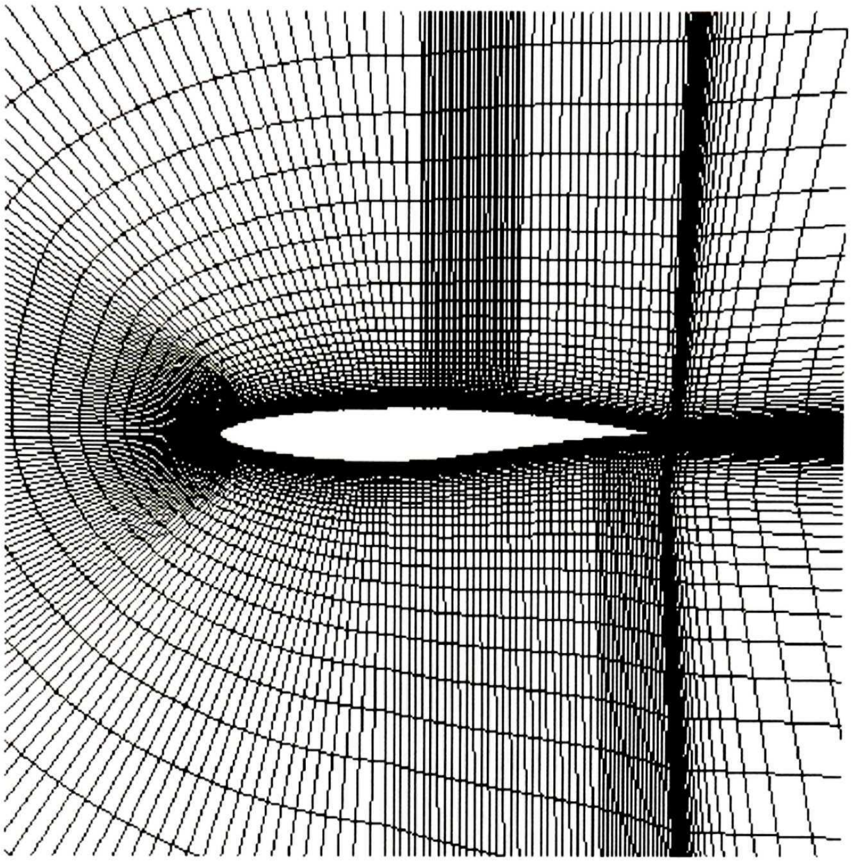

Figure 3.3: Mesh around the RAE 2822 airfoil.

In the first test case the flow parameters are: $Ma = 0.725$, $AoA = 2.37^{o}$, and $\mathrm{Re} = 6.5\times10^{6}$. The predicted and experimental pressure distributions are presented in figure 3.5. The AoA has a strong influence on the shock location, and unfortunately the effective experimental AoA is uncertain in this case (Ref. 43 and 44). Thus the shock location is not necessarily a reliable indicator of solution quality. Nevertheless, the predicted pressure distribution agrees reasonably well with the experimental one. This test case shows that the model works also in cases more complex than a flat plate. However, not much can be said about the accuracy, due to the uncertainties of the experiments.

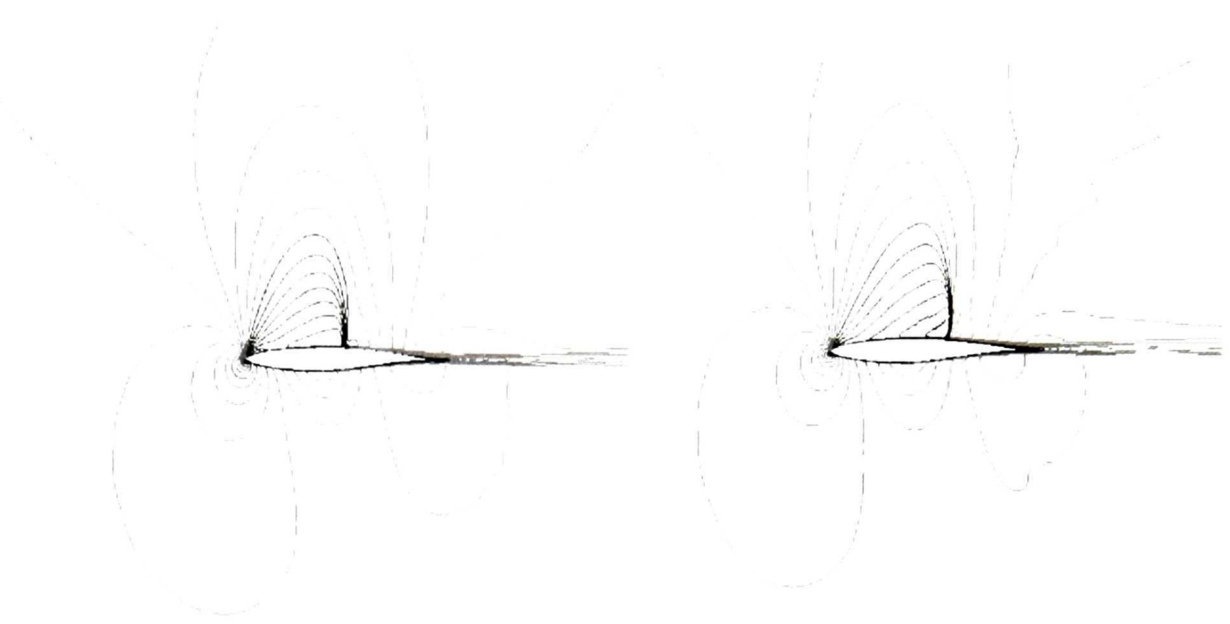
a) b)

Figure 3.4: Mach number contours around the RAE 2822 airfoil ; a) $Ma = 0.725 \quad AoA = 2.37^o$ **and** $\text{Re} = 6.5 \times 10^6$ **; b)** $Ma = 0.75$, $AoA = 2.52^o$, **and** $\text{Re} = 6.2 \times 10^6$.

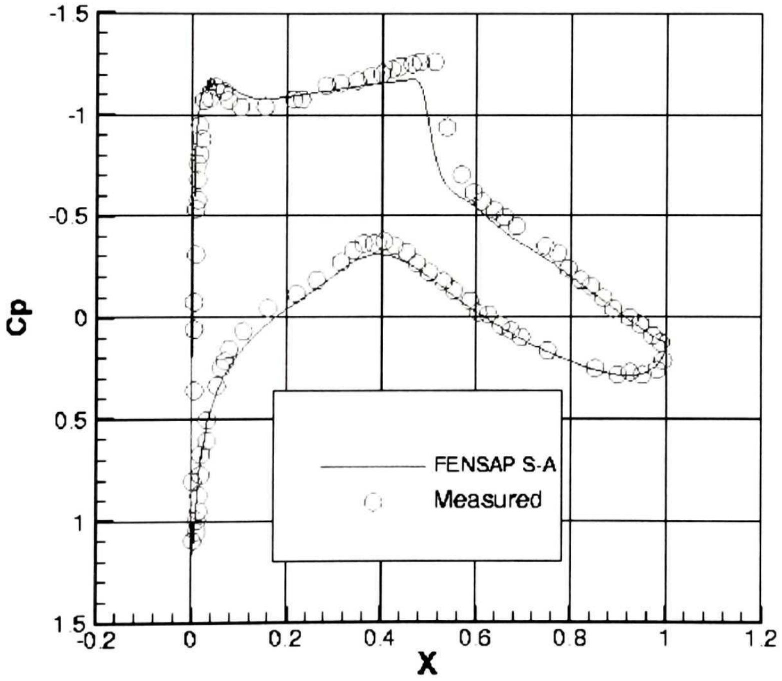

Figure 3.5: Pressure coefficient distribution corresponding to the following conditions:

$Ma = 0.725$, $AoA = 2.37^o$, **and** $\text{Re} = 6.5 \times 10^6$.

In the second test case the flow parameters are: $Ma = 0.75$, $AoA = 2.52^o$, and $\mathrm{Re} = 6.2\times10^6$. The predicted pressure distribution is compared to experiments and pressure distribution of the Cebeci-Smith model in figure 3.6. The shock location predicted with S-A is closer to the experimental shock location than the Cebeci-Smith prediction. But again, it should be remembered that the experimental AoA is uncertain. Both models predict a stronger shock than the experiment. Globally, the S-A pressure distribution agrees well with the Cebeci-Smith prediction and the experiments. As a conclusion of these two test cases, the S-A model can be used to model turbulence around more complex geometries than a flat plate (like airfoils) even in the transonic flow regime.

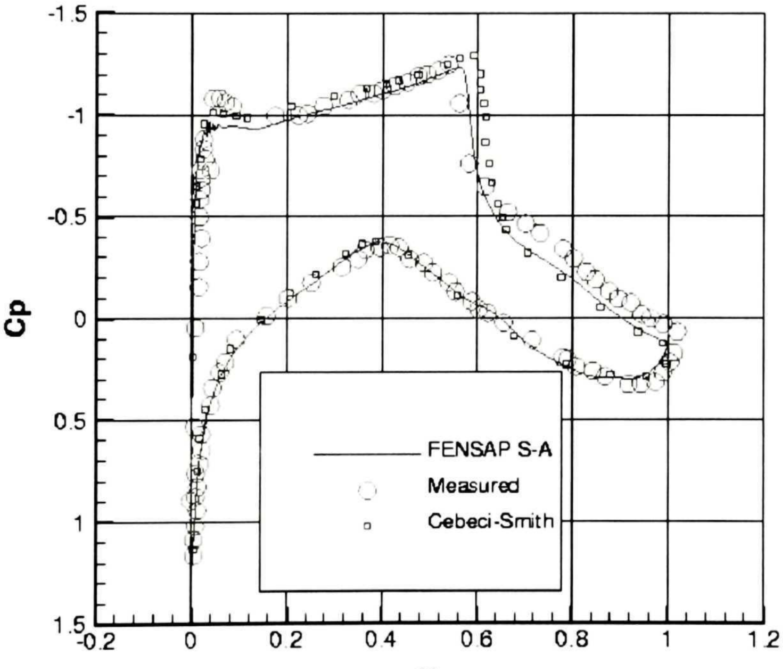

Figure 3.6: Pressure coefficient distribution corresponding to the following conditions:

$Ma = 0.75$, $AoA = 2.52^o$, **and** $\mathrm{Re} = 6.2\times10^6$.

3.2.2. Rough wall treatment with the S-A model

This extension of the model[47] is essential in icing studies and requires non-zero wall values of $\tilde{\nu}$ and ν_T. The d function is increased, relative to the minimum distance $d_{\min}$:

$$d = d_{\min} + 0.03k_s$$

In the last equation, 0.03 is near $\exp(-8.5\kappa)$, and 8.5 is the asymptote of the theoretical log-law intercept, in k_s units, as $k_s^+ \to \infty$.

The solution for a standard constant-stress layer is the same as for smooth walls:

$$\tilde{\nu} = \kappa u_\tau d$$

which requires the mixed wall boundary condition:

$$\frac{\partial \tilde{\nu}}{\partial n} = \frac{\tilde{\nu}}{d}$$

To adjust the model and achieve good predictions for smaller roughness, the $f_{\nu 1}$ function is altered by adding a shift on the function χ, which becomes:

$$\chi = \frac{\tilde{\nu}}{\nu} + c_{R1}\frac{k_s}{d}$$

The suggested value for c_{R1} is 0.5 (Ref. 47). The definition of $\tilde{S}$ is adjusted so that $\tilde{S} = \frac{u_\tau}{\kappa d}$ still down to the wall.

$$\tilde{S} = S + \frac{1}{\mathrm{Re}_\infty}\frac{\tilde{\nu}}{\kappa^2 d^2} f_{\nu 2}, \qquad f_{\nu 2} = 1 - \frac{\tilde{\nu}/\nu}{1 + \frac{\tilde{\nu}}{\nu} f_{\nu 1}}.$$

3.2.2.1. Modification of the surface integrals for roughness

Instead of having a Dirichlet boundary condition $\tilde{\nu} = 0$ at the wall, we impose a Robin boundary condition. Inside the residual $r_{\tilde{\nu}}$ the wall surface integrals become:

$$\int_S W\left\{\frac{1}{\sigma \mathrm{Re}_\infty}(\nu+\tilde{\nu})\frac{\partial \tilde{\nu}}{\partial x_j}n_j\right\}dS = \int_S W\left\{\frac{1}{\sigma \mathrm{Re}_\infty}(\nu+\tilde{\nu})\frac{\tilde{\nu}}{d}\right\}dS$$

with $d = 0.03K_s$ for all the wall nodes.

3.2.2.2. Calibration of the roughness model and validation

The convective heat transfer coefficient, strongly related to the surface roughness, influences the growth, shape and type of ice accretion. When the sandgrain roughness is increased the convective heat transfer will also increase, producing rime ice accretion. In contrast, when the sandgrain roughness decreases, the convective heat transfer will also decrease and only a fraction of the incoming droplets freezes on impact, producing glaze ice accretion.

The logarithmic velocity profile of a boundary layer upon a rough surface has the form[48]:

$$u^+ = \frac{1}{\kappa}\ln y^+ + B - \Delta B$$

where

$$u^+ = \frac{u}{u_\tau} \qquad y^+ = \frac{y u_\tau}{\nu}$$

and the constants defined by $\kappa = 0.41$ and $B = 5$.

The correction added to the constant B, ΔB, is related to the roughness coefficient by the following formula:

$$\Delta B = \frac{1}{\kappa}\ln k_s^+ - 3.65 \qquad k_s^+ = \frac{u_\tau k_s}{\nu}.$$

The logarithmic velocity profile can then be directly related to the roughness coefficient by:

$$u^+ = \frac{1}{\kappa}\ln\frac{y}{k_s} + 8.5 \tag{3.5}$$

The agreement of the computed velocity profiles with Nikuradse's universal profiles, equation (3.5), in the log layer is shown in figure 3.7. The S-A model agrees pretty well with Nikuradse's profile.

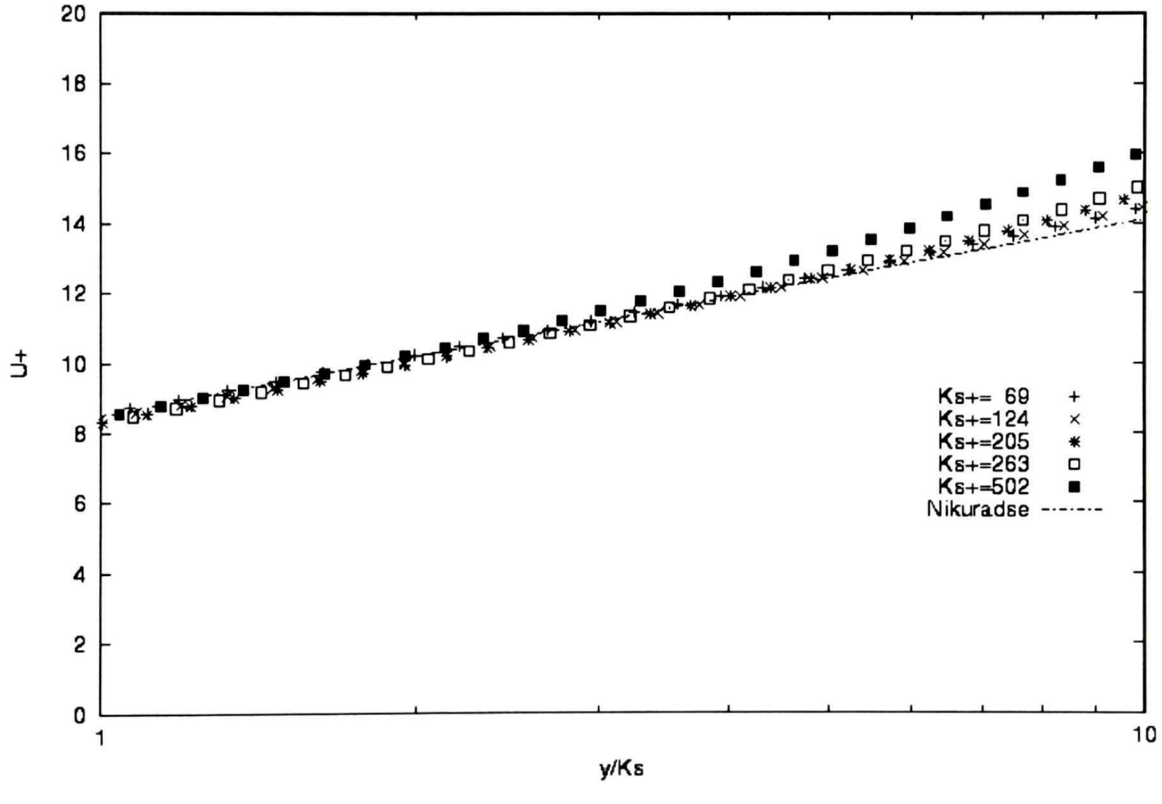

Figure 3.7: Velocity profiles u^+ as a function of $\frac{y}{k_s}$ according to the S-A model compared with Nikuradse's profile.

Mills and Hang[48] have deduced a semi-empirical formula for the skin-friction coefficient on a sand-roughened flat plate:

$$c_f = \left(3.476 + 0.707 \ln \frac{x}{k_s}\right)^{-2.46} \tag{3.6}$$

In figure 3.8, the computed c_f −curves are compared with equation (3.6). The S-A model gives results quite close to the results obtained from equation. (3.6).

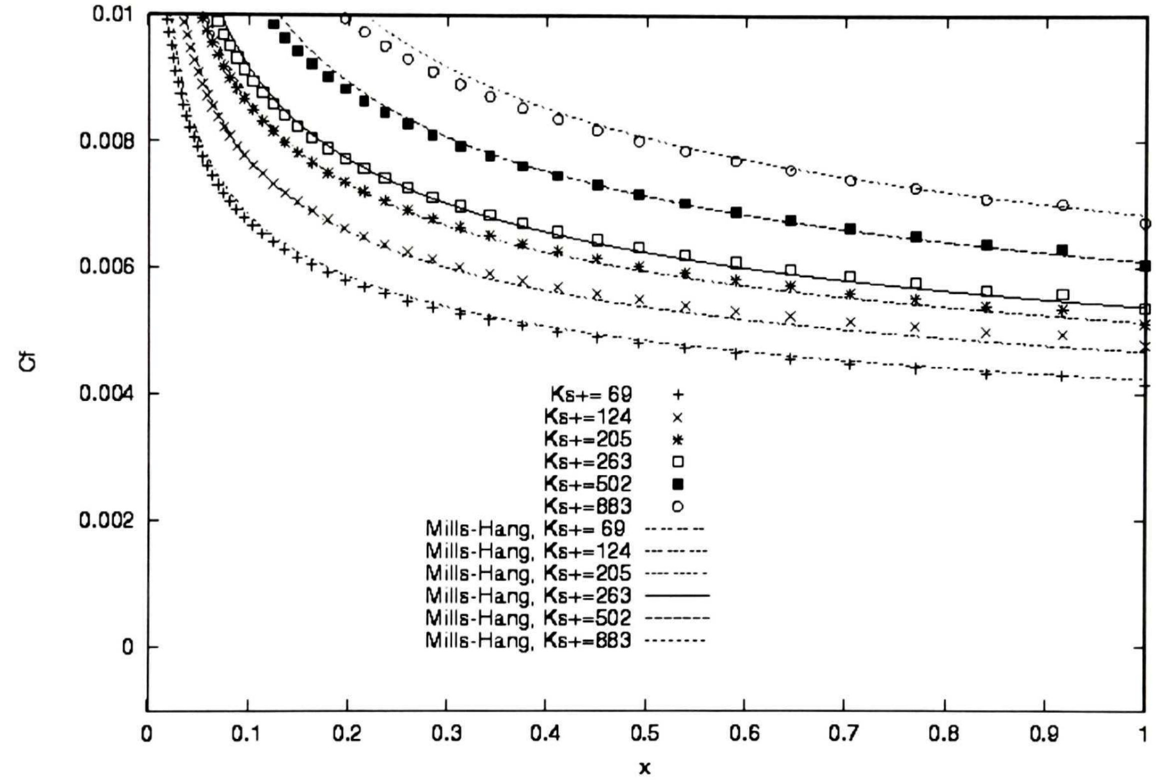

Figure 3.8: Skin friction coefficients for fully-rough plates obtained with S-A compared with equation (3.6).

In figure 3.9, the experiments performed by Blanchard[49] are compared to FENSAP and ONERA[50] results. In the experiments, the surface is covered with hemispheres with a spacing of four times their height. For an external velocity of 58 m/s, the reduced equivalent sandgrain roughness k_s^+ is about 50. In this case, the Stanton number is fairly well reproduced by S-A in the three codes.

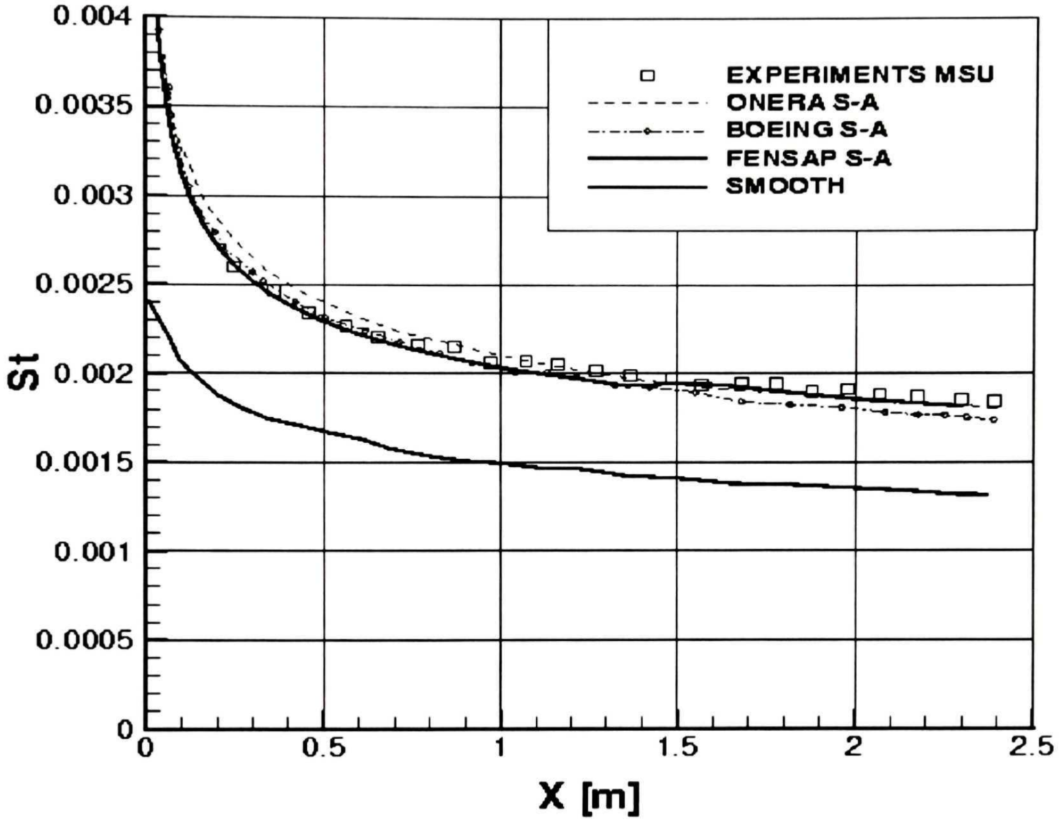

Figure 3.9: Stanton number predictions, MSU experiments, 58 m/s comparison between S-A ONERA, S-A Boeing and S-A FENSAP.

The velocity gradient near a rough pipe wall is less steep than that near a smooth one, as can been seen in figure 3.10, in which the velocity ratio u/U obtained with FENSAP S-A has been plotted against the distance ratio y/R for a smooth and for several rough pipes. All have been compared to the measurements and show good agreement of FENSAP S-A with experimental data.

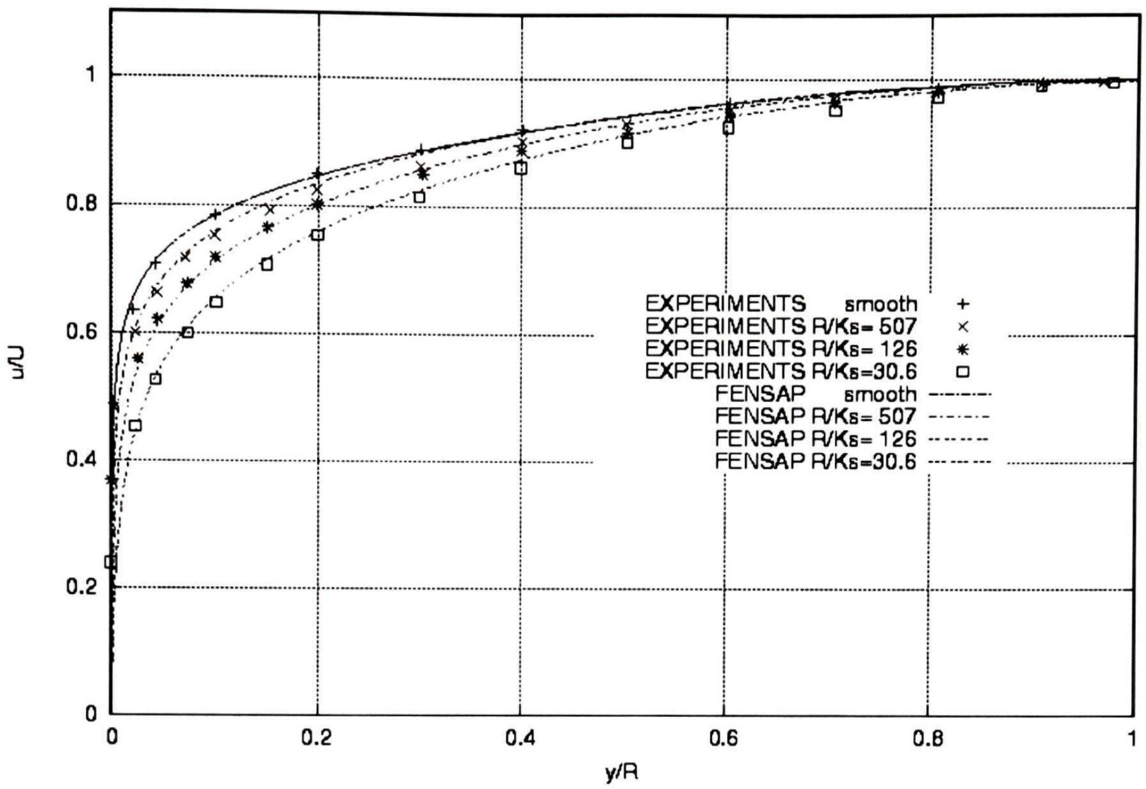

Figure 3.10: Velocity profiles distribution in rough pipes, comparison with Nikuradse[51].

3.3. Influence of roughness on ice shape

Ice shapes are strongly influenced[52, 53] by the convective heat transfer rate from the ice surface. As described previously, the S-A model can predict turbulence on rough surfaces according to an equivalent sandgrain roughness parameter provided. Traditionally in icing simulation, roughness of the iced surface is taken into account with an equivalent sandgrain roughness parameter. This roughness will increase the skin friction, the heat transfer rate and will also modify the transition from laminar to turbulence flow.

Changing the size of the roughness parameter will modify the convective heat transfer rate and will influence the growth rate, shape and type of ice. When the sandgrain roughness is increased, the convective heat transfer will also increase, producing rime ice accretion. When it is decreased the convective heat transfer will decrease and only a fraction of the droplets freezes on impact, producing glaze ice accretion. Therefore, a calculated ice shape can change drastically when various roughness sizes are selected as can be seen in figures 3.11, 3.12 and 3.13.

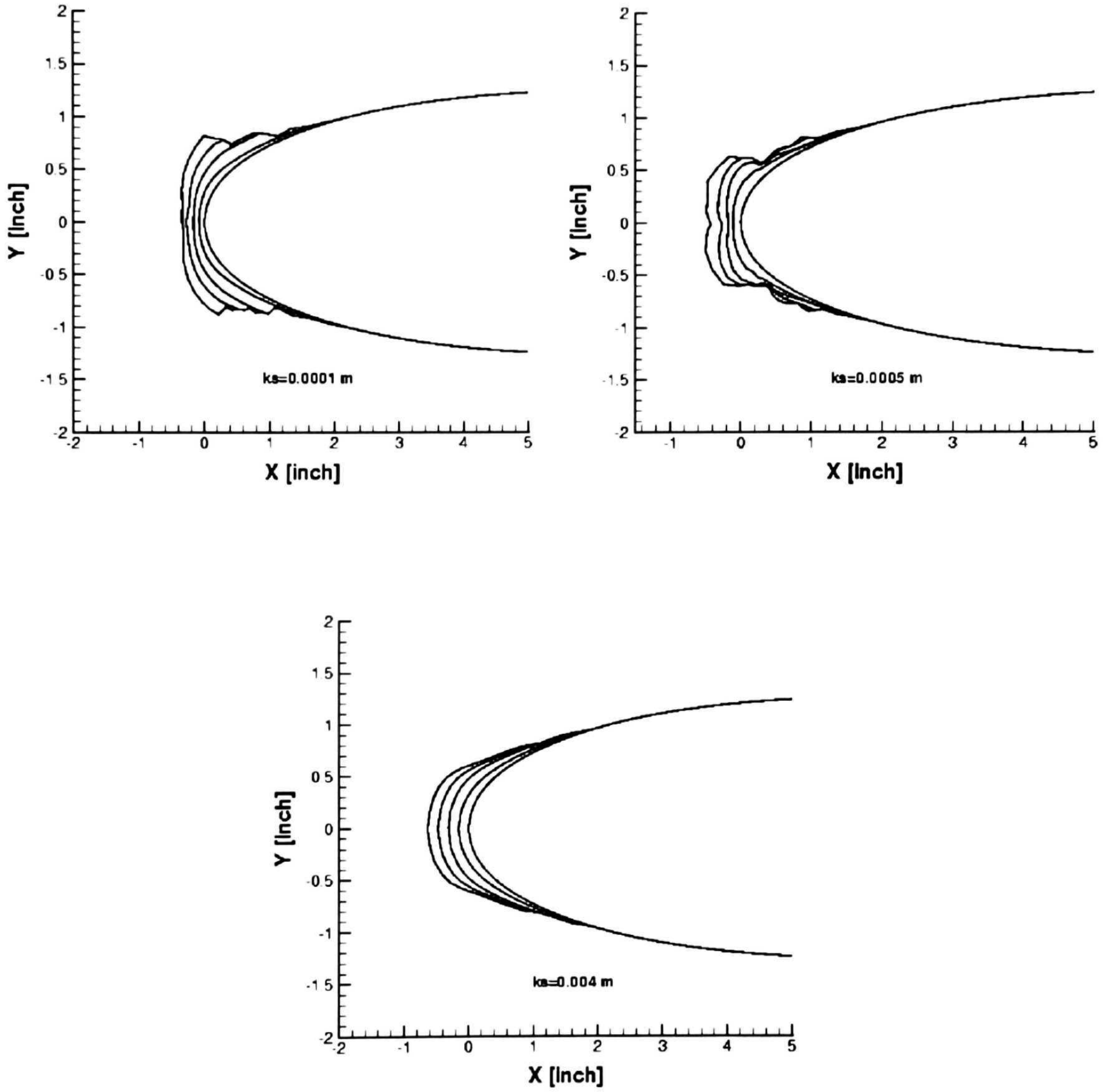

Figure 3.11: Effects of roughness on a NACA 0012 airfoil, the ambient icing conditions are the following: $AOA = 0$ deg, $T_{\infty} = 259.15K$, $U_{\infty} = 93.88 m \cdot s^{-1}$, $d = 30.7 \mu m$, $LWC = 0.94 g \cdot m^{-3}$ **and** $t = 225 s$ **of ice accretion.**

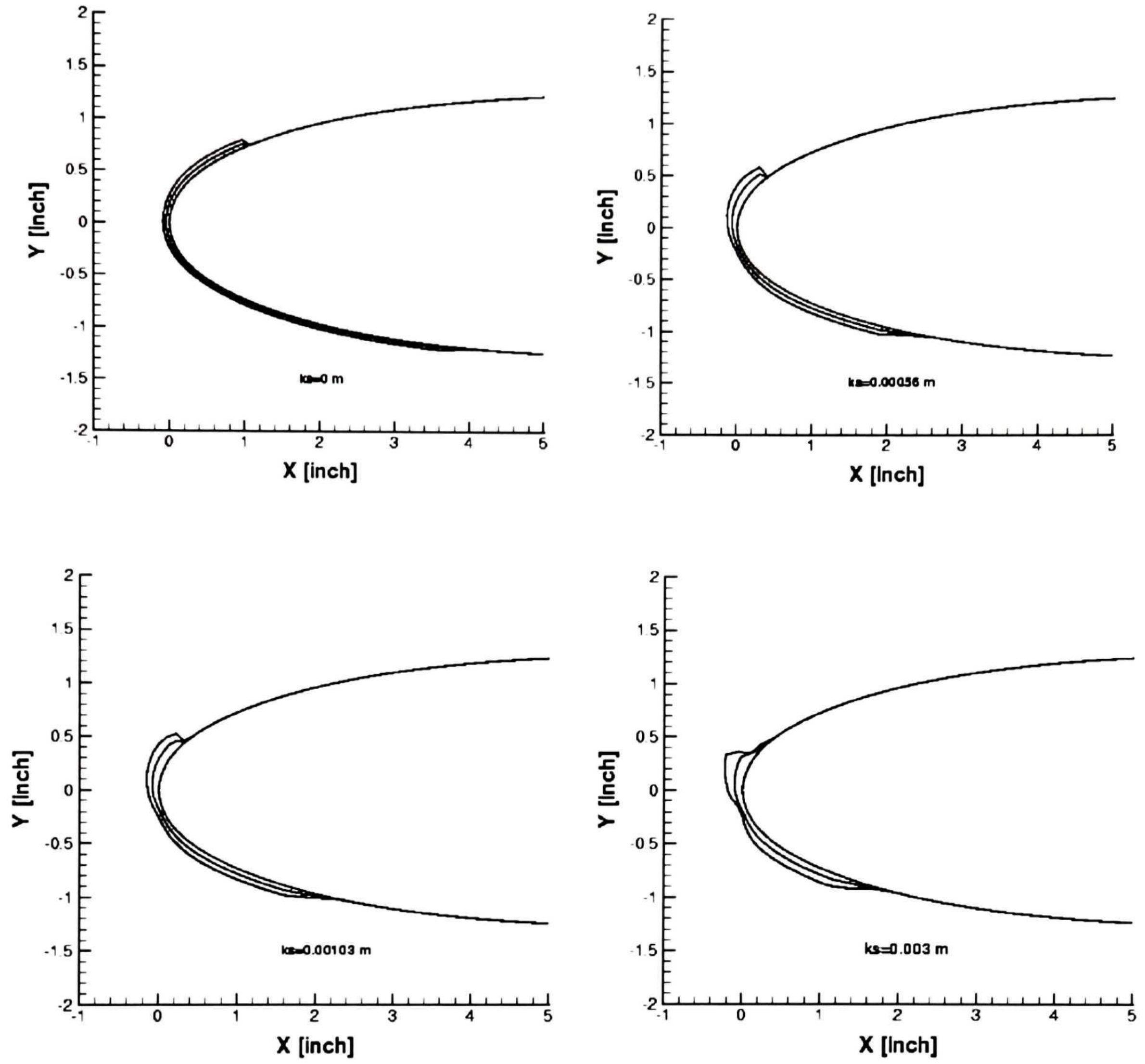

Figure 3.12: Effects of roughness on a NACA 0012 airfoil, the ambient icing conditions are the following: $AoA = 3.5\deg$, $T_\infty = 262.04\,K$, $U_\infty = 102.8\,m \cdot s^{-1}$, $LWC = 1\,g \cdot m^{-3}$, $d = 20\,\mu m$ **and** $t = 91\,s$ **of ice accretion.**

Empirical correlations can be found in the literature to evaluate the effect of roughness, but these correlations exist only for a well-defined type of roughness element. Furthermore, they are not relevant for ice accretion calculations. In icing, the roughness sizes can vary with the ambient icing conditions, the location on the body surface and the length of accretion time. The influence of these parameters on roughness is complex and remains a specialized active research field. Because of the roughness influence on ice shape, all computational icing codes face the problem of defining the most appropriate sandgrain roughness for given icing conditions.

It has become almost the norm that icing codes develop their own empirical correlation for surface roughness. The procedure followed is to first predict the ice shapes for a set of experimental ice shapes and convective heat transfer coefficient (or roughness parameter). Then they determine the value of roughness that yields the best agreement with the experiments.

An empirical correlation relating the surface roughness equivalent sandgrain parameter had been developed for LEWICE, equation (3.7). As a first approximation, this correlation will be used inside our flow solver. The equations determining this correlation are the following:

Velocity

$$\left[\frac{k_s / c}{k_s / c)_{base}}\right]_{V_\infty} = 0.4286 + 0.0044139(V_\infty)$$

Liquid water content

$$\left[\frac{k_s / c}{k_s / c)_{base}}\right]_{LWC} = 0.5714 + 0.2457(LWC) + 1.2571(LWC)^2$$

Static temperature

$$\left[\frac{k_s/c}{k_s/c)_{base}}\right]_{T_s} = 46.8384\left(\frac{T_s}{1000}\right) - 11.2037$$

In all equations, $k_s/c)_{base}$ is set to 0.00117, the velocity is in m/s, the LWC in g/m^3 and the static temperature is in K. The value of the sandgrain roughness is the following:

$$k_s = \left[\frac{k_s/c}{k_s/c)_{base}}\right]_{V_\infty} \left[\frac{k_s/c}{k_s/c)_{base}}\right]_{LWC} \left[\frac{k_s/c}{k_s/c)_{base}}\right]_{T_s} k_s/c)_{base}c \tag{3.7}$$

This equivalent sandgrain roughness may be recomputed at each update of the airflow solution to account for the variation in ice shape and roughness.

Figure 3.13 shows ICE3D-SWIM accretion with smooth wall and with roughness, along with LEWICE results and experimental ones obtained by NASA in the IRT (Ref. 66). The ICE3D-SWIM results have been calculated using a one shot ice accretion technique and first show that roughness has a significant effect on accretion. As can be noticed when no roughness is used, the convective heat transfer is not sufficient to freeze the impinging water on impact and the remainder runs back along the geometry. The figure 3.13 also shows that using the S-A model with LEWICE roughness parameter seems to be a judicious choice to solve our problem. Referring to chapter 5 about the quality of experiments in icing we observe good agreement of ICE3D-SWIM results with the experimental data. Concerning the comparison to LEWICE solution, it should be recalled that only a one shot ice accretion has been done with ICE3D-SWIM, LEWICE did seven layers, which could explain the discrepancies between the two solutions .

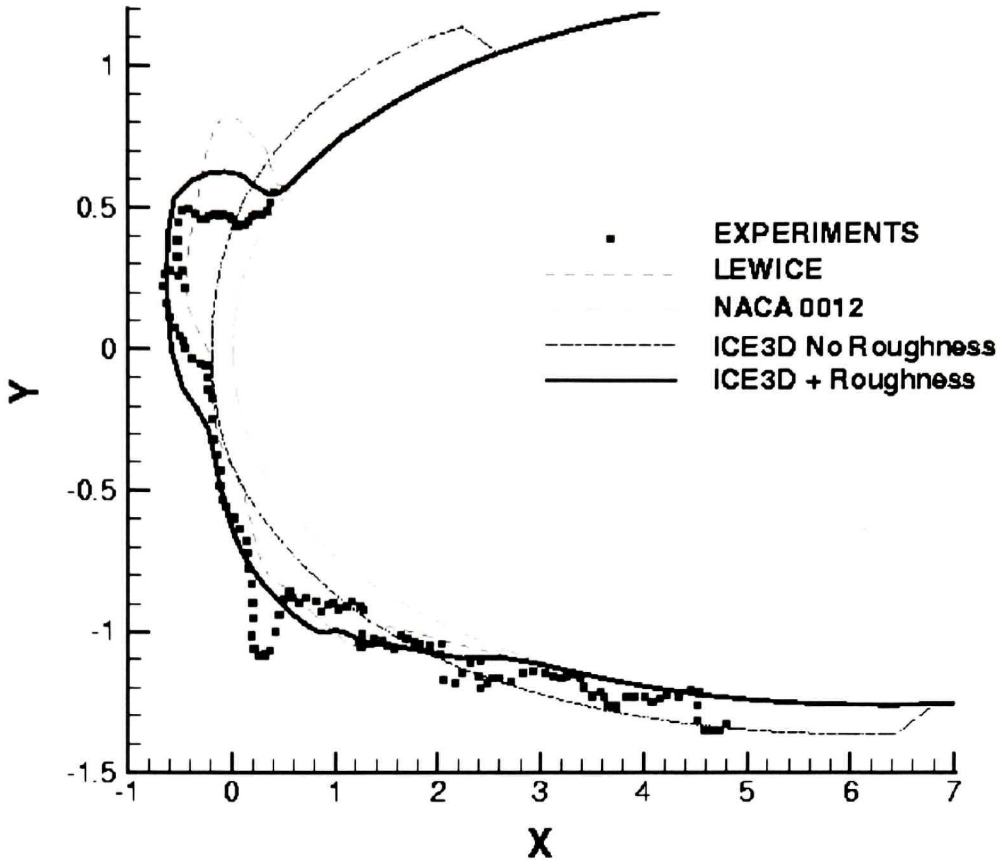

Figure 3.13: Effects of roughness on ice shapes, comparison with LEWICE and the experiments on a NACA 0012 airfoil, Run 209. The ambient icing conditions are the following: $AOA = 3.5\,\text{deg}$, $T_\infty = 265.07\,K$, $U_\infty = 130.3\,m \cdot s^{-1}$, $LWC = 1.3\,g \cdot m^{-3}$, $d = 30\,\mu m$ **and** $t = 360\,s$ **of ice accretion.**

3.4. Conclusions

The one-equation turbulence model developed by Spalart and Allmaras has been implemented in the three-dimensional finite element flow solver FENSAP. The coding has been verified by solving the boundary layer over a flat plate. The surface roughness has been taken into account and validated against numerical and experimental results. Its effect on ice shape has been demonstrated through test cases. It should be kept in mind that, as every turbulence models based on the Boussinesq approximation, this model also has limitations[40]. Nevertheless the present model appears to be robust and easy to use. The good agreement of the results with theory and experiments are encouraging and makes it a valuable tool for icing simulations. All the results presented in this thesis have been obtained using this turbulence model.

Chapter 4

A PDE-Based Ice Accretion Module

For the ice accretion calculation, heat and mass transfer at the body surface is taken into account. The model should contain all the physics that cause ice formation from rime to glaze, including conditions categorized as mixed. Glaze and mixed ice form when there is no sufficient heat transfer to immediately freeze all impinging water droplets, with some water running back along the dry surface or the existing ice layer and freezing further downstream. The convective heat transfer controls ice accretion in this case and the thermodynamic model used[54] is the Messinger[28] formulation that satisfies the first law of thermodynamics in terms of conservation of mass and energy in a control volume. In this work, we will derive a continuous form of these equations for the liquid water film and these partial differential equations will be shown to be close to the well-known shallow water equations, with the addition of source terms corresponding to the other water phase: solid and vapor. Their discretization, using the finite volume approach in this case, will be described.

It should be noted that in this chapter, a tilde over any temperature indicates the temperature to be in degrees Celsius, otherwise the temperature is in degrees Kelvin.

4.1. Physical model

Let us define a fixed control volume V contained between the curvilinear surfaces S and S', figure 4.1 representing the clean body geometry and the geometry once ice is accreted. S' is the normal projection of S, the distance between S and S' being the height of the liquid water film.

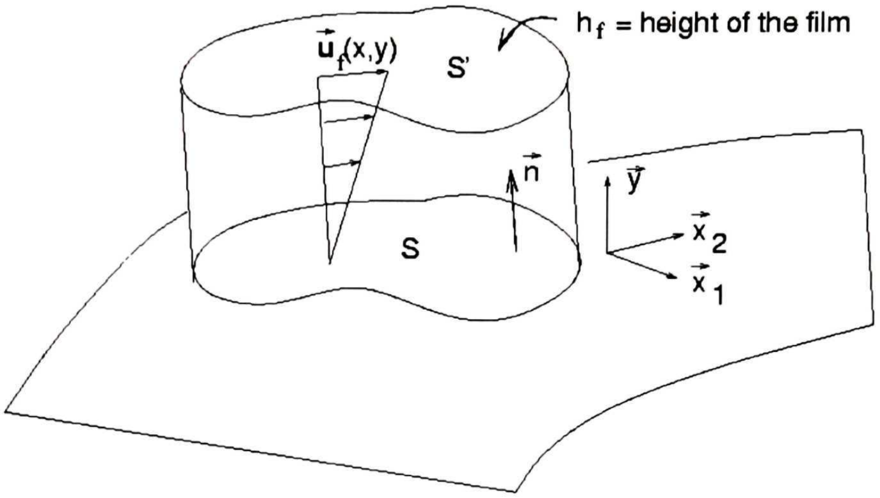

Figure 4.1: ICE3D-SWIM control volume.

The velocity of the water film is a function of the coordinates $\vec{x} = (x_1, x_2)$ on the surface and y normal to the surface, in other words fully 3D. The problem can be simplified by introducing a linear velocity profile for the film, $\vec{u}_f = (\vec{x}, y)$, tangent to the wall, with a zero velocity at the wall:

$$\vec{u}_f = \frac{y}{\mu_w} \vec{\tau}_{wall}(\vec{x}, y). \tag{4.1}$$

Such a linear velocity profile assumption is justified by thin film theory in which terms of order higher than one in the velocity profile are negligible. The small film thickness, seldom greater than 10 μm in icing or anti-icing simulations[55], would support this approximation.

In equation (4.1), $\vec{\tau}_{wall}$, the shear stress of the air, is the main driven force for the water film; the pressure and gravity forces being negligible except close to the stagnation point and at low velocities. For example, when the pressure force is considered:

$$\vec{u}_f = y\left(\frac{\vec{\tau}_{wall}(x,y)}{\mu_w} - \frac{h_f}{y}\frac{d\vec{p}}{ds}\right). \tag{4.2}$$

At a stagnation point in 2D the dimensionless pressure gradient is defined by:

$$-\frac{s}{\rho u_e^2}\frac{d\vec{p}}{ds} = 1, \tag{4.3}$$

where u_e is the velocity just outside the boundary layer and s the distance from the stagnation point. Pressure forces are negligible if:

$$\vec{\tau}_{wall} >> h_f \frac{d\vec{p}}{ds}. \tag{4.4}$$

When the definition of the friction coefficient and equation (4.3) are used, equation (4.4) becomes

$$0.5c_f >> h_f / s. \tag{4.5}$$

For a small water film thickness, the pressure gradient could have an effect only very close to the stagnation point. With similar arguments, the gravity force can be shown to be negligible except in the vicinity of a stagnation point (Ref. 15).

By averaging across the film thickness, a mean velocity can thus be derived:

$$\bar{u}_f = \frac{1}{h_f}\int_0^{h_f} \vec{u}_f(\vec{x}, y)dy = \frac{h_f}{2\mu_w}\vec{\tau}_{wall}(\vec{x}, y) \tag{4.6}$$

In addition, because the water film is very thin, temperature changes in the direction normal to the wall are small and a constant average temperature through the water film is used. Equation (4.6) will be used to derive a system of partial differential equations for mass and energy conservation.

4.1.1. Mass conservation

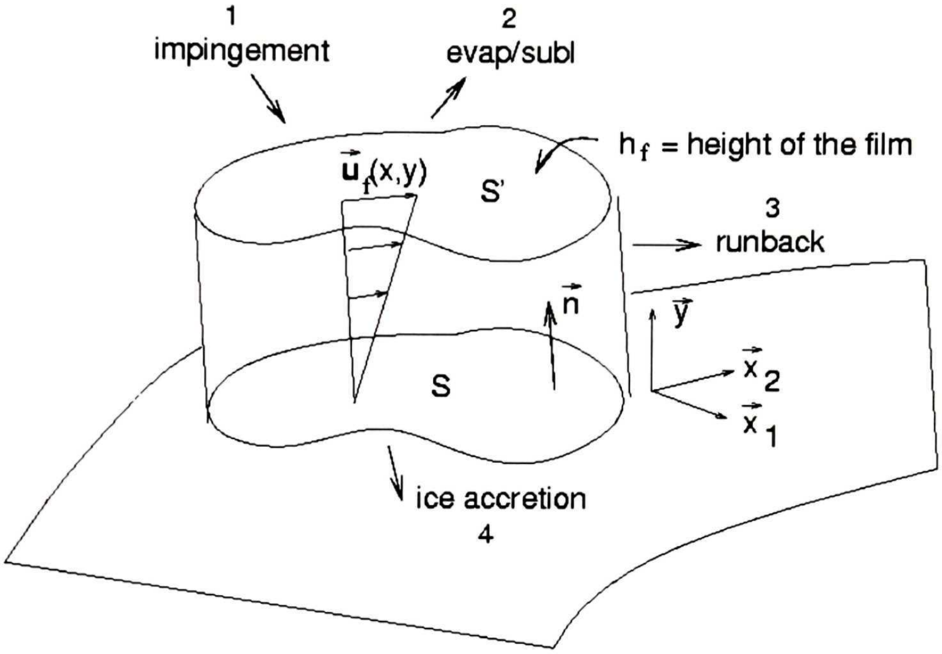

1.	Impinging water	$\dot{m}_\beta$
2.	Evaporation/Sublimation	$\dot{m}_{evap}$
3.	Water runback through V	$\dot{m}_F$
4.	Ice accretion leaving V	$\dot{m}_{ice}$

Figure 4.2: Mass balance for a control volume.

An evaluation of all the mass of water entering and leaving the control volume is shown in figure 4.2. A mass balance equation can be formed from these terms:

$$\dot{m}_v + \dot{m}_F = \dot{m}_\beta + \dot{m}_{evap} + \dot{m}_{ice} \tag{4.7}$$

The following assumptions have been made to simplify the problem:

- The mass of air trapped inside the solid ice is neglected. It is supposed that no reaction occurs between air and water and that no air is dissolved in water.
- The main driving force of the film is the frictional force.

- The properties are constant inside the control volume.

We can evaluate and express each term of equation (4.7) in the following manner:

Liquid water film

The Reynolds transport theorem applied to the liquid water film states that:

- The rate of change of liquid water within the control volume is:

$$\dot{m}_v = \frac{\partial}{\partial t}\int_0^{h_f}\int_S \rho_w d\bar{x}dy = \rho_w \frac{\partial}{\partial t}\int_S \int_0^{h_f} dy d\bar{x}$$

- The flux of liquid water passing into and out the control surface is:

$$\dot{m}_F = \int_{\partial S}\int_0^{h_f} \rho_w \vec{u}_f(\vec{x},y,t)\cdot\vec{n}(\vec{x})dyd\bar{x} = \frac{\rho_w}{2\mu_w}\int_S div\left(\vec{\tau}_{wall}(\vec{x},t)h_f^2(\vec{x},t)\right)d\bar{x}$$

Impinging water due to impacting droplets

$$\dot{m}_\beta = U_\infty LWC\int_{S'}\beta(\vec{x},t)d\bar{x} \approx U_\infty LWC\int_S \beta(\vec{x},t)d\bar{x}$$

It is assumed that the impinging water is uniformly distributed on the lower surface of the control volume.

Evaporation/Sublimation

$$\dot{m}_{evap} = -\int_{S'}\dot{m}''_{evap}(\vec{x},t)d\bar{x} \approx -\int_S \dot{m}''_{evap}(\vec{x},t)d\bar{x}$$

We assume that the evaporation is uniformly distributed on the lower surface of the control volume. The mass rate of water lost by evaporation/sublimation, $\dot{m}''_{evap}$, is recovered from a parametric model expressed in the following section, equation 4.9.

Ice accumulation

As previously discussed, the control volume remains on the surface of the geometry as the ice accumulates outside the control volume. Therefore the mass rate of water leaving the control volume by freezing can be expressed as:

$$\dot{m}_{ice} = -\int_S \dot{m}''_{ice}(\vec{x},t)d\vec{x}$$

A partial differential equation for mass conservation

For every volume V , i.e. every surface S , we have:

$$\int_S \left(\rho_w \left[\frac{\partial h_f}{\partial t} + div\left(\bar{u}_f h_f\right)\right]\right) d\vec{x} = \int_S \left(U_\infty LWC\beta - \dot{m}''_{evap} - \dot{m}''_{ice}\right) d\vec{x} \ , \quad \forall S$$

Therefore the conservative form of the mass conservation can be written as follows:

$$\rho_w \left[\frac{\partial h_f}{\partial t} + div\left(\bar{u}_f h_f\right)\right] = U_\infty LWC\beta - \dot{m}_{evap} - \dot{m}_{ice} \qquad (4.8)$$

Where the three terms on the right hand side correspond, respectively, to the mass transfer rate by water droplet impingement (source for the film), the evaporation/sublimation and ice accretion (sinks for the film). For notation simplicity, we omit the " distinction sign concerning the evaporation and the ice mass transfer rates but we will keep in mind that these mass transfer rates are expressed per surface unit.

4.1.2. A parametric model for evaporation

MacArthur[56] gives a relation to calculate the mass flux that evaporates or sublimates as:

$$\dot{m}_{evap} = \frac{0.7h_c}{c_{p,air}}\left[\frac{P_{v,p}(T) - H_{r,\infty}P_{v,\infty}}{P_{wall}}\right] \qquad (4.9)$$

Where $P_{v,p}$ is the saturation vapor pressure at the surface, $P_{v,\infty}$ the saturation vapor pressure of water in ambient air and P_{wall} is the absolute pressure above the control volume outside the boundary layer. $H_{r,\infty}$ is the relative humidity, T the temperature in Kelvin, $c_{p,air}$ the specific heat capacity of air and h_c the convective heat transfer coefficient.

The saturation vapor pressure is calculated using an approximation[57] of the saturated steam table[58] values:

$$P_{v,p} = 3386\left[\ 0.0039 + 6.8096.10^{-6}\hat{T}^2 + 3.5579.10^{-7}\hat{T}^3\right]$$

with $\hat{T} = 72 + 1.8T$

4.1.3. Energy Conservation

The same concept of control volume is used to write the energy balance. The first law of thermodynamics states that:

Energy inflow rate = Energy outflow rate + Energy storage rate

The modes of energy transfer are illustrated in figure 4.3. We use the convention that the energy that flow into the control volume is positive.

To simplify the task we made the following energy assumptions:

- Ice acts somewhat as an insulator[59] ($\dot{Q}_{cond} = 0\ W$):
    - The conduction between the surface and water is neglected.
    - The conduction between neighboring control volumes is also neglected.
- Any heating of the droplet in the air is neglected (Ref. 17).

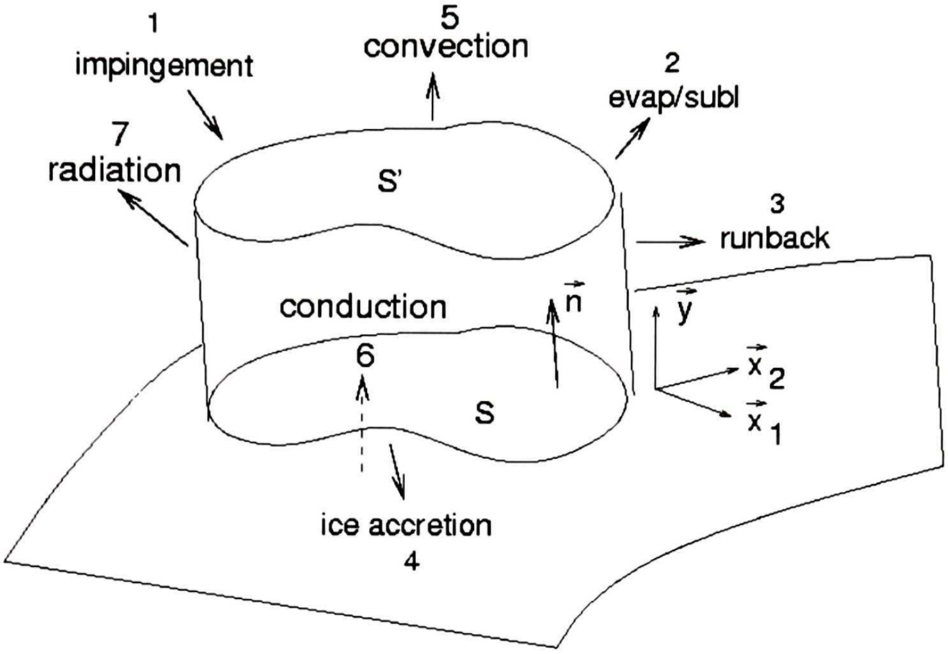

1.	Impinging water	$\dot{Q}_\beta$
2.	Evaporation/Sublimation	$\dot{Q}_{evap}$
3.	Water runback through the CV	$\dot{Q}_F$
4.	Ice accretion leaving the CV	$\dot{Q}_{ice}$
5.	Convection	$\dot{Q}_{conv}$
6.	Conduction	$\dot{Q}_{cond}$
7.	Radiation	$\dot{Q}_{rad}$

Figure 4.3: Energy balance for a control volume.

The energy due to the impact of droplets along with the energy of the water running back from the upstream control volume and the heat released by the freezing water represent the energy flow into the control volume, while the convection, conduction, radiation, evaporation and the energy of the water running out of the control volume represent the energy flow out of the control volume. A general form of the energy equation can be written as follows:

$$\dot{Q}_V + \dot{Q}_F = \dot{Q}_\beta + \dot{Q}_{evap} + \dot{Q}_{ice} + \dot{Q}_{conv} + \dot{Q}_{rad} \tag{4.10}$$

Liquid water film

The water flowing through the control volume at time t will be at the surface temperature $\tilde{T}(\vec{x},t)$. The enthalpy of the water can therefore be defined by $c_{p,w}\tilde{T}(\vec{x},t)$, where $c_{p,w}$ is the specific heat capacity of water. The energy term corresponding to the liquid water film can then be expressed as follows:

$$\dot{Q}_V = \frac{\partial}{\partial t}\int_S \left(\int_0^{h_f} \rho_w c_{p,w} \tilde{T}(\vec{x},t) dy \right) d\vec{x} = \int_S \frac{\partial}{\partial t}\left[\rho_w c_{p,w} h_f(\vec{x},t) \tilde{T}(\vec{x},t) \right] d\vec{x}$$

and after use of equation 4.6:

$$\dot{Q}_F = \int_{\partial S} \left(\int_0^{h_f} \rho_w c_{p,w} \tilde{T}(\vec{x},t) \vec{u}_f(\vec{x},y,t) \cdot \vec{n}_S(\vec{x}) dy \right) d\vec{x} = \frac{\rho_w}{2\mu_w} \int_S div\left(h_f^2 \vec{\tau}_{wall} c_{p,w} \tilde{T}(\vec{x},t) \right) d\vec{x}$$

Impingement

Since droplets are brought to rest when they strike the geometry, it is appropriate to use the stagnation enthalpy to evaluate the energy of the impinging water. The reference for zero enthalpy in this study is water at the freezing point ($T_c = 273.15 K$). The energy flow rate of the impinging water therefore is:

$$\dot{Q}_\beta = \int_S U_\infty LWC\beta \left[c_{p,w}\left(T_{d,\infty} - T_c \right) + \frac{\left\| \vec{u}_d \right\|^2}{2} \right] d\vec{x}$$

where $T_{d,\infty}$ is the droplet temperature at infinity, in degrees Kelvin, and $\left\| \vec{u}_d \right\|^2$ is the square norm of the droplet velocity at impact.

Evaporation/sublimation

Following an approximation of Hedde[15], half of the water is considered liquid and the other half solid when evaporation/sublimation occurs. This simple model should take into account the non-continuity of the liquid water film. It is possible to observe, on the body surface, bumps of ice separated by liquid water. In that case the ice will sublimate and the liquid water will evaporate.

$$\dot{Q}_{evap} = -\int_S \left[\frac{1}{2}\left(L_{evap}(T_c) + L_{sub}(T_c)\right) \dot{m}_{evap} \right] d\vec{x}$$

where $L_{evap}(T_c)$ and $L_{sub}(T_c)$ are the latent heat of evaporation and sublimation respectively evaluated at freezing point.

Notice: $L_{evap}(T_c)$ and $L_{sub}(T_c)$ are of the same order of magnitude. In glaze ice situations (liquid water + ice) LEWICE chooses another approach and considers only the evaporation (assuming the liquid water on the top of the ice layer). This has been also tested in our code but does not improve ice shapes; Hedde's approximation is then used for all the test cases.

Ice accumulation leaving the control volume

The enthalpy of ice is computed referring to the water at 273.15K. The rate of energy leaving the control volume with accumulated ice can be expressed as:

$$\dot{Q}_{ice} = \int_S \dot{m}_{ice}(\vec{x},t) \left[L_{fus}(T_c) - c_{p,ice}\tilde{T}(\vec{x},t) \right] d\vec{x}$$

where $L_{fus}(T_c)$ is the latent heat of fusion and $c_{p,ice}$ is the specific heat capacity of ice.

Convection

The heat lost by convection is:

$$\dot{Q}_{conv} = \int_S \dot{Q}_{S-A}\, d\vec{x} = \int_S k \left.\frac{\partial \tilde{T}_{air}}{\partial \vec{n}}\right|_{wall} d\vec{x}$$

where k is the thermal conductivity of air and $\left.\frac{\partial \tilde{T}_{air}}{\partial \vec{n}}\right|_{wall}$ is the gradient of temperature normal to the wall. The convective heat transfer $\dot{Q}_{S-A}$ provided by the CFD code for turbulent dry air is converted into a heat transfer coefficient, before ice accretion calculations:

$$h_c = \dot{Q}_{S-A} / (T_{ini} - T_\infty).$$

This heat transfer coefficient depends only weakly on the initial surface temperature distribution T_{ini} along the airfoil, but will change depending on the boundary layer thickness. Therefore between each call to the flow solver, the ice accretion module uses a fixed value for $h_c(\vec{x})$ to obtain a convective heat flux $\dot{Q}_h$ that will change with the surface temperature T.

$$\dot{Q}_h = h_c(T - T_\infty)$$

Radiation

The heat lost by radiation is:

$$\dot{Q}_{rad} = \sigma\varepsilon \int_S \left[\ T_\infty^4 - \left(\tilde{T}(\vec{x},t) + T_c\right)^4 \right] d\vec{x}$$

or

$$\dot{Q}_{rad} = \sigma\varepsilon \int_S \left[\ T_\infty^4 - T^4 \right] d\vec{x}$$

where σ is the Boltzman constant and ε the solid's emissivity. The heat losses by radiation are included, although they are important only in anti-icing simulation.

Relative importance of the terms

- Source terms: the heat released by the freezing water represent the most important source term of the energy balance, followed by the energy due to the impact of droplets.
- Sink terms: the convection is the most important term, followed by the evaporation. The heat lost by radiation is negligible and represent less than 1% of the exchange.

Considering all the terms together, the convective heat transfer flux will remain the determining factor for obtaining a realistic ice shape.

A partial differential equation for the energy conservation

The energy terms can now be summed to form the energy equation:

$$\int_S \rho_w \left[\frac{\partial h_f c_{p,w} \tilde{T}}{\partial t} + div\left(\bar{u}_f h_f c_{p,w} \tilde{T}\right) \right] d\vec{x} \;=\; \int_S \left\{ \begin{aligned} & \left[c_{p,w} \tilde{T}_{d,\infty} + \frac{\left\| \bar{u}_d \right\|^2}{2} \right] \times U_\infty LWC\beta + \sigma\varepsilon\left(T_\infty^4 - T^4\right) \\ & - \; 0.5\left(L_{evap} + L_{sub}\right) \dot{m}_{evap} + \left(L_{fus} - c_{p,ice}\tilde{T}\right) \dot{m}_{ice} + \dot{Q}_h \end{aligned} \right\} d\vec{x} \qquad \forall S$$

Therefore the conservative form of the energy equation is:

$$\rho_w \left[\frac{\partial h_f c_{p,w} \tilde{T}}{\partial t} + div\left(\bar{u}_f h_f c_{p,w} \tilde{T}\right) \right] \;=\; \begin{aligned} & \left[c_{p,w} \tilde{T}_{d,\infty} + \frac{\left\| \bar{u}_d \right\|^2}{2} \right] \times U_\infty LWC\beta + \sigma\varepsilon\left(T_\infty^4 - T^4\right) \\ & - \; 0.5\left(L_{evap} + L_{sub}\right) \dot{m}_{evap} + \left(L_{fus} - c_{p,ice}\tilde{T}\right) \dot{m}_{ice} + \dot{Q}_h \end{aligned} \tag{4.11}$$

The coefficients ρ_w, $c_{p,w}$, $c_{p,ice}$, L_{evap}, L_{sub}, L_{fus} are physical properties of water, while $\tilde{T}_{d,\infty}$, U_∞, LWC, and T_∞ are airflow and droplets parameters specified by the user. The ambient icing conditions completely determine these values.

The flow solver provides the local wall shear stress $\vec{\tau}_{wall}$ and the convective heat flux $\dot{Q}_h$.

The Eulerian droplet module provides local values of the collection efficiency β and the droplet impact velocity $\vec{u}_d$.

The evaporative mass flux is recovered from the convective heat flux using the parametric model, equation 4.9.

4.1.4. Compatibility relations

Three unknowns are to be computed: the film thickness h_f, the equilibrium temperature $\tilde{T}$ within the air/water film/ice/wall interface, and the instantaneous mass accumulation of ice $\dot{m}_{ice}$.

Compatibility relations are therefore needed to close the system. Based on physical observations, one way to write them is as follows:

$$\begin{cases} h_f \geq 0 \\ \dot{m}_{ice} \geq 0 \\ h_f \tilde{T} \geq 0 \\ \dot{m}_{ice} \tilde{T} \leq 0 \end{cases} \tag{4.12}$$

The first compatibility relation is a natural assumption on the film thickness, as is the positivity of the air density for a compressible flow. This first assumption is explicitly stated as there is no guaranty, at this time, that the model forces the film thickness to remain positive. The second compatibility relation, although not essential, just prevents the remelting of ice. It could probably be removed in case inward movements of the geometry (for ice remelting) can be properly handled. The last two inequalities ensure that the model predicts no liquid water when the equilibrium temperature is under the freezing point (0°C), and that no ice forms at any temperature above freezing.

4.1.5. Conclusion: system to solve

At the end, to model the thermodynamics of the freezing process on a body undergoing icing, we have to solve the partial differential equations resulting from mass and energy balance, along with the four compatibility relations:

$$\begin{cases} \rho_w \left[\dfrac{\partial h_f}{\partial t} + div\left(\bar{u}_f h_f\right) \right] = U_\infty LWC\beta - \dot{m}_{evap} - \dot{m}_{ice} & (4.8) \\ \rho_w \left[\dfrac{\partial h_f c_{p,w} \tilde{T}}{\partial t} + div\left(\bar{u}_f h_f c_{p,w} \tilde{T}\right) \right] = \left[c_{p,w} \tilde{T}_{d,\infty} + \dfrac{\left\| \vec{u}_d \right\|^2}{2} \right] \times U_\infty LWC\beta + \sigma\varepsilon\left(T_\infty^4 - T^4\right) & (4.11) \\ \qquad - \; 0.5\left(L_{evap} + L_{sub}\right) \dot{m}_{evap} + \left(L_{fus} - c_{p,ice}\tilde{T}\right) \dot{m}_{ice} + \dot{Q}_h & \\ h_f \geq 0 & \\ \dot{m}_{ice} \geq 0 & \\ h_f \tilde{T} \geq 0 & (4.12) \\ \dot{m}_{ice} \tilde{T} \leq 0 & \end{cases}$$

To investigate the well-posedness of ICE3D-SWIM, one should first see if the compatibility relations lower the number of unknowns from 3 to 2. Indeed, as could be seen in figure 4.4, the regions of the $\left(h_f, \tilde{T}, \dot{m}_{ice}\right)$ - icing space delimited by the compatibility relations generate a connected surface, called the icing surface. But two degrees of freedom are enough to describe a surface. It thus becomes clear that by restricting the solution of ICE3D-SWIM to the icing surface, the number of unknowns matches the number of PDEs available.

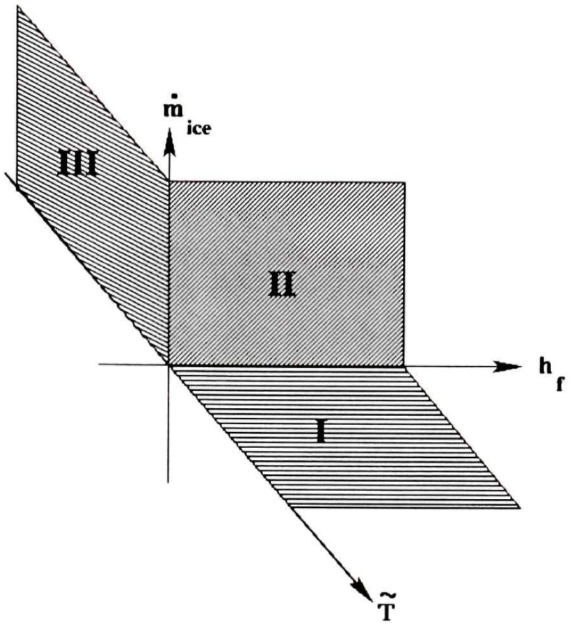

Figure 4.4: Surface generated by the compatibility relations: I, running wet, no ice; II, glaze icing; III, rime icing.

The icing surface is composed of three contiguous quarters of plane. The first one labeled I on figure 4.4, corresponds to a running wet-no ice growth condition above the freezing point: some water may impinge on the walls, but no freezing occurs. Regions II and III correspond to wet and dry ice growth conditions, respectively. For wet or glaze ice growth condition a water film and some ice are present simultaneously, and the equilibrium temperature should be the triple point of water. For dry or rime ice growth all the impinging water freezes: no water runs back and the temperature of the interface could be below the freezing point. Of course, the solution is not restricted in space and in time, and switching is done automatically by the solver.

4.1.6. Ice growth and nodes displacements

The ice accretion equations are solved to get the rate of mass accretion by surface area, $\dot{m}_{ice}\,(kg/m^2 s)$, for each node on the wall. This rate of mass accretion must be converted into a nodal displacement to modify the original grid and the original surface. To obtain the nodal displacement:

- A growth direction must be assumed, either normal to the wall or in the opposite direction of the impinging droplets;
- An ice thickness in this direction is obtained.

As much as possible, the ice thickness at each node must be selected as to ensure mass conservation for a given ice density. In other words, the ice thickness must take into account the deformation of the body surface. Inside the ice accretion module, the ice density can be chosen constant ($\rho_{ice} = 917\,kg/m^3$), or variable, according to the Macklin formula:

$$\rho_{ice} = 378 + 425\log_{10}(R_M) - 82.3(\log_{10}(R_M))^2 \text{ for } 0.2 < R_M < 170$$

$$\rho_{ice} = 917\,kg/m^3 \text{ for } R_M \le 0.2 \text{ or } R_M \ge 170$$

with $R_M = -\dfrac{r_d u_{d,n}}{\tilde{T}}$ with r_d the mean droplet radius in μm, $u_{d,n}$ the normal droplet velocity component and $\tilde{T}$ the wall temperature in Celsius. The variable density approach has been chosen to perform the test cases presented in this thesis.

For a given time interval Δt the volume of ice accreted is given by:

$$V_{ice} = \int_0^{\Delta t} \int_S \frac{\dot{m}_{ice}}{\rho_{ice}} ds dt \tag{4.13}$$

The rate of mass accretion by surface area, the ice density and the area S change with time and position along the iced surface. The discrete form of equation (4.13) is:

$$V_{ice} = \sum_{t=0}^{\Delta t} \sum_{i=1}^{n_s} \frac{\dot{m}_{ice}}{\rho_{ice}} ds_i(t)$$

where n_s is the number of nodes on the wall body geometry.

If a tight coupling between the airflow, droplet and ice accretion solver is used, the surface $ds(t)$ can be considered constant in time. Therefore the ice thickness can be defined by:

$$D_{ice} = \frac{\dot{m}_{ice}}{\rho_{ice}} \tag{4.14}$$

and

$$V_{ice} = \sum_{i=1}^{n_s} ds_i \sum_{t=0}^{\Delta t} D_{ice} \tag{4.15}$$

If large nodal displacements occur, the area displacements change in time. The ice thickness must then take into account the surface deformation.

$$V_{ice} = \sum_{t=o}^{\Delta t} \sum_{i=1}^{n_s} D_{ice} distds_i \tag{4.16}$$

where $distds_i$ is the area associated at each node at time t. Volumes from equations (4.15) and (4.16) are not equal, unless a corrected value for the ice thickness D_{ice} is used. The rate of ice accretion must be applied on the new displaced surface. The ice thickness at each node becomes:

$$D_{ice} = \frac{\dot{m}_{ice}\, ds_i / distdsi}{\rho_{ice}} \tag{4.17}$$

where ds_i is the area associated at each node at initial time.

A sketch of different possible deformations, with the corresponding corrected ice thickness h, is drawn in figure 4.5.

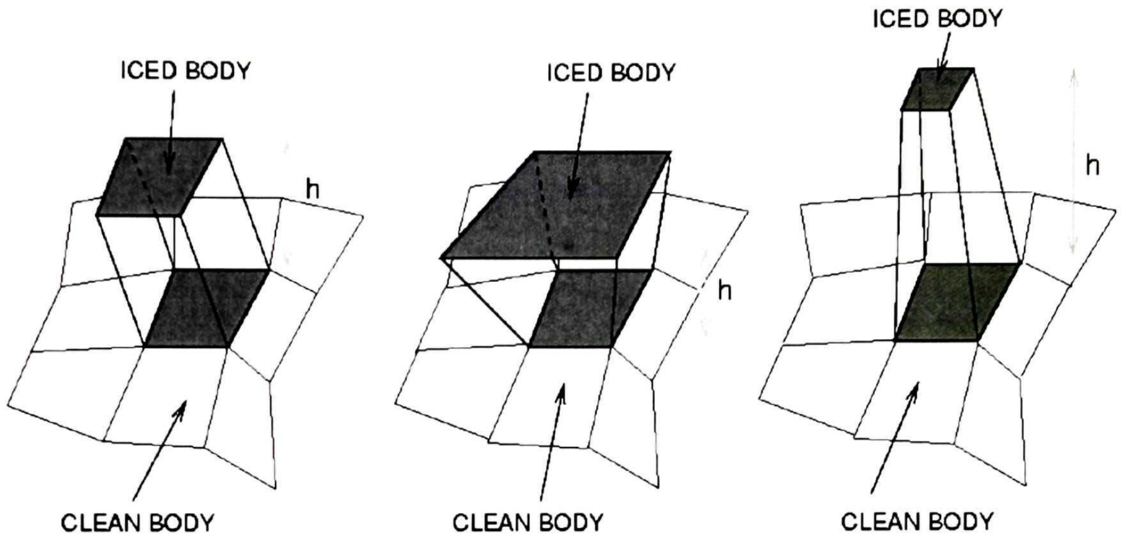

Figure 4.5: Computation of the ice thickness according to the wall body surface deformation.

An example of nodes displacements respecting the mass of ice accreted on an existing test case is shown in figure 4.6. In this figure, the resulting ice shape, when nodes displacements are computed taking into account the wall body surface deformation (equation 4.17), is compared to the resulting ice shape when equation (4.14) is used to compute the nodes' displacements as if no deformation occurs. As can be seen, the correction effect is more visible on the horn.

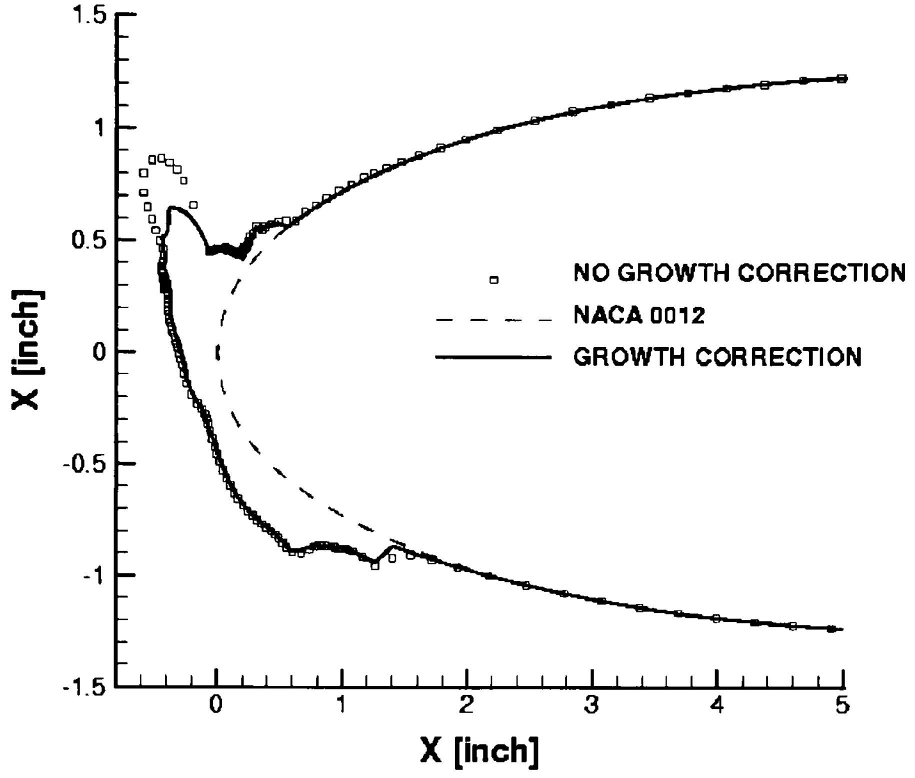

Figure 4.6: Comparison between mass conservative ice growth and non mass conservative ice growth on Run 308 (Ref. 66).

4.2. Computational approach

4.2.1. Finite volume method

4.2.1.1. Choice of the control volumes

Special care has to be taken because the two PDEs are expressed on the walls of the geometry, i.e. on a two-dimensional surface embedded in a three-dimensional one. So, the first derivatives, more precisely the *div* operator, of some unknowns, have to be evaluated along the wall surface. A classical way to compute the divergence of a vector on a surface is through the introduction of a curvilinear coordinate system on the surface.

To avoid the introduction of such curvilinear coordinates of an evolving (caused by ice growth) wall surface, the intrinsic definition of the *div* operator is applied:

$$div\vec{u}(P) = \lim_{v \to P} \frac{\int_{\partial v} \vec{u} \cdot \vec{n} ds}{vol(v)}, \qquad (4.18)$$

where v is an area element that shrinks to the point P on the surface.

The finite volume method is an application of that definition but at the discrete level. A finite volume cell is chosen as the area element v in equation (4.18) instead of a vanishing sequence of arbitrary area elements. Therefore a finite volume method is found more appropriate to discretize the partial differential equations. Here a finite volume cell means a cell of the dual surface mesh, figure 4.7. The boundary of the three-dimensional mesh at the air/structure walls interface is denoted as the surface mesh. From the surface mesh a dual mesh is obtained by connecting to cell centroids the mid-edges of the cells so that ICE3D-SWIM unknowns correspond one to one to the finite element nodes of the airflow and droplet solutions. The discrete equations are obtained upon application of the finite volume method on this dual mesh; the solution obtained is an average value over the cell and is set at the mesh nodes.

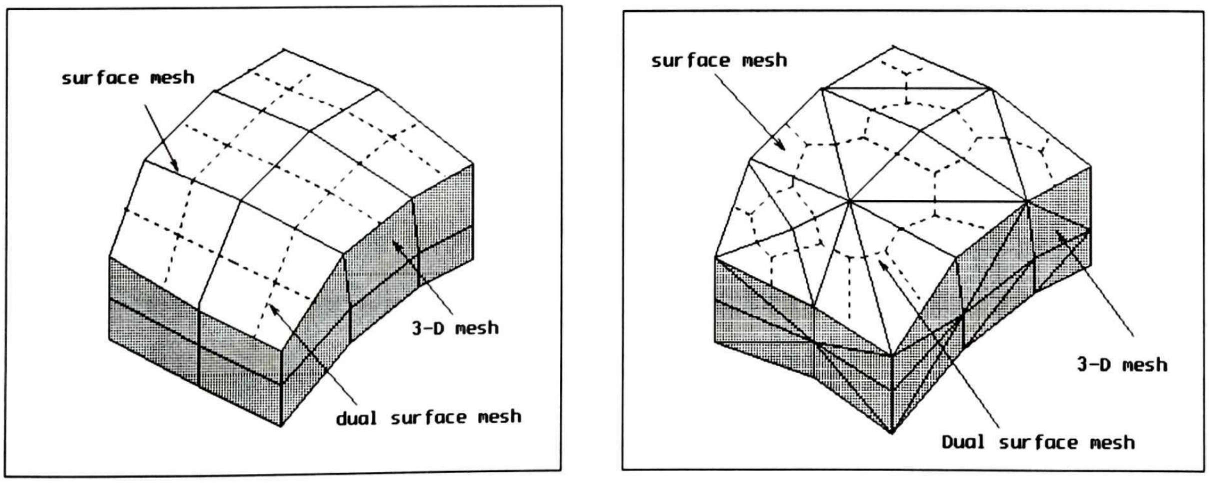

Figure 4.7: Dual meshes on structured and unstructured grids.

The nodes on the surface have a global numbering coming from the 3D finite element mesh, and a numbering associated to the skin mesh. Because our finite volume method is expressed in 3D, pointers are used to go from one numbering to the other.

4.2.1.2. Spatial discretization

We recall that:

$$\bar{u}_f = \frac{h_f}{2\mu_w}\bar{\tau}_{wall}\left(\bar{x}, y\right)$$

Another way to formulate our mass and energy conservation equations is the following:

$$\begin{cases} \dfrac{\partial h_f}{\partial t} + \vec{\nabla}\cdot\left(\vec{\tau}_{wall}\dfrac{h_f^2}{2\mu_w}\right) = \dfrac{S^h}{\rho_w} \\ \dfrac{\partial\left(c_{p,w}h_f\tilde{T}\right)}{\partial t} + \vec{\nabla}\cdot\left(c_{p,w}\vec{\tau}_{wall}\dfrac{h_f^2\tilde{T}}{2\mu_w}\right) = \dfrac{S^{\tilde{T}}}{\rho_w} \end{cases} \tag{4.19}$$

where S^h is the source term corresponding to the mass balance equation, and $S^{\tilde{T}}$ is the source term corresponding to the energy equation. We consider that $c_{p,w}$ is constant through the domain of computation. Let us define:

$$U = \begin{bmatrix} h_f \\ h_f\tilde{T} \end{bmatrix} \quad \vec{F}(U) = \begin{bmatrix} \dfrac{h_f^2}{2\mu_w}\vec{\tau}_{wall} \\ \dfrac{h_f^2\tilde{T}}{2\mu_w}\vec{\tau}_{wall} \end{bmatrix} \quad S = \begin{bmatrix} \dfrac{S^h}{\rho_w} \\ \dfrac{S^{\tilde{T}}}{c_{p,w}\rho_w} \end{bmatrix}$$

The conservative form of our system is the following:

$$\frac{\partial U}{\partial t} + \vec{\nabla}\cdot\vec{F}(U) = S$$

4.2.1.3. A Roe scheme

The Roe scheme is a first-order Godunov[60, 61, 62] scheme. It is a conservative extension of the first-order upwind scheme to non-linear systems of hyperbolic conservation laws. The essential ingredient of the Godunov method is the solution of the Riemann problem, which may be the exact solution or some suitable approximation to it.

Let U_i and U_j be the vector of unknowns at points i and j, the Roe scheme is expressed in the following manner:

$$vol(C_i)\frac{\partial U_i}{\partial t}+\sum_{j\ neighbor\ of\ i}\int_{\partial C_{ij}}\Phi^{Roe}(U_i,U_j,\vec{n})\,ds=vol(C_i)S_i \tag{4.20}$$

with

$$\Phi^{Roe}(U_i,U_j,\vec{n})=\frac{1}{2}\left(\vec{F}(U_i)+\vec{F}(U_j)\right)\cdot\vec{n}-\frac{1}{2}\left|\vec{J}(U_{i+1/2})\cdot\vec{n}\right|\left(U_j-U_i\right) \tag{4.21}$$

where $\vec{J}\left(U_{i+1/2}\right)$ is the Jacobian matrix defined at the mid-point by: $\vec{J}\left(U_{i+1/2}\right)=\vec{J}_{i+1/2}=\vec{J}\left(\frac{U_i+U_j}{2}\right)$.

The definition of the Jacobian matrix of our system is given by equation (4.22).

$$\vec{J}\left(U_{i+1/2}\right)\cdot\vec{n}=\begin{bmatrix}\frac{h_f}{\mu_w}\left(\vec{\tau}_{wall}\cdot\vec{n}\right) & 0\\ \frac{h_f\tilde{T}}{2\mu_w}\left(\vec{\tau}_{wall}\cdot\vec{n}\right) & \frac{h_f}{2\mu_w}\left(\vec{\tau}_{wall}\cdot\vec{n}\right)\end{bmatrix} \tag{4.22}$$

We define by h_i the value of h_f at node i and by $\tilde{T}_i$ the value of $\tilde{T}$ at node i. By substitution inside the definition of Φ^{Roe} we obtain:

$$\Phi^{Roe}(U_i,U_j,\vec{n}) = \begin{bmatrix} \frac{1}{2}\left(h_i^2 + h_j^2 \right)\vec{u}\cdot\vec{n} \\ \frac{1}{2}\left(h_i^2\tilde{T}_i + h_j^2\tilde{T}_j \right)\vec{u}\cdot\vec{n} \end{bmatrix} - \left|\vec{u}\cdot\vec{n}\right| \begin{bmatrix} (h_j - h_i)h_{ij} \\ \frac{\left(h_i\tilde{T}_i + h_j\tilde{T}_j\right)}{2}\frac{(h_j - h_i)}{2} + \frac{h_{ij}}{2}\left(h_j\tilde{T}_j - h_i\tilde{T}_i \right) \end{bmatrix} \tag{4.23}$$

with

$$\vec{u} = \frac{\vec{\tau}_{wall}}{2\mu_w} \qquad\qquad h_{ij} = \frac{1}{2}(h_i + h_j)$$

At node i we have to solve:

$$vol(C_i)\left(\rho_w \frac{\partial h_i}{\partial t} - S_i^h \right) + \sum_{j \text{ neighbor of } i} R_{ij}^h = 0 \tag{4.24}$$

$$vol(C_i)\left(\rho_w \frac{\partial c_w h_i \tilde{T}_i}{\partial t} - S_i^{\tilde{T}} \right) + \sum_{j \text{ neighbor of } i} R_{ij}^{\tilde{T}} = 0. \tag{4.25}$$

The summation is taken over all of the nodes j connected to the node i with R_{ij}^h and $R_{ij}^{\tilde{T}}$ defined by:

$$R_{ij}^h = \frac{1}{2}\rho_w\left[h_i^2 + h_j^2 \right]\vec{u}_{ij}\cdot\vec{n}_{ij} - \rho_w\left|\vec{u}_{ij}\cdot\vec{n}_{ij}\right| h_{ij}\left[h_j - h_i \right]$$

$$R_{ij}^{\tilde{T}} = \frac{c_{p,w}}{2}\rho_w\left[h_i^2\tilde{T}_i + h_j^2\tilde{T}_j \right]\vec{u}_{ij}\cdot\vec{n}_{ij} - \rho_w\left|\vec{u}_{ij}\cdot\vec{n}_{ij}\right|\frac{c_{p,w}}{2}\left[\frac{\left(h_i\tilde{T}_i + h_j\tilde{T}_j\right)}{2}\left(h_j - h_i \right) + h_{ij}\left(h_j\tilde{T}_j - h_i\tilde{T}_i \right) \right]$$

4.2.2. Time discretization

The time derivatives could be discretized with any finite difference formula. An implicit scheme was first implemented followed by an explicit scheme. The details of each method are briefly discussed in the following sections.

4.2.2.1. Implicit scheme

Inside the implicit scheme the variables h_i and $h_i\tilde{T}_i$ are only needed to write down the Roe scheme. Indeed, their use as dependent variables is not recommended for the present system as the film thickness, h_i, may vanish in many icing situations, and $h_i\tilde{T}_i$ would also vanish, preventing the recovery of $\tilde{T}_i$ from $h_i\tilde{T}_i$ as when h_i is strictly positive. The variables h_i and $\tilde{T}_i$ seem a better choice. Even if h_i vanishes at some grid points, the use of a fully implicit scheme will make possible the recovery of $\tilde{T}_i$ from the degenerated equations $S_i^h = 0$ and $S_i^{\tilde{T}} = 0$.

The instantaneous ice accretion rate $\dot{m}_{ice}$, is also a dependent variable, although appearing only in the source terms. At each node, i, three unknowns h_i, $\tilde{T}_i$ and $\dot{m}_i$ are thus to be computed, satisfying the system (4.24) and (4.25) and the compatibility relations. These could be addressed later in their original form (4.12). Unfortunately, standard iterative methods like the Newton method cannot handle directly such a system of two equations and four inequalities. Even the application of nonlinear programming techniques[63] to the original problem is tedious and expensive as four generalized Lagrange multipliers would have to be added at each node to cope with the four inequalities.

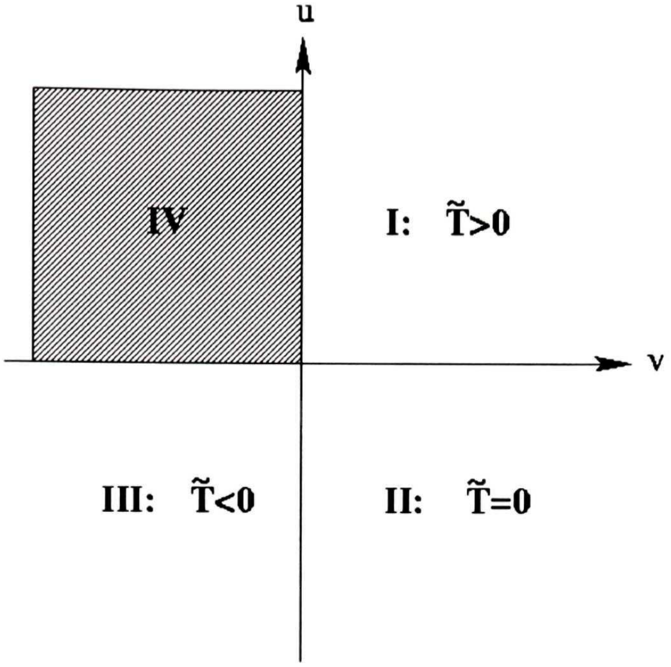

Figure 4.8: Icing plane: I, running wet, no ice; II, glaze icing; III, rime icing; IV, dry air, no man's land.

Instead, we introduce a change of variable from a portion of the plane onto the icing surface. Figure 4.8 shows that portion of the plane, called the icing plane, with regions labeled I to III as for the icing surface in figure 4.4. An extra region, labeled IV, has appeared, which corresponds to dry air flight situations, i.e. without any droplets for an arbitrary temperature below or above the freezing point.

The significance of each region is better understood by looking at the change of variable from the icing plane (u,v) to the icing surface:

Region I $\begin{cases} \tilde{T} = v^2 \\ h_f = u^2 \\ \dot{m}_{ice} = 0 \end{cases}$ Region II $\begin{cases} \tilde{T} = 0 \\ h_f = u^2 \\ \dot{m}_{ice} = v^2 \end{cases}$

Region III $\begin{cases} \tilde{T} = -u^2 \\ h_f = 0 \\ \dot{m}_{ice} = v^2 \end{cases}$ Region IV $\begin{cases} \tilde{T} = v^2 - u^2 \\ h_f = 0 \\ \dot{m}_{ice} = 0 \end{cases}$

This change of variable is invertible from the icing surface onto the region $I \cup II \cup III$ of the icing plane. Moreover the transformation is differentiable, even on the u and v axis. These two features allow the solution of ICE3D-SWIM in (u_i, v_i) instead of $(\tilde{T}_i, h_i, \dot{m}_i)$ at each node. For example, using Newton's method, the two unknowns (u_i, v_i) are updated with the residual of the two equations (4.24) and (4.25), without compromising the convergence of the iterative solver because the transformation is sufficiently regular. Whatever (u_i, v_i) is selected in the icing plane, the compatibility relations will be automatically satisfied.

Whenever required, the inverse transformation could be used to recover the physical variables $(\tilde{T}_i, h_i, \dot{m}_i)$ from (u_i, v_i). A difficulty arises from the fact that the inverse transformation is not defined in region IV, and the iterative solver could very well converge to values in that region. As just stated, region IV corresponds to dry air situations, which are, in fact, already completely represented by the points on the portion of the u and v axis adjacent to this region. Region IV simply has to be avoided, otherwise the system (4.24) and (4.25) would be indefinite. Nonlinear programming techniques could be used to avoid going out of regions I, II and III.

4.2.2.2. Explicit scheme

In practice, nonlinear programming techniques[64, 65] are not so easy to use, especially if we deal with general inequality constraints. Inequality constraints can be expressed as equations with help of Lagrange multipliers but each constraint will add an unknown to our problem.

If we come back to our physical problem; three water phase changes are possible: from liquid to solid, solid to liquid or solid-liquid to gas, depending on the thermodynamic transfer of energy inside the control cell. These changes of phase create fronts that are difficult to track with a numerical scheme. Another convenient way to deal with this difficulty is to use an explicit scheme with small time steps to prevent instabilities.

The phase changes can be treated as moving boundary conditions from one phase to another. Because physical phase may vanish or appear, special care must be taken to conserve mass transfer and heat transfer fluxes.

For a simplification purpose we will express the instantaneous mass of ice accretion using the following formula:

$$\dot{m}_i = \frac{\partial m_i}{\partial t}.$$

Therefore the system (4.24) and (4.25) will be expressed by equations (4.26) and (4.27):

$$vol(C_i)\left(\rho_w \frac{\partial h_i}{\partial t} + \frac{\partial m_i}{\partial t} - S_1\right) + \sum_{j \text{ neighbor of } i} R_{ij}^h = 0 \tag{4.26}$$

$$vol(C_i)\left(\rho_w \frac{\partial c_w h_i \tilde{T}_i}{\partial t} - (L_{fus} - c_{p,ice}\tilde{T}_i)\frac{\partial m_i}{\partial t} - S_2\right) + \sum_{j \text{ neighbor of } i} R_{ij}^{\tilde{T}} = 0 \tag{4.27}$$

where S_1 corresponds to S_i^h without the term containing $\dot{m}_i$ and S_2 corresponds to $S_i^{\tilde{T}}$ without the term containing $\dot{m}_i$. The algorithm used to solve the problem is shown in figure 4.9. Regions I, II, and III correspond to those of figure 4.8, i.e. I: running wet, no ice; II: glaze ice and III: rime ice. At node i, the temperature of the preceding time step,

$n-1$, is used to determine the first guess region. If the compatibility relations are satisfied, node i remains in that region at time n, otherwise a different region is selected until the compatibility relations are satisfied. A water phase change occurs at node i if the node switches from one region to another one between time $n-1$ and n.

4.3. Conclusions

A new equilibrium ice accretion model based on two PDEs has been developed to predict ice shapes on impacted surfaces using the shear stress and the convective heat fluxes from the airflow solver and the local collection efficiency from the droplets solver. This model includes some features for continuous film runback prediction on two- and three-dimensional geometries and compatibility relations to ensure a physical solution and the well-posedness of the problem. By using a PDE-based model, a distinction can be made between the physical modeling and the numerical resolution of the resulting problem. A numerical scheme using the finite volume method and based on a Roe scheme is derived to solve the problem. In practice all the results of the following chapters have been obtained using the explicit scheme.

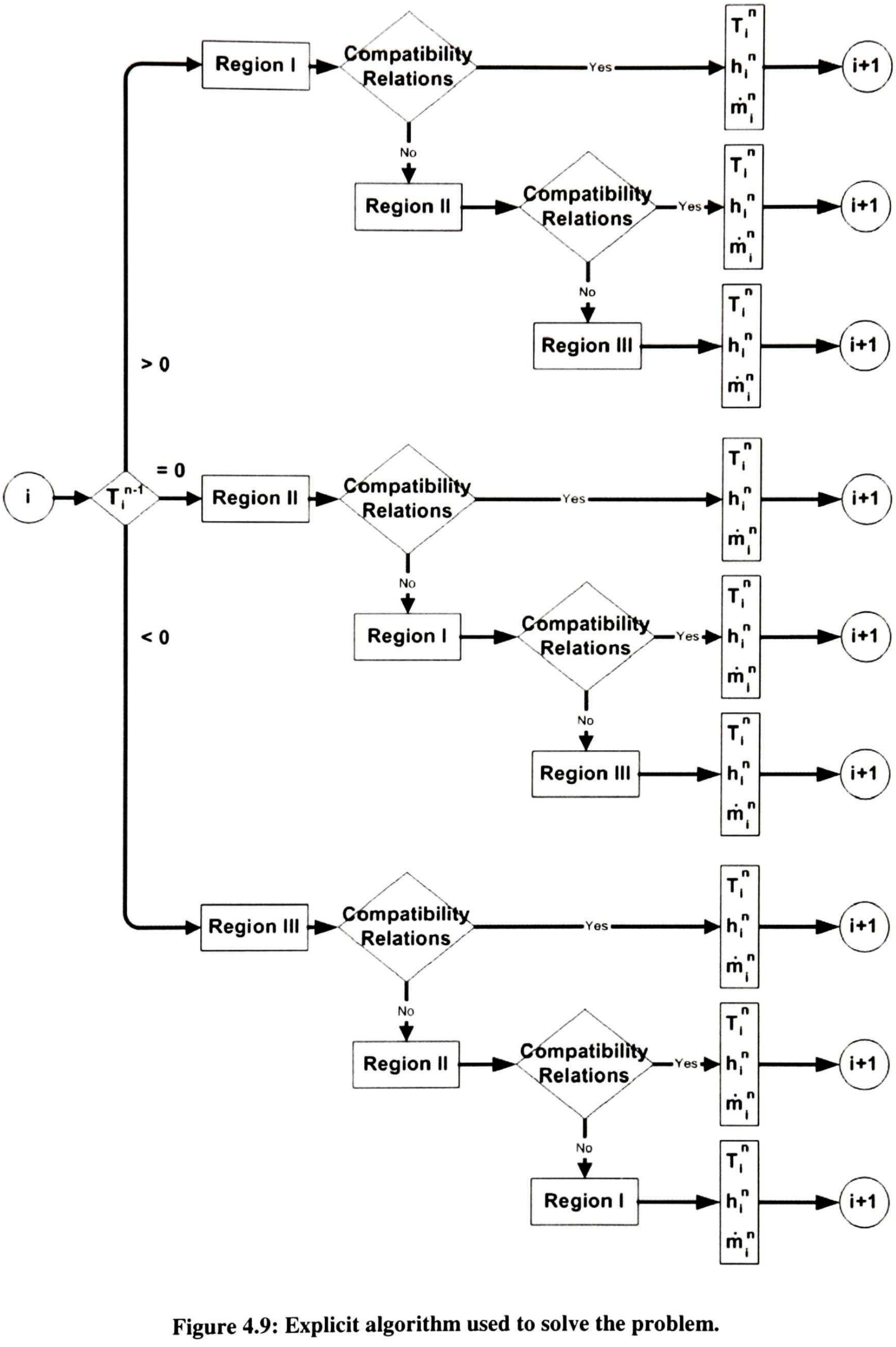

Figure 4.9: Explicit algorithm used to solve the problem.

Chapter 5

Two-dimensional Validations

ICE3D-SWIM has been compared to numerical solutions obtained with LEWICE, and experimental results done in the NASA Glenn (formerly NASA Lewis) Icing Research Tunnel (IRT)[66]. All 2D calculations are carried out in a pseudo-3D manner on meshes of one element thickness in the spanwise direction. A consensus[67, 68] about the comparison of two icing shapes is difficult to obtain in icing. Indeed the focus can be on different criteria such as the limit of impact, the ice thickness or the location and angle of a possible horn, etc. As a consequence, the comparisons remain most of the time subjective but conservative enough to meet best aircraft safety.

In December 2000, all icing computer code developers, FIA representatives, aircraft industries including Boeing participants met at Capua (CIRA) in Italy in the context of a NATO/RTO Symposium[68] to validate their results by comparing numerical ice shapes to wind tunnel experiments in rime ice and glaze ice conditions on: airfoils, multi-element configurations, nacelles and rotary wings. This event has been unique and gave the opportunity to the international aircraft icing community to give their results of this exercise one year in advance of the workshop. The final discussion reveals that there is still a large discrepancy between the numerical simulations and icing wind tunnels data, especially for glaze ice conditions and it is almost the same between flight test results and laboratories experiments. The consistency of ice shapes produced in icing wind tunnels needs to be investigated. Development of a reliable method to quantitatively judge similarity between ice shapes is needed. The method should consider the similarity between the aerodynamic effects of the ice shapes as well as the geometric similarities. In addition, discovering that various codes give various shapes will not shed light on what is the culprit. Ice accretion needs an airflow solution, an impingement model and an ice accretion model. If the first two do not agree (different solvers, mesh density, no specified convergence criteria, etc.), it is impossible to state why there is a difference in ice shapes.

Experimental methods in icing

Given the inherent variability[69] in the shape of experimental ice accretions, when comparing the goodness of ice accretions formed, it is typical to use words like poor, fair, good or excellent. How good can the comparisons be, given the inherent variability of ice shapes obtained from identical icing conditions? To answer this question it is necessary to have access to a fair estimation of the experimental error, for each icing condition run. In the IRT[70], for example, the data is taken by cutting out a small section of the ice growth and tracing the contour of the ice shape onto a cardboard template with a pencil. During such experiments there are several steps which can potentially cause experimental error:

- Spanwise variability:

Even with a two-dimensional wing model, the ice shape produced in the tunnel will have some spanwise variability due to the random nature of ice accretion process.

- Uncertainty in setting conditions:

Several tests assessed experimental error[70] by running the same flow and spray conditions for the same airfoil multiple times. The repeatability of the ice shape also raises the question of uncertainty in setting conditions in the icing tunnel, like for example controlling a constant LWC during the experiment.

- Tracing technique:

There are several potential errors involved in the ice tracing and digitization process which are difficult to quantify. Some of these errors come from the quality of the template, the technique used to trace the ice shape and by the digitization process. If the ice shape extends beyond the dimensions of the template, it cannot be traced. The technique used may also have an effect on the final digitized ice shape. The template may not be placed squarely on the airfoil, the person may only trace the top of ice feathers or not trace feathers at all, as the ice feather may break off due to the pressure applied by the pencil. The researcher may not always trace a single continuous line for the ice shape, making the digitalization process more difficult. Multiple tracings of the same ice shape are rarely performed in the IRT[70] and even more rarely are more than one tracing digitized.

5.1. Mesh density effects

The effect, on the ice accretion simulation, of mesh density around the leading edge of a NACA 0012 airfoil has been studied with a coarse (90 nodes on the airfoil), medium (180 nodes) and fine grid (360 nodes), figures 5.1 to 5.3. The meshes contain, respectively, 23350, 36130 and 61690 nodes. The spacing in the direction normal to the wall is kept the same for the 3 meshes and is equal to $8.4\times10^{-6}c$, c being the chord of the airfoil. The ambient conditions selected for this test case correspond to the LEWICE run 403[66] and are given in table 5.1. The accretion time is 7 minutes. The airflow, impingement and ice accretion solutions on the 3 meshes are compared to each other and compared to LEWICE solutions[66]. For the airflow and impingement solutions the results are plotted against the distance from the stagnation point.

Parameter	Value
T_∞	262.04K
P_∞	100 kPa
U_∞	102.8 m.s^{-1}
AOA	4^{o}
MVD	20μm
LWC	0.55g/m^3
Re_∞	4.39×10^6

Table 5.1: Ambient conditions corresponding to Run 403.

5.1.1. Airflow solution

The turbulence model selected for the simulation is the one-equation Spalart-Allmaras model with an equivalent sandgrain roughness of 0.55 mm. The convective heat transfer coefficient on the airfoil geometry is compared for the three turbulent airflow solutions in figure 5.4. The curve shapes are the same for the three solutions, only the amplitude varies. The solutions on the medium and fine grids are similar and appear to be mesh independent.

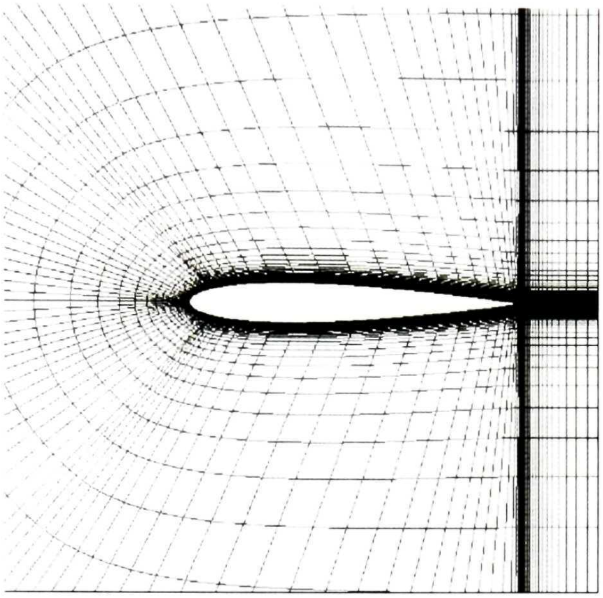

Figure 5.1: NACA 0012 airfoil, coarse mesh.

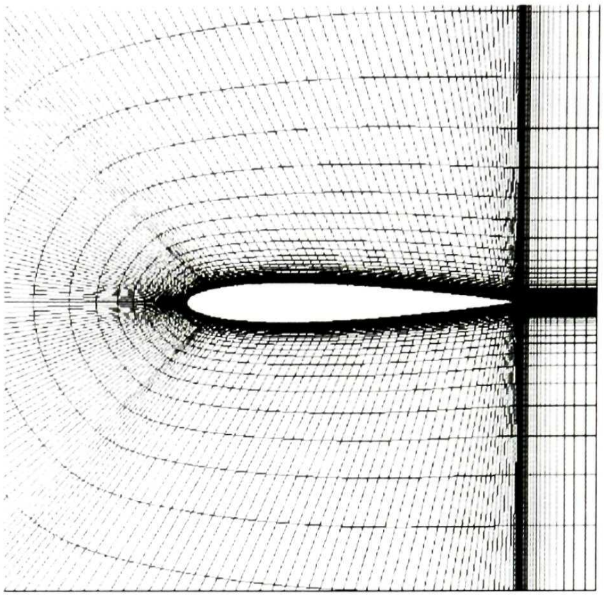

Figure 5.2: NACA 0012 airfoil, medium mesh.

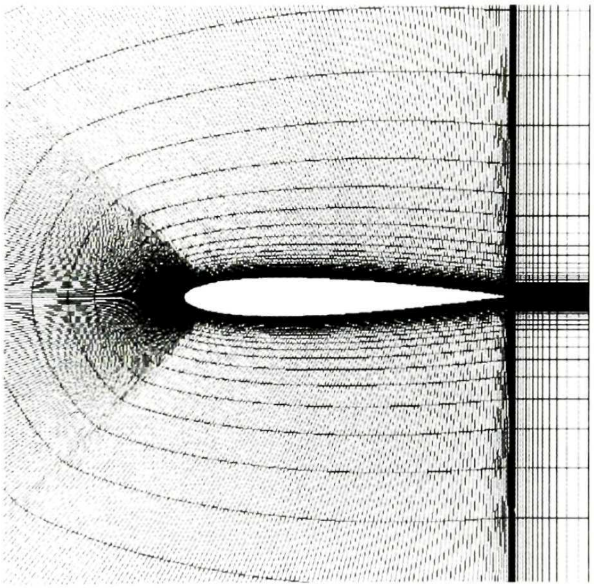

Figure 5.3: NACA 0012 airfoil, fine mesh.

LEWICE uses an integral method to solve the boundary layer. LEWICE and FENSAP solutions are compared in figure 5.5. The differences between the two curves close to the trailing edge are due to the thickness of the boundary layer which is not taken into account by the LEWICE code. Close to transition points the differences are most probably induced by the roughness coefficient. The equivalent sandgrain roughness coefficient used for this calculation is the same as LEWICE. This roughness coefficient is especially calibrated for LEWICE (Chapter 3, last section, equation 3.7). Although the two methods employed are strongly different, the two solutions agree pretty much and the results are satisfactory.

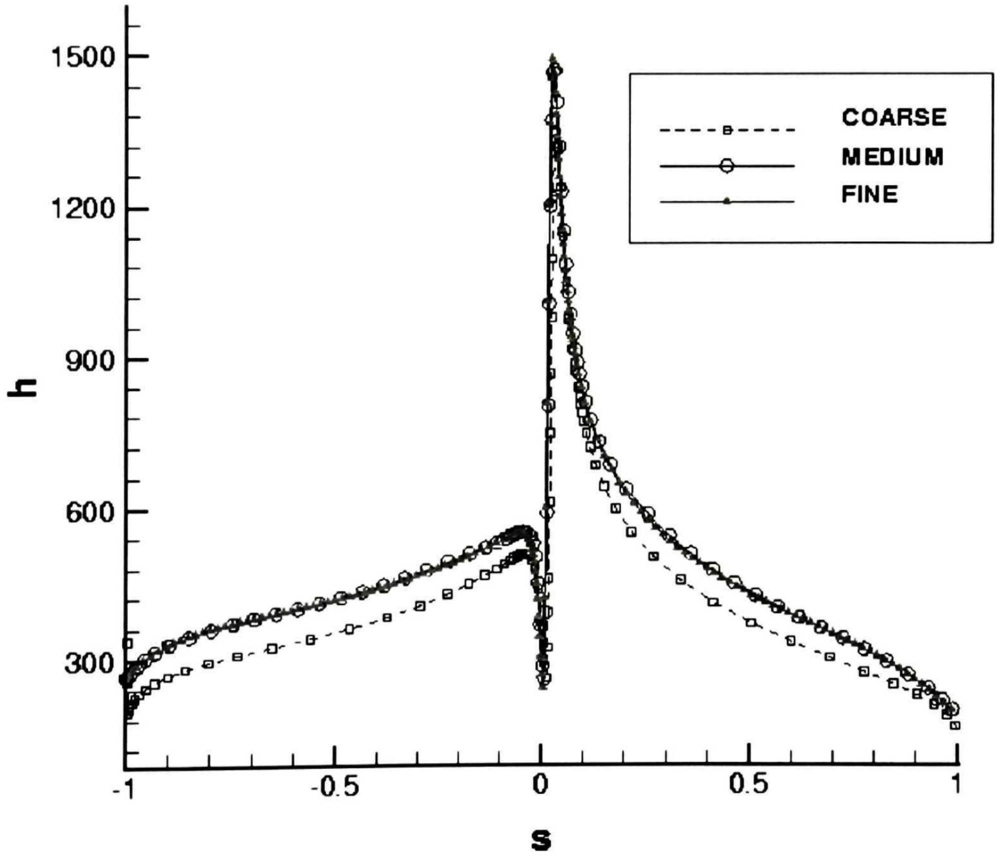

Figure 5.4: Convective heat transfer coefficient (W/m^2K) distribution against the distance from stagnation point for the coarse, medium and fine grids.

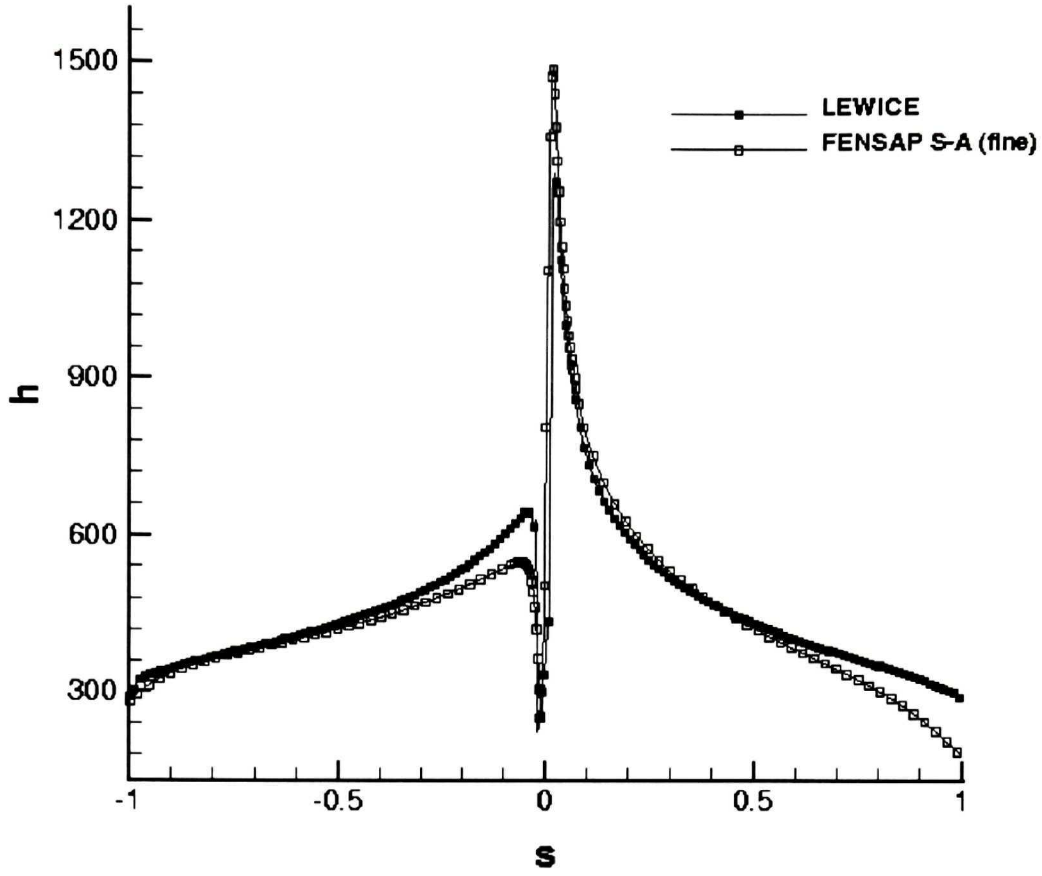

Figure 5.5: Convective heat transfer coefficient (W/m^{2}K) distribution against the distance from stagnation point, comparison between FENSAP S-A (fine grid) and LEWICE solution.

5.1.2. Impingement solution

The local collection efficiency, for the 3 meshes, is compared in figure 5.6. The solutions are identical for the 3 meshes.

The comparison with LEWICE is shown in figure 5.7. The maximum collection efficiency predicted by the two codes is identical. The impingement limits are slightly different on the upper part of the airfoil ($s \geq 0$). This is most probably due to a loss of precision from LEWICE, which uses panel methods for flow calculations.

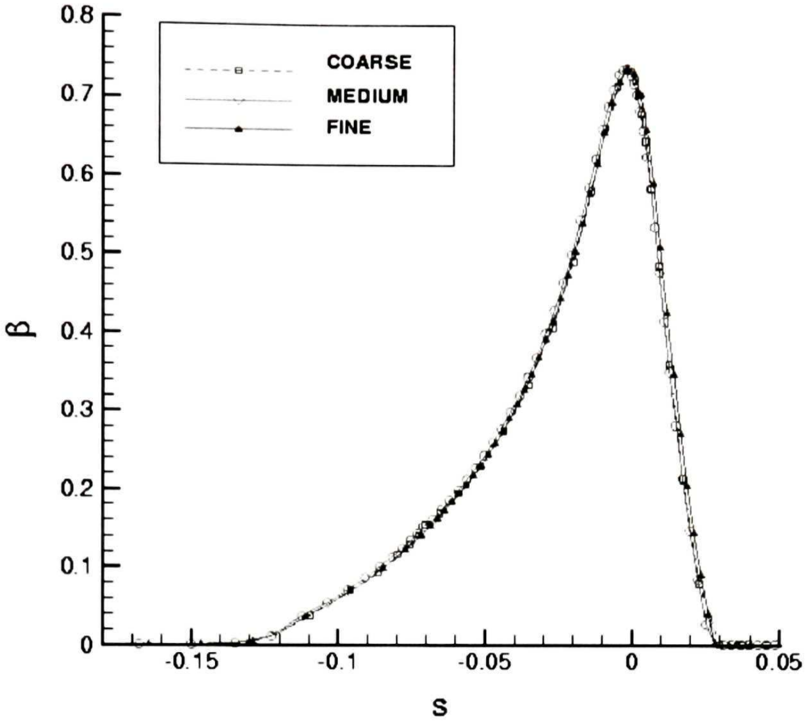

Figure 5.6: Local collection efficiency distribution against the distance from stagnation point for the coarse, medium and fine grids.

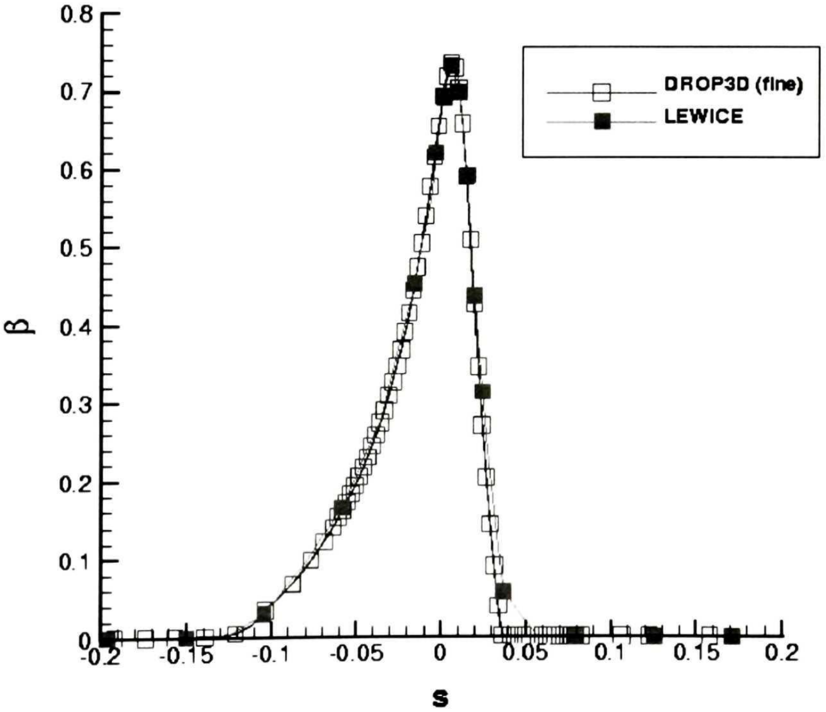

Figure 5.7: Local collection efficiency distribution against the distance from stagnation point, comparison between DROP3D (fine grid) and LEWICE.

5.1.3. Ice accretion solution

For the ice accretion module, a one-shot ice accretion simulation is performed on each mesh. The aim is to have bigger ice shapes to compare, and also to not mix the effect of mesh density with the effect of airflow solution updates on the solution. This last aspect will be studied in isolation in the next section.

The comparison of ice shapes on the three meshes is shown on figure 5.8. The mass of ice accreted is the same for the three meshes and is equal to 0.496 kg per unit span. The three ice shapes are similar, with only some details like the ice thickness close to the stagnation point and close to the impingement limits varying for the coarse grid compared with the fine and medium grids. It is also possible to miss some details on the ice shape with the coarse grid, as can be seen on the pressure side of the airfoil.

For this run number, two experimental solutions are available. The LEWICE numerical solutions obtained with a multi-stepping approach composed of 7 layers is also available and shown in figure 5.9. The one-shot ICE3D-SWIM shape is acceptable compared to the experimental and numerical solutions, especially if we take into account the fact that the over predicted ice thickness on top of the airfoil will substantially decrease if a multi-stepping approach were used (see figures 5.10, 5.11 and 5.12). Indeed this part of the airfoil will be in the shadow zone of the bump located between the coordinates: $0 \leq Y \leq 0.2\ in.$

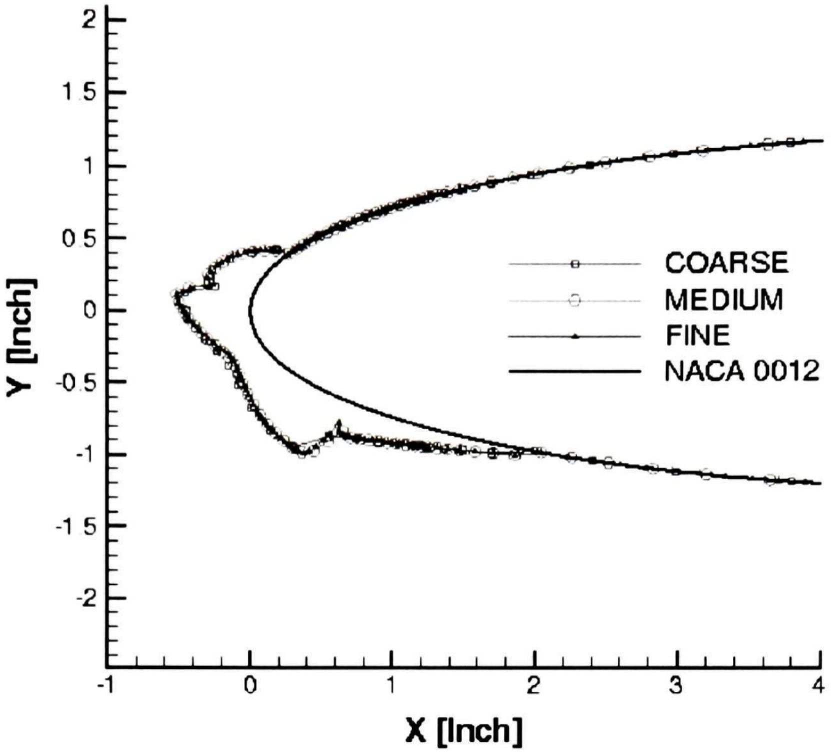

Figure 5.8: Run 403, comparison of the ice shape obtained with the coarse, medium and fine grids.

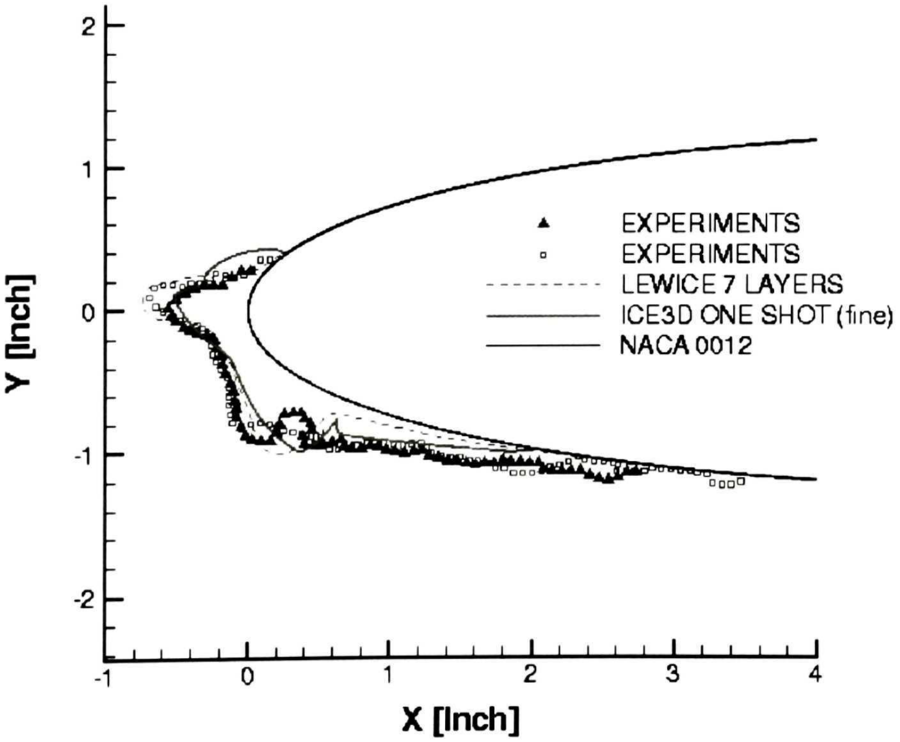

Figure 5.9: Run 403 [NASA-CDROM], ice shape comparison between ICE3D-SWIM (fine grid), LEWICE and experiments.

5.2. Effects of airflow solution updates on ice shapes

When multiple layers of ice are grown with an update of the airflow and impingement solution after each layer, more features can be seen on the ice shape (figure 5.10). If one part of the airfoil is in a shadow zone due to the ice growth, a one-shot ice accretion will over estimate the ice thickness in that region. For example in figure 5.11, we can notice that the one-shot ice accretion predicts a bigger ice thickness on the upper part of the airfoil. It is then usual that a one shot ice accretion predicts a bigger ice thickness close to the impingement limits (figures 5.10, 5.11 and 5.12). For glaze ice accretion, if a horn develops, a one-shot ice accretion will predict a shorter and larger horn than a multi-stepping approach. It is also possible to predict impact behind a horn due to the air recirculation (figure 5.12).

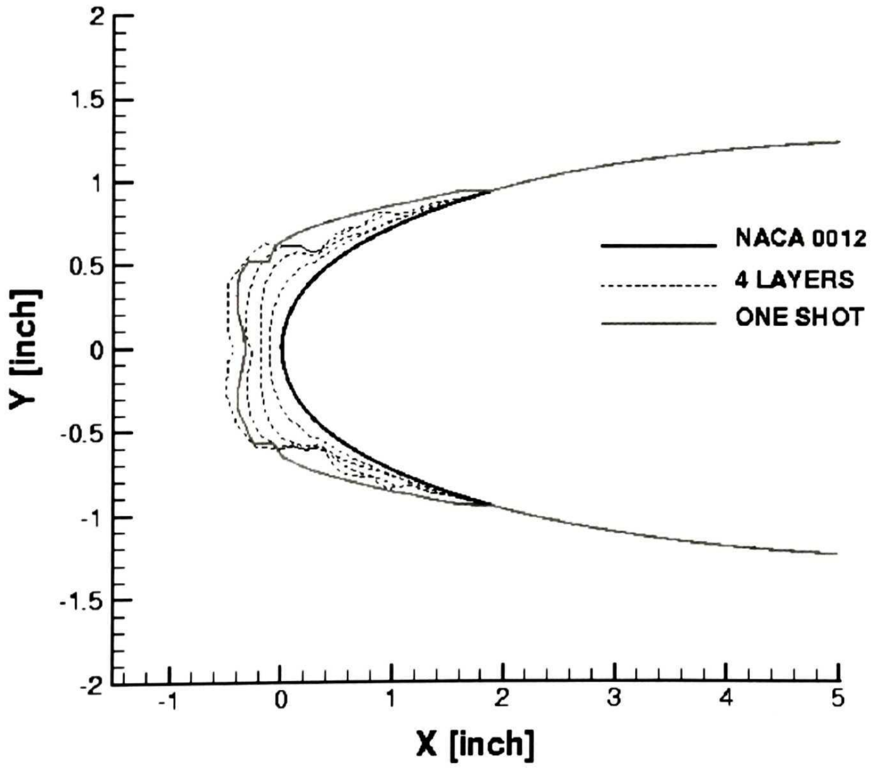

Figure 5.10: Effects of multiple layers on ice shapes, NACA0012 at 0° AoA.

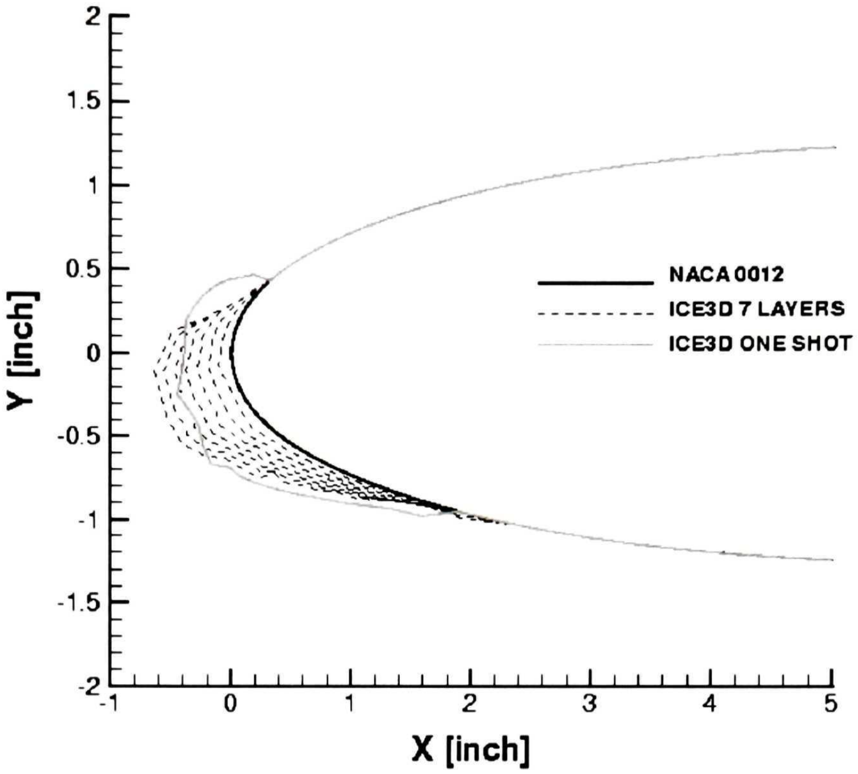

Figure 5.11: Effects of multiple layers on ice shapes, NACA0012 at 4° AoA.

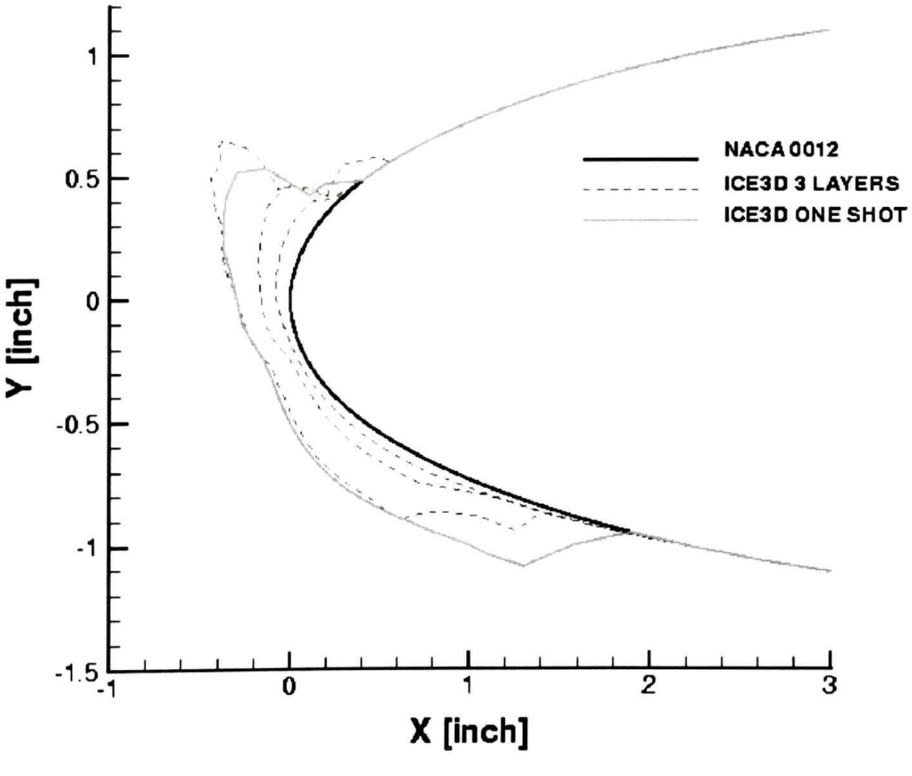

Figure 5.12: Effects of multiple layers on ice shapes, glaze ice conditions with a horn.

5.3. Validation on symmetrical airfoil: NACA 0012

The NACA 0012 airfoil, figure 5.13, has been used in several test entries. The data from this airfoil represent the highest number of ice shapes which have been created in the IRT. Through all this section, the ice shapes are plotted in inches.

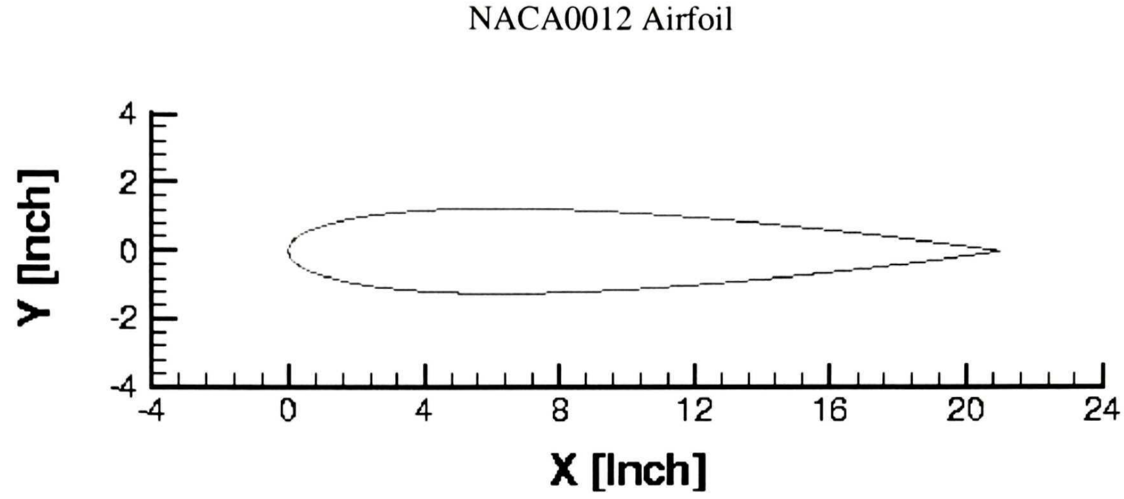
NACA0012 Airfoil

Figure 5.13: NACA0012 Airfoil.

5.3.1. Run 404

In the first comparison, ice is accreted for 7 minutes on a NACA 0012 airfoil at an AoA of 4°. The ambient icing conditions, which should be close to rime ice accretion are given in table 5.2 and correspond to LEWICE Run 404[66].

The first five minutes of accretion are calculated in five 1-min time steps and compared to the LEWICE solution in figure 5.14. The first minute of ice accretion is almost identical for ICE3D-SWIM and LEWICE. The limits of impact are the same and the ice thickness coincides almost everywhere. The location and angle of the upper bumps match in the two numerical solutions. One can notice that ICE3D-SWIM slightly over predicts the ice thickness on the top bump and just below the stagnation point. This can be explained by a larger amount of runback predicted by LEWICE. Naturally, the differences magnify after each update of the airflow and droplet solutions.

Parameter	Value
T_∞	256.49K
P_∞	90.76 kPa
U_∞	102.8 m.s^{-1}
AOA	4^{o}
MVD	20μm
LWC	0.55g/m^3
Re_∞	4.14×10^6

Table 5.2: Ambient conditions corresponding to Run 404.

The behavior observed during the first time steps is still observable in the final ice shape after 7 minutes of accretion. Figure 5.15 shows the final ice shape computed by LEWICE and ICE3D-SWIM, compared to the experimental ice shape obtained in the IRT. The limits of impact are identical for LEWICE and ICE3D-SWIM and match the experiments on the suction side of the airfoil but are under predicted by both codes on the pressure side of the airfoil. ICE3D-SWIM's ice shape is thicker and closer to the experimental ice shape than LEWICE on the upper part of the airfoil. This may be due to a larger estimation of the water evaporation from LEWICE. ICE3D-SWIM also predicts a slightly smaller ice thickness on the pressure side where the LEWICE solution is closer to the measurement.

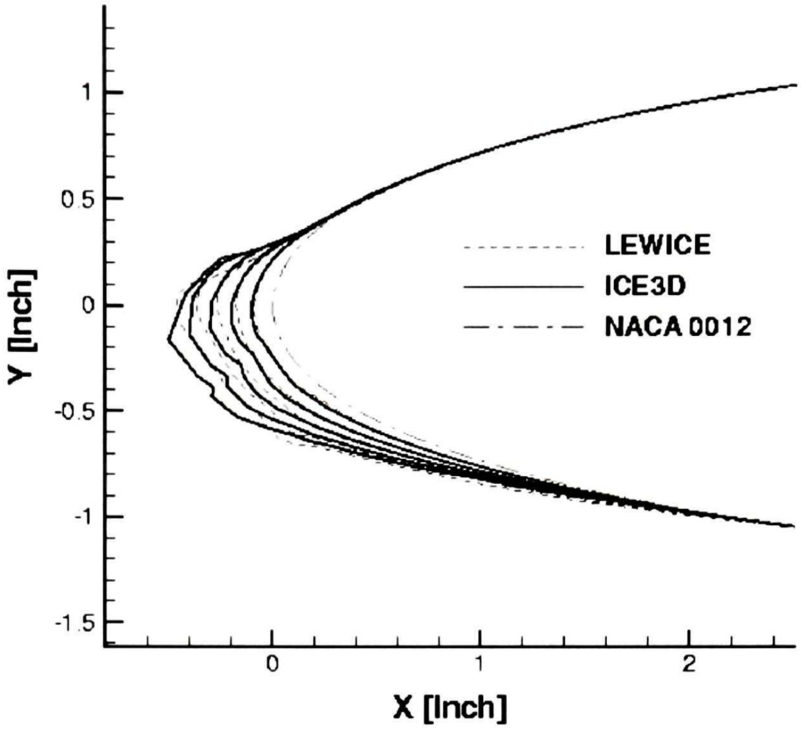

Figure 5.14: Run 404 [NASA CD-ROM] comparison between ICE3D-SWIM and LEWICE after 1, 2, 3, 4 and 5 min of ice accretion.

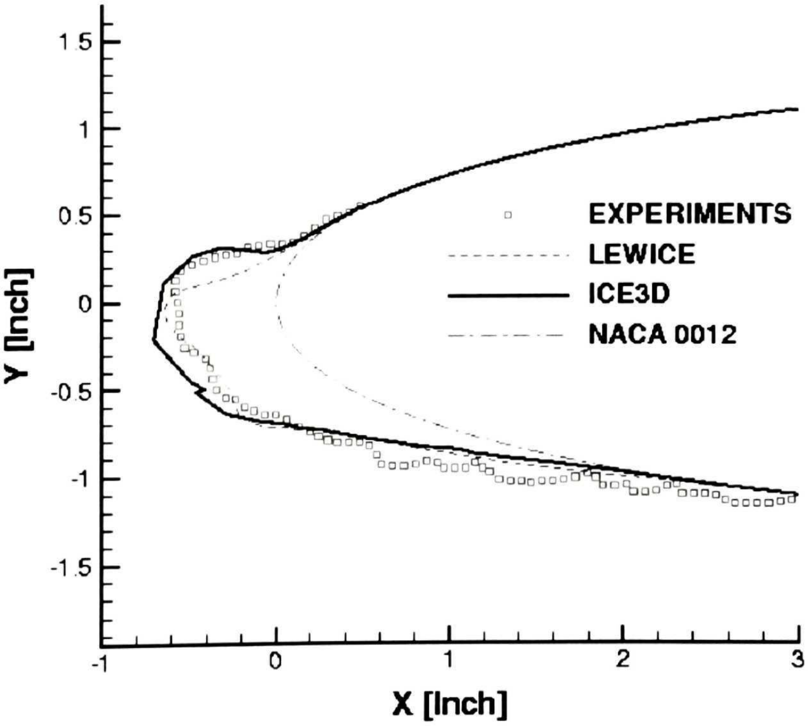

Figure 5.15: Run 404 [NASA CD-ROM] comparison between LEWICE, and IRT experimental ice shape.

5.3.2. Run 308

In the second comparison, ice is accreted on a NACA 0012 airfoil at an AoA of 4° for 231 seconds. The ambient conditions, closer to glaze ice conditions, are summarized in table 5.3 and correspond to LEWICE Run 308[66].

Figure 5.16 shows the comparison between LEWICE and ICE3D-SWIM numerical solutions after 47.58 and 95.16 seconds of accretion. At 47.58 seconds of accretion, ICE3D-SWIM and LEWICE solutions are identical: same ice thickness and limits of impact for both codes. After 95.16 seconds of accretion, LEWICE and ICE3D-SWIM solutions remain very close to each other, LEWICE predicting a slightly bigger amount of runback than ICE3D-SWIM. Both codes predict the formation of a horn on the upper part of the NACA 0012 airfoil, with the same angle and ice thickness.

Parameter	Value
T_∞	262.04K
P_∞	90.76 kPa
U_∞	102.8 m.s^{-1}
AOA	4^{0}
MVD	20μm
LWC	1g/m^3
Re_∞	4.14×10^6

Table 5.3: Ambient conditions corresponding to Run 308.

After 95.16 seconds of accretion, the horn predicted by ICE3D-SWIM induces a separation in the flow solution. Contrary to LEWICE, which may be able to predict but not compute separation with only a viscous/inviscid interaction, ICE3D-SWIM's convective heat transfer coefficient and shear stress decrease suddenly in the separation area. As a consequence impact may be predicted behind a horn as can be seen in figure 5.16. ICE3D-SWIM's final ice shape is very close to LEWICE's. But both codes fail to predict the horn's angle of the experimental ice shape. There is still room for improvement in the quality of ice accretion shape predictions yielded by current icing codes, as large differences between predicted and experimental ice shapes are often encountered[68] in glaze ice conditions, compounded by the problem of the lack of consistency of ice shapes produced in icing wind tunnels.

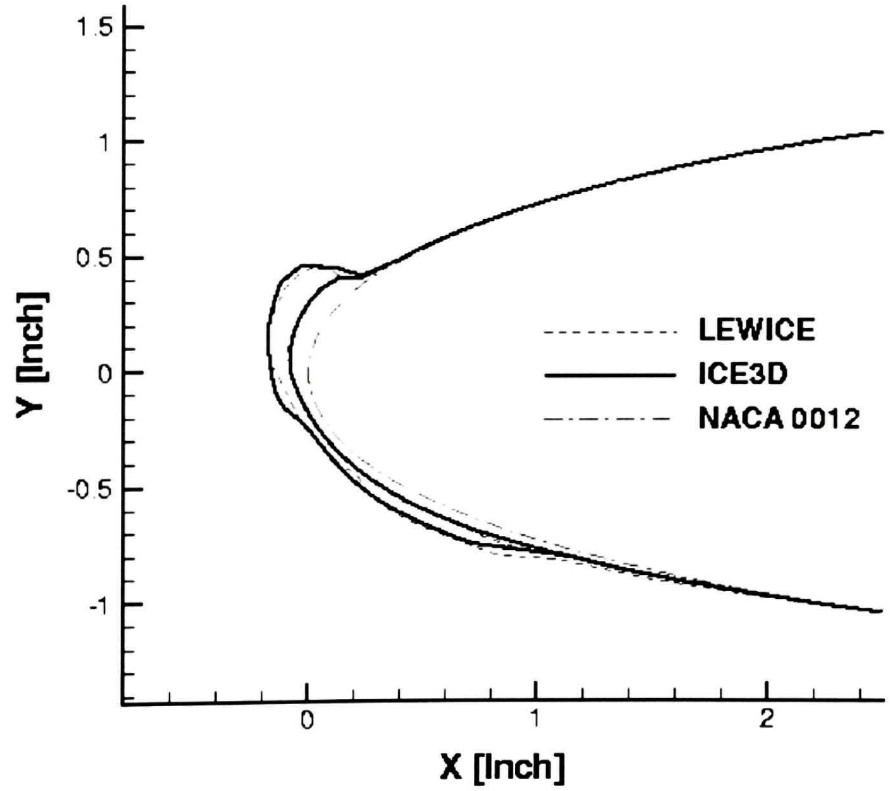

Figure 5.16: Run 308 [NASA CD-ROM] comparison between ICE3D-SWIM and LEWICE after 47.58 and 95.16 s of ice accretion.

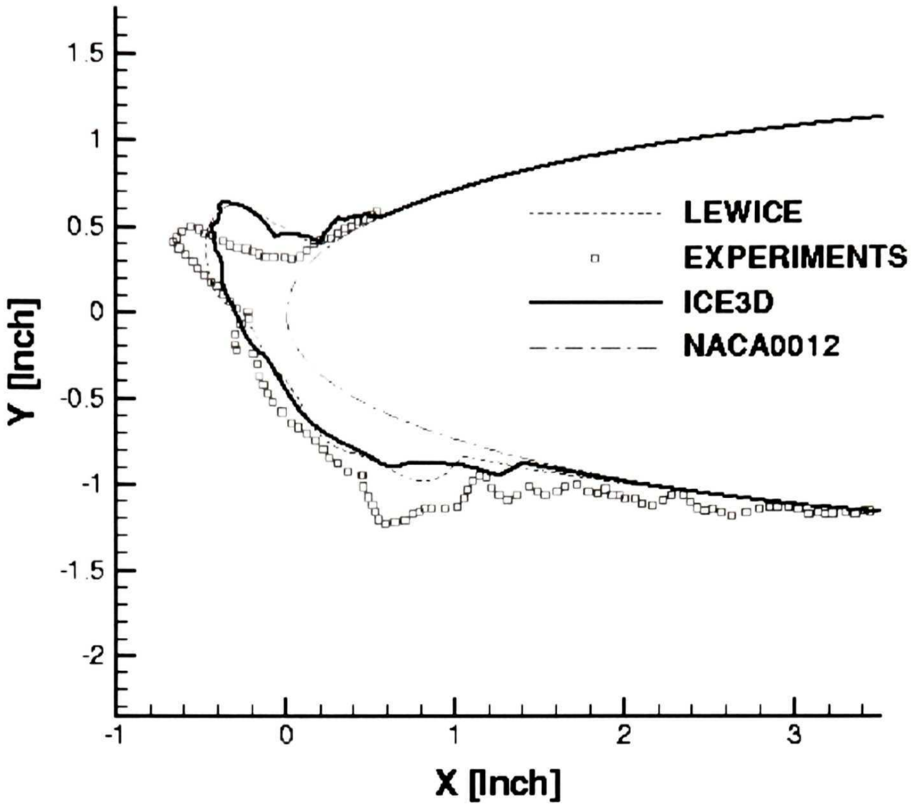

Figure 5.17: Run 308 [NASA CD-ROM] comparison between ICE3D-SWIM, LEWICE and IRT experimental ice shape.

5.4. Cambered airfoil: NLF-0414

The NLF-0414 airfoil is representative of a laminar flow design for general aviation. It is shown in figure 5.18.

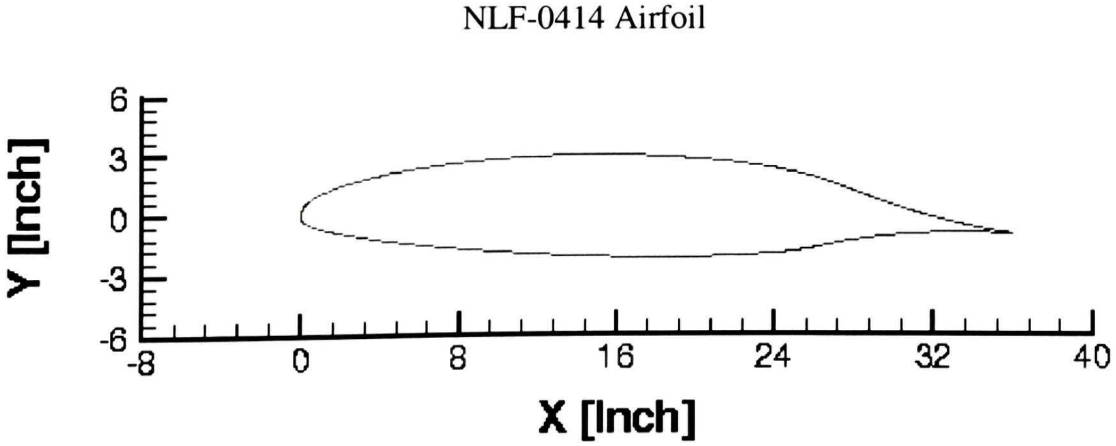

Figure 5.18: NLF-0414 Airfoil.

For the NLF-0414 airfoil, a glaze ice test case, corresponding to Run 623[66], has been chosen. In this particular test case, LEWICE fails to predict the ice shape. ICE3D-SWIM is run to see if the same difficulties are encountered. The ambient conditions of this run are presented in table 5.4

Parameter	Value
T_∞	267.30K
P_∞	90.76 kPa
U_∞	66.9 m.s^{-1}
AOA	2^o
MVD	20μm
LWC	0.54g/m^3
Re_∞	4.289×10^6

Table 5.4: Ambient conditions corresponding to Run 623.

Ice is accreted on the NLF airfoil at an AoA of 2^o for 22.5 minutes. A one-shot ice accretion is performed and is compared to the LEWICE solution and the experimental measurements in figure 5.19, where the dimensions used are still expressed in inches. Following the other 2D test cases performed with the present code, it is considered that a one-shot ice accretion would be sufficient to conclude if our numerical code encounters the same difficulties as LEWICE for this test case, even though LEWICE performed a multi-stepping approach with 15 layers. As can be shown in figure 5.19, the ICE3D-SWIM shape is closer to the experimental solution on the suction side of the airfoil.

Contrary to LEWICE, ICE3D-SWIM predicts well the location and angle of the horn. However, on the pressure side, the LEWICE prediction is slightly better than ICE3D-SWIM, but both codes predict qualitatively similar ice shapes. LEWICE difficulties to accurately predict collection efficiency on the NLF-0414[77] airfoil can be surmised as a problem due to the airflow solution, which is not amenable to a panel method calculation because of the importance of the boundary layer. Taking figure 5.12 as a possible reference, a multi-stepping approach will probably increase the size of the horn and improve the solution on the pressure side of the airfoil.

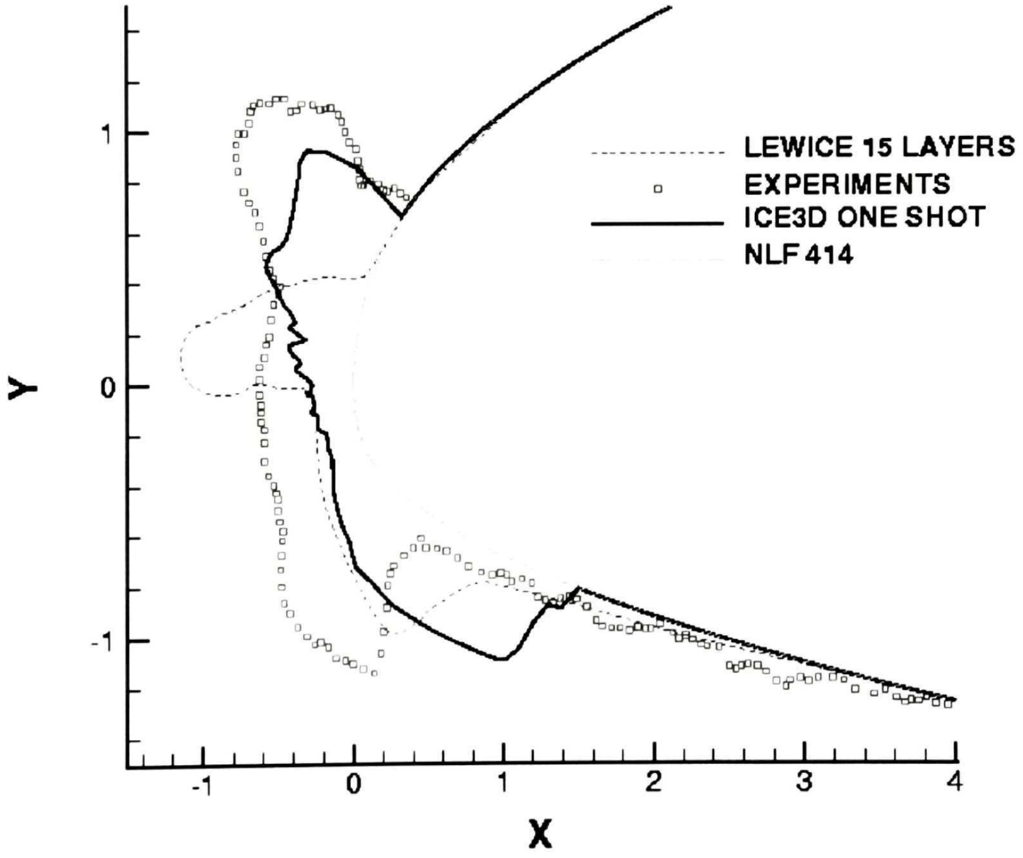

Figure 5.19: Run 623 [CD-ROM], comparison between ICE3D-SWIM, LEWICE and IRT experimental ice shape.

5.5. Conclusions

This chapter presents some 2D results obtained on 3D meshes of one element thickness. The resulting ice shape, for each test case, is compared to LEWICE numerical ice shape and the experiments obtained in the IRT. These preliminary 2D validations are encouraging. The proposed in-flight system is able to predict ice shapes in rime and glaze ice situations on symmetrical and cambered airfoils. The complexity of the ice shape and the details will increase if a finer grid is used and/or if a multi-stepping approach, with airflow and impingement updates, is selected. It is common to observe that wind tunnel experimental ice shape limits on the pressure side of the airfoil are further than those predicted by numerical codes. This phenomenon cannot be explained easily and require much more investigations. The validation of ICE3D-SWIM continues in chapter 6 with a couple of 3D test cases.

Chapter 6

Three-dimensional Results

In icing, three-dimensional experimental results are not numerous. Moreover, when three-dimensional experiments are done, the results are most of the time not publicly available or the geometry used during the tests is confidential. Hence, it is not easy to find 3D experimental data to compare with.

In this chapter, two 3D test cases have been selected to test the new algorithms for ice accretion simulations. In the first one, a 3D Eurocopter/ONERA helicopter rotor blade tip, the results of Hedde and Guffond[23] were chosen, and from their published information, clearly given as being based on known NACA 13106 airfoils, we were able to reconstruct a complete three-dimensional geometry with which to carry out the calculations[71]. However, after some talks with Eurocopter engineers, it appears that the geometry may have been initially based on NACA 13106 airfoils, but that the final airfoils are quite different from that base shape. It became clear that the exact geometry was and will remain confidential. As a consequence, the three-dimensional results can only be compared qualitatively.

In the second test case, a non-axisymmetric Boeing 737-300[72] inlet nacelle is selected. Airflow solution, droplets impingement and ice accretion have been performed and are compared[73] with numerical and/or experimental results, whichever available.

6.1. 3D helicopter rotor blade tip results

A three-dimensional helicopter rotor tip geometry is succinctly described in reference 23 as follows: "from the base to the top along the span, the chord varies from 0.6 to 0.2m, the leading edge sweep angle starts at 0 and ends at 60deg. The trailing edge is perpendicular to the flow and is lightly spun so that the incidence angle at the top is 0.74 deg less than at the base. The span is 0.48m. The rotor blade tip is built from a NACA 13106 airfoil". The CAD of the geometry was produced with the ICEM DDN software. The one-equation Spalart-Allmaras model was used for turbulence modeling within FENSAP and mesh adaptation was carried out with OptiMesh[74], an automatic anisotropic (highly directional and highly stretched) mesh adaptation code. It should be noticed that the rotor blade tip was fixed in the wind tunnel during experiments and not in rotation.

6.1.1. Airflow solution and mesh adaptation

The ambient conditions for the simulation are shown in table 6.1. To improve the quality of the flow solution, three mesh adaptations cycles were carried out with OptiMesh. The OptiMesh algorithm utilizes mesh movement, edge refinement, coarsening and swapping to automatically yield a nearly-optimal anisotropic (highly stretched) adapted grid. Figure 6.1 shows a 2D cut of the original mesh which contains 221,800 nodes and 1,118,131 elements, and figures 6.2, 6.3 show the last adapted grid containing 467,705 nodes and 2,546,857 elements.

Parameter	Value
T_∞	-30.5°C
P_∞	45.6 kPa
Mach	0.52
AOA	9.5°
MVD	20μm
LWC	1g/m^3
time	91s

Table 6.1: Ambient conditions, helicopter rotor blade tip.

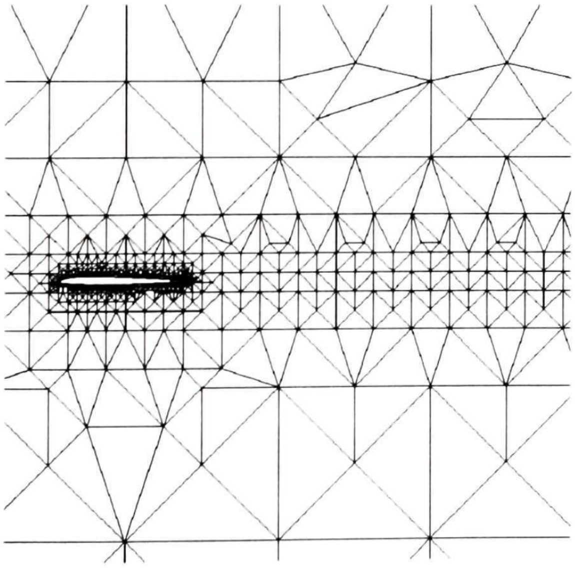

Figure 6.1: 3D rotor blade tip, initial mesh.

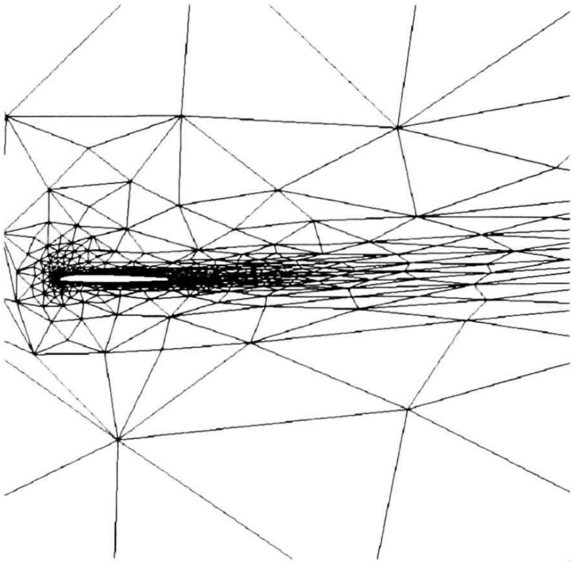

Figure 6.2: Third mesh adaptation on the 3D rotor blade tip.

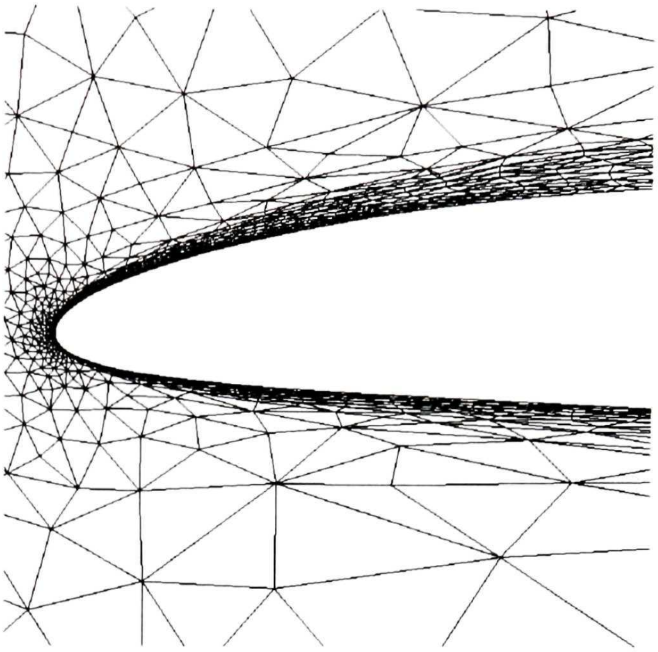

Figure 6.3: Zoom on the third mesh adaptation, 3D rotor blade tip.

The equivalent sandgrain roughness used is obtained with equation (3.7) of chapter 3 and corresponds to 0.269 mm in this case. To help the discussion of the results, two-dimensional (X,Z) cuts at four different spanwise locations are presented. The cuts are referred to as station 1 (location Y=0.09m), station 2 (Y=0.25m), station 3 (Y=0.30m) and station 4 (Y=0.45m). The origin of the coordinate system is at the root of the wing at the leading edge. The X-axis is in the chordwise direction, the Y-axis is in the spanwise direction and the Z-axis is in the normal direction to the plane (X,Y); (X,Y,Z) being the Cartesian reference system.

As presented in figure 6.4, the finite blade modeled engenders 3D aerodynamic effects, first with the creation of an aerodynamic angle of attack locally different from the free stream and, second, with the creation of a tip vortex at the blade extremity. Due to a negative twist angle and a high AoA, the numerical solution shows a separation and a small sweep angle. All aerodynamic variables are affected by this flow pattern. The distributions of turbulent viscosity are presented in figure 6.5. Figure 6.6 shows the convective heat transfer coefficient for stations 1, 2, 3 and 4. The heat transfer coefficient curves are quite similar along the blade, except close to the tip where the separation decreases the airspeed and hence the heat transfer coefficient.

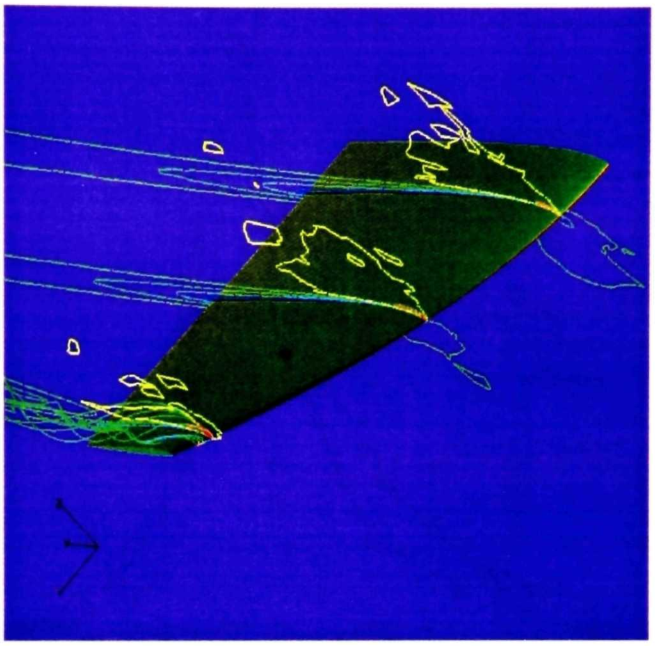

Figure 6.4: Three-dimensional rotor blade tip, turbulent airflow solution, Mach number contours, and streamlines at the tip.

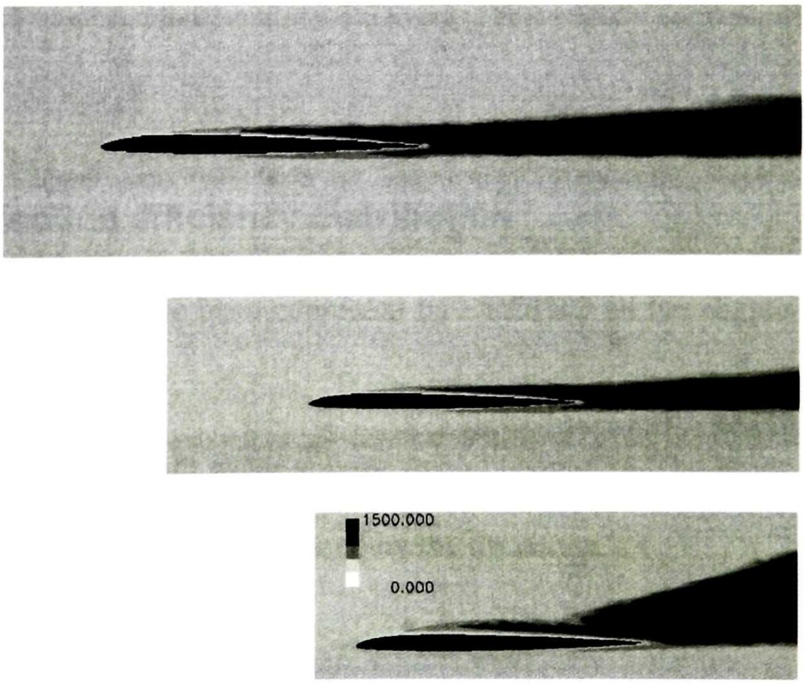

Figure 6.5: Turbulent viscosity distribution at stations 1, 2 and 4.

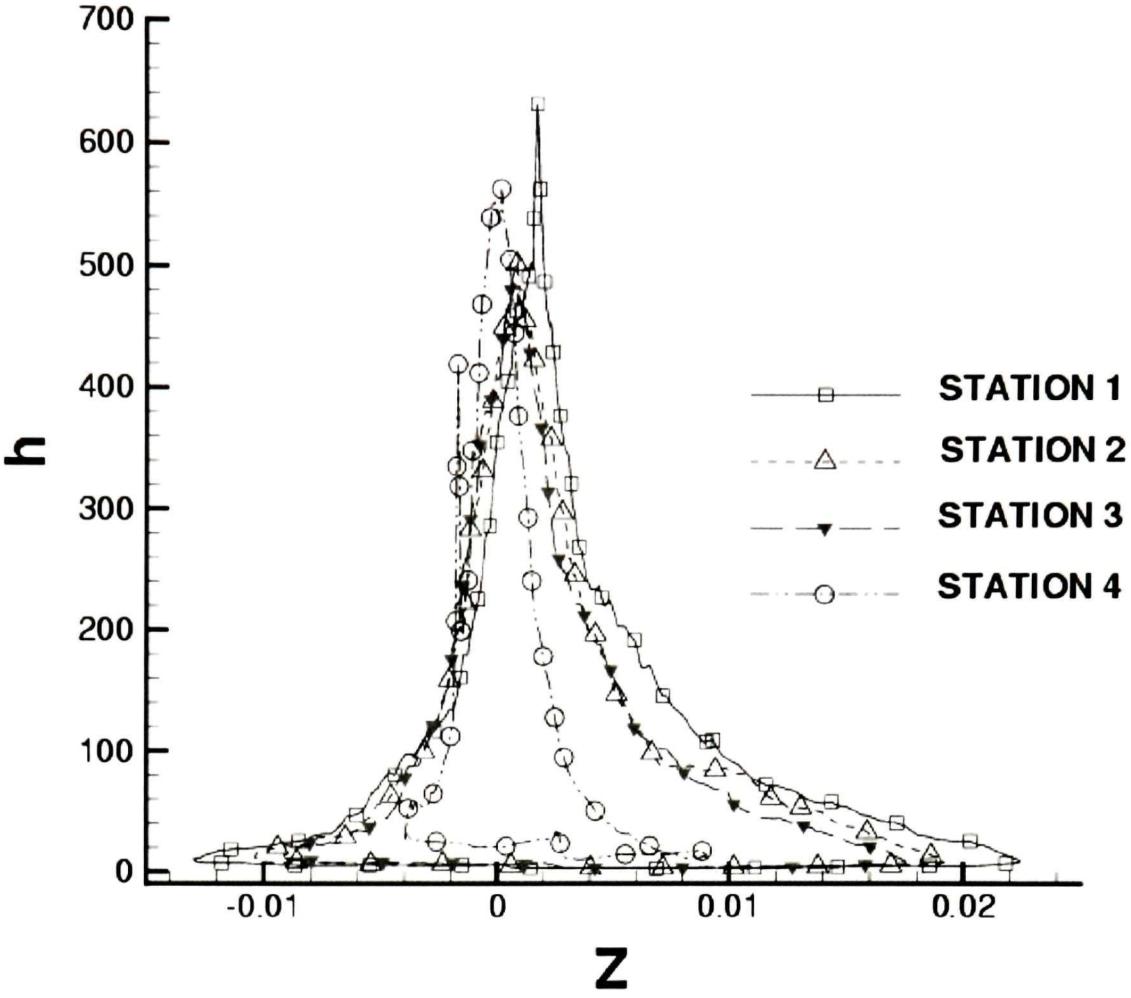

Figure 6.6:Two-dimensional cuts of the convective heat transfer coefficient, in W/m^2K.

6.1.2. Collection efficiency distribution

The droplet solution has also been computed by DROP3D on the adapted grid, using the FENSAP adapted airflow solution. Figure 6.7 presents the collection efficiency distribution on the blade, with water volume fraction contours. The water volume fraction increases in the recirculation zone induced by the tip vortex.

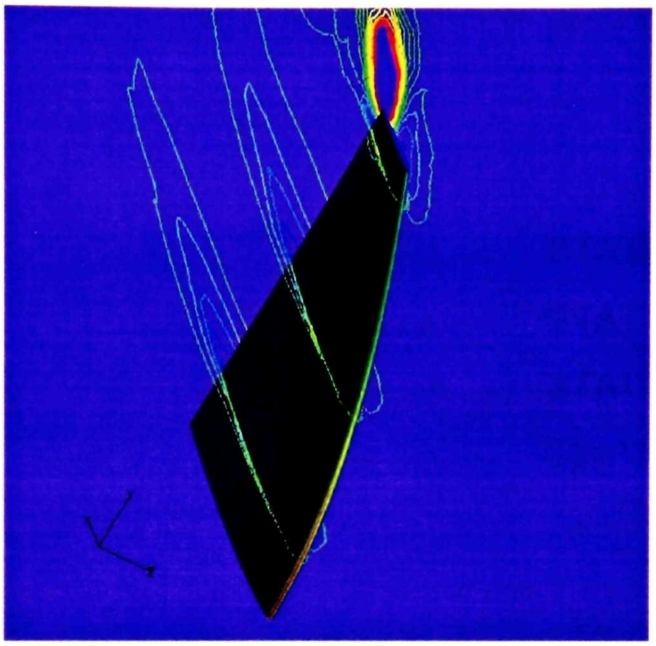

Figure 6.7: Collection efficiency distribution on the wing and liquid water volume fraction contours for stations 1, 2, and 4.

The maximum of the collection efficiency increases with the length of the chord. In figures 6.8 and 6.9, the airfoil corresponding to each station is presented in non-dimensional units, using the chord length, to make comparison easier. Usually, the β curves are created using curvilinear coordinates with the origin located at the stagnation point. Finding the stagnation line in 3D is, however, not always an easy task, and we choose to represent the curves in the inner coordinates (X,Y,Z) even if it becomes a little more difficult to find the part of the curve corresponding to the upper part of the wing and the one corresponding to the lower part. The limit of impingement on the lower side of the blade extends further back closer to the tip (figure 6.8). On the other hand, the impingement limit on the upper side of the blade decreases from station 1 to station 4 (zone of positive Z in figure 6.9), showing a three-dimensional effect due to the negative twist angle.

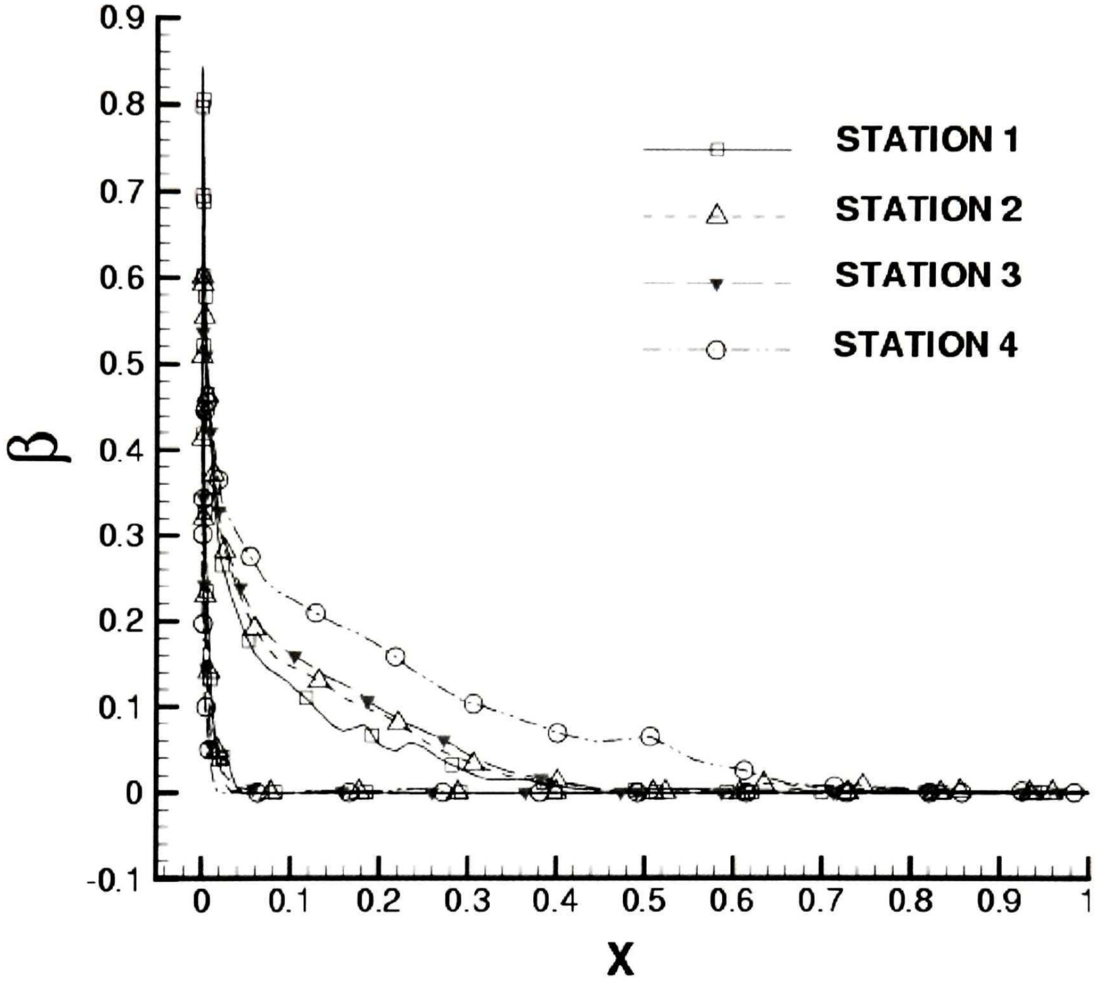

Figure 6.8: Two-dimensional cuts of the collection efficiency for stations 1-4 along the non-dimensional X axis, the chord direction.

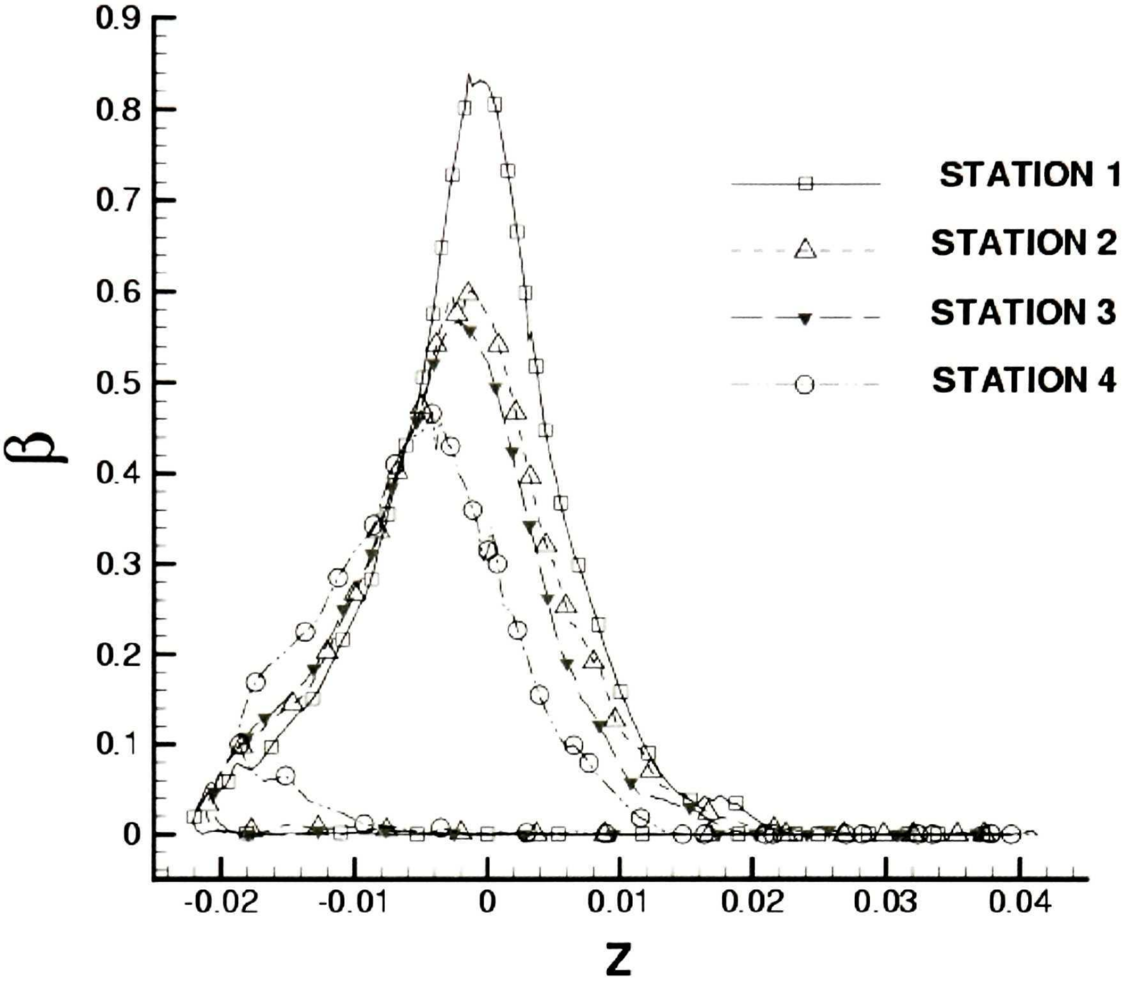

Figure 6.9: Two-dimensional cuts of the collection efficiency for stations 1-4 along the Z axis.

6.1.3. Ice accretion

Once the FENSAP airflow solution and the collection efficiency from DROP3D have been determined, ice accretion can be performed on the adapted grid. The 91-second exposure was simulated in one shot. The effect of intermediate airflow solutions with automatic mesh movement using ALE was not studied in this case, as the unavailability of experimental data did not warrant the additional effort. Figure 6.10 gives a 3D view of the ice accretion at the tip. The apparent roughness is due to the discrete representation of the surface by triangular faces. Ice is assumed to grow in the direction normal to the wing surface. Two-dimensional cuts of the ice shape corresponding to station 1, 2, 3, and 4 are plotted in figure 6.11. The global aspect of the ice shape qualitatively agrees with the numerical and experimental results of ONERA, figure 6.12. However no closer comparison can be made because of the discrepancies between the real geometry and the published one. In figure 6.12, we respect the scale published in reference 23. It would have been interesting to compare with results from another 2D icing code, but none of the existing codes was available for carrying out such a comparison. The 3D effects are not spectacular, as the geometry does not present strong 3D features and the very cold temperature corresponds to rime ice conditions, making water runback less of an important factor.

Figure 6.10: Three-dimensional ice shape at blade tip.

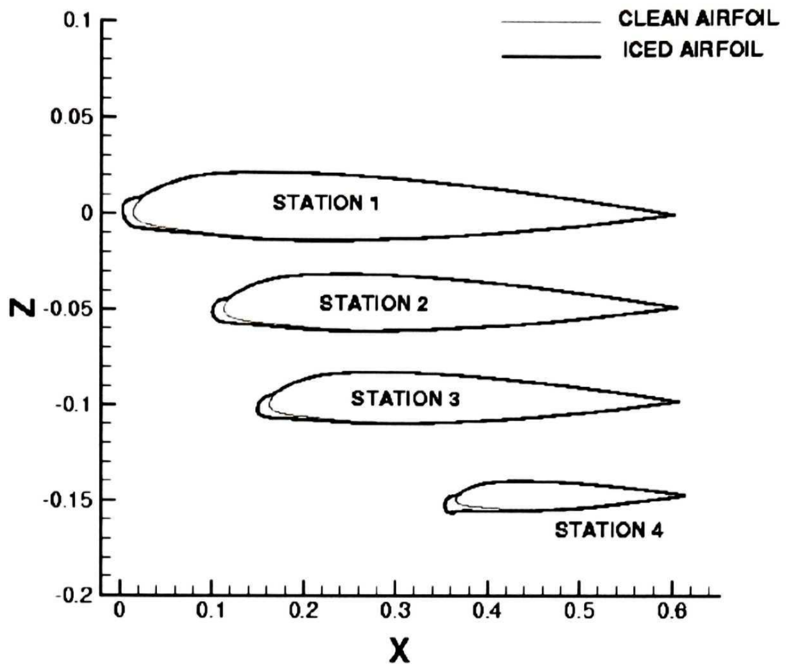

Figure 6.11: Two-dimensional ice cuts along the spanwise direction for stations 1-4.

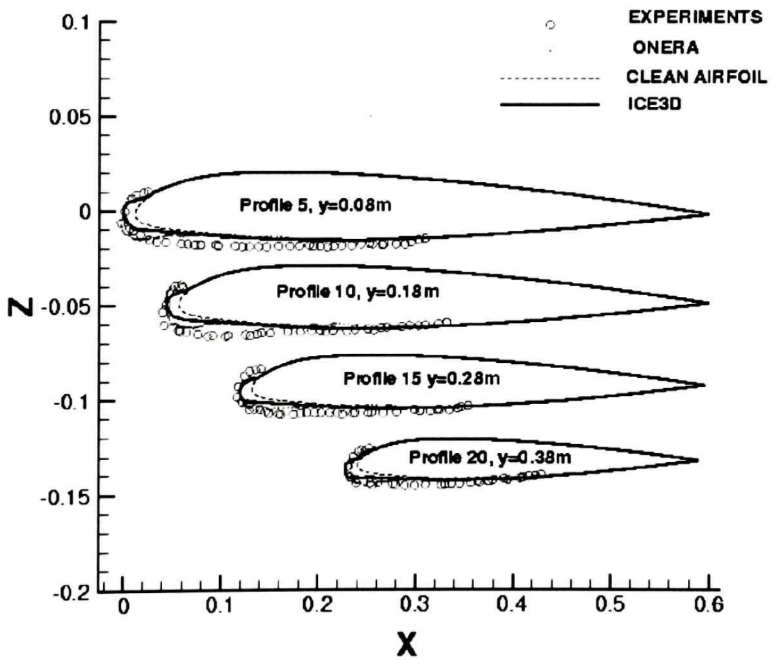

Figure 6.12: Two-dimensional ice cuts along the spanwise direction; comparison between ICE3D-SWIM and ONERA numerical solutions with the experimental solution.

To highlight ICE3D-SWIM's predictive three-dimensional capabilities, the convective heat flux has been modified, figure 6.13, to produce icing with runback and the results of that study is presented in figures 6.14 and 6.15.

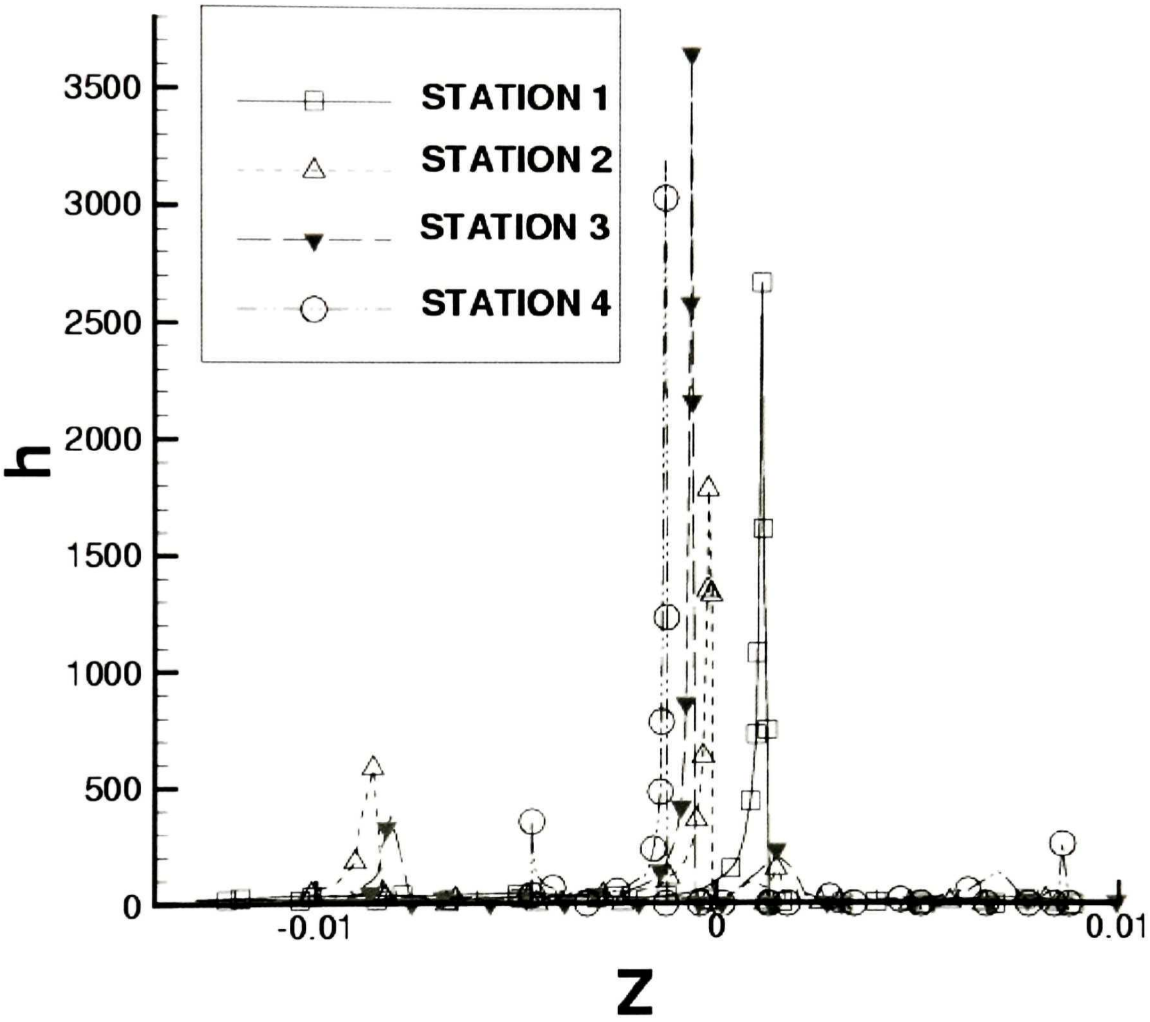

Figure 6.13: Two-dimensional cuts of the modified convective heat transfer coefficient, in W/m^{2}K.

The results may have no real physical meaning, but they show that the numerical method can predict three-dimensional icing with runback. Two-dimensional cuts corresponding to station 1, 2, 3 and 4 are also plotted in figure 6.15. The water runback in that case is quite important. The resulting ice shape is a lot more complex than the previous one, especially close to the tip where the separation and tip vortex dramatically affect the ice accretion profile. It is also possible to observe drastically different spanwise behavior of the ice accretion process, on a single geometry.

Figure 6.14: Three-dimensional ice shape at blade tip.

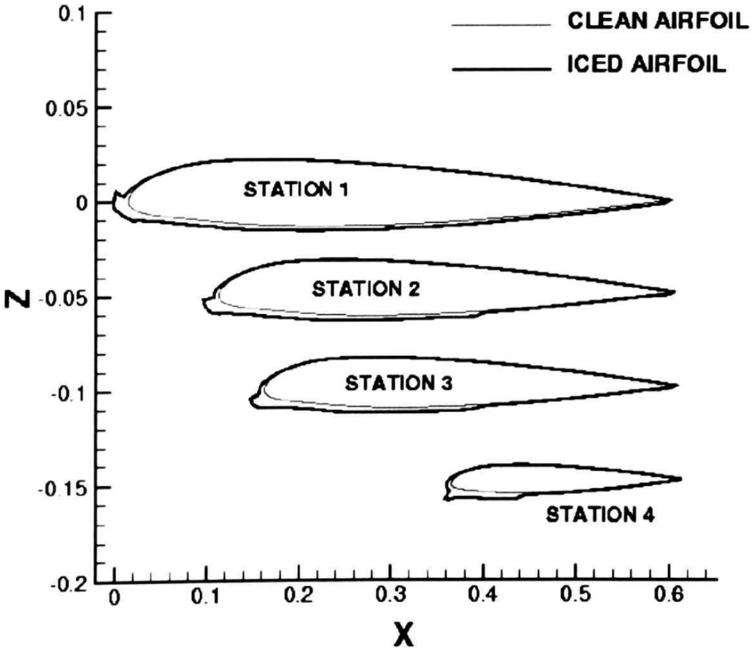

Figure 6.15: Two-dimensional ice cuts along the spanwise direction for stations 1-4.

6.2. Boeing 737-300 inlet nacelle

In this exercise we intend to predict ice accretion on a 3D non-axisymmetric Boeing 737-300[75] nacelle inlet and compare ICE3D-SWIM's predictions to LEWICE's. A Complete set of computational and experimental results, made by NASA[72], are available for the airflow solution and the collection efficiency. The icing calculation process requires three steps: the computation of the airflow solution, the computation of the droplet solution and the prediction of the ice shape. Each "step solution" will be compared to LEWICE's solutions and the experiments, whichever is available.

Two cases were analyzed at different incidences of the nacelle: they correspond to run id 092385-1, 2, 3-737-0 in reference 75 for 0 degree nacelle incidence, and run id 092385-13, 14, 15-737-15 in reference 75 for 15 degree nacelle incidence. Five circumferential positions, sketched in figure 6.16, have been selected to make the comparisons; they correspond to the experimental blotter strip locations (see Appendix).

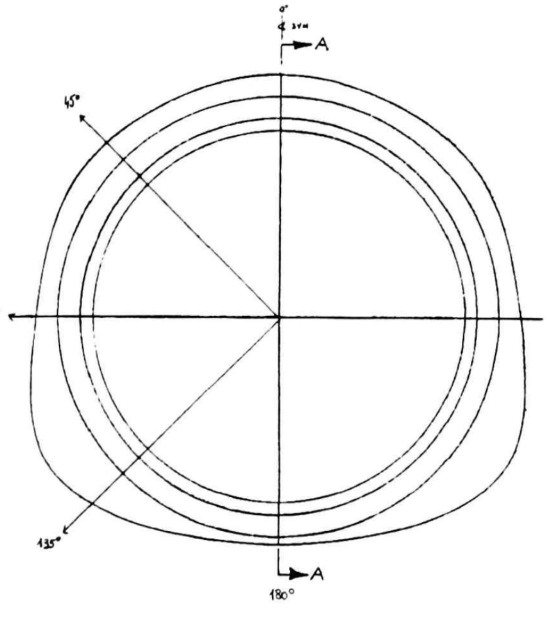

Figure 6.16: Experimental blotter strip locations on the 3D Boeing 737-300 inlet nacelle.

6.2.1. Airflow solutions

Two cases were analyzed at an airspeed of 75 m/s, inlet mass flow of 10.4 kg/s, static temperature of 7°C, static pressure of 95840 Pa and nacelle incidences of 0 and 15 degrees. Euler solutions have first been calculated on this geometry and the results have been published by Tran *et al.*[76]. Turbulent airflow solutions using the S-A model are then computed. Four mesh adaptation cycles have been performed with OptiMesh. The original mesh and the final one corresponding to the 15 degree incidence solution are shown in figures 6.17 and 6.18.

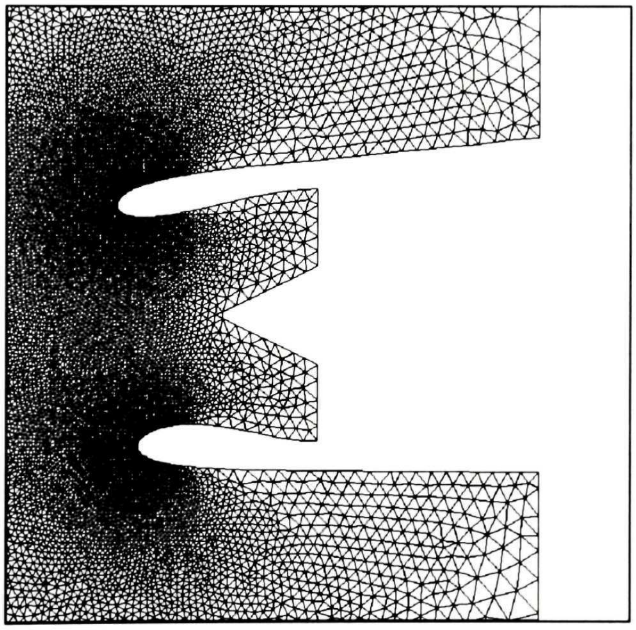

Figure 6.17: Original mesh (symmetry plane).

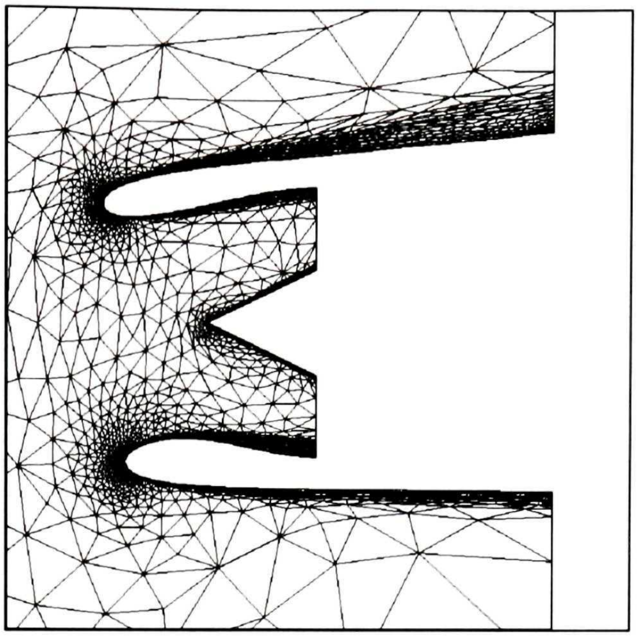

Figure 6.18: Final adapted mesh corresponding to the 15 degree incidence solution (symmetry plane).

Experimental data available for the airflow solution give access to the Mach number distribution for the five circumferential positions. Using the distribution of the pressure coefficient at the wall from the Navier-Stokes solution, the Mach number distribution at the edge of the turbulent boundary layer is recovered. Therefore, the Mach number distribution for Navier-Stokes and Euler solutions can be compared to experimental measurements. For all circumferential cuts and both incidences, the turbulent airflow solution agrees very well with the Euler solution, two 2D cuts are presented in figures 6.19 and 6.21. The influence of mesh adaptation on the solution can be seen in figures 6.20 and 6.22. At the end, regarding the two last cycles of mesh adaptation, the solution appears to be mesh-independent.

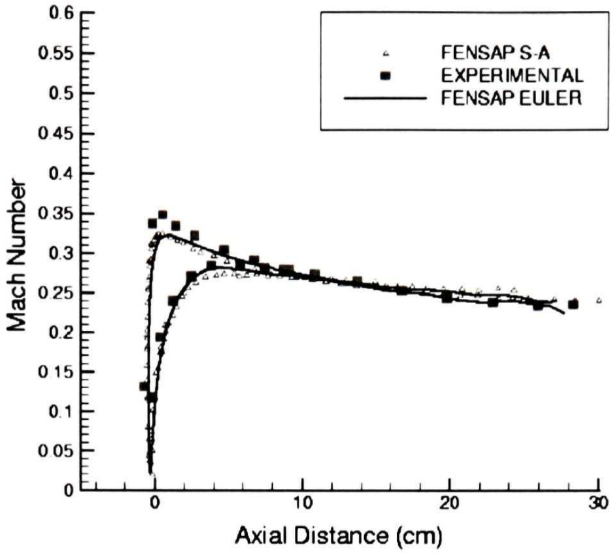

Figure 6.19: Mach number distribution for the Boeing 737-300 inlet for 15 deg AoA and an inlet mass flow rate of 10.4 kg/s; comparison at 0 deg circumferential position between Navier-Stokes solution (FENSAP S-A), Euler solution (FENSAP EULER) and Experiments.

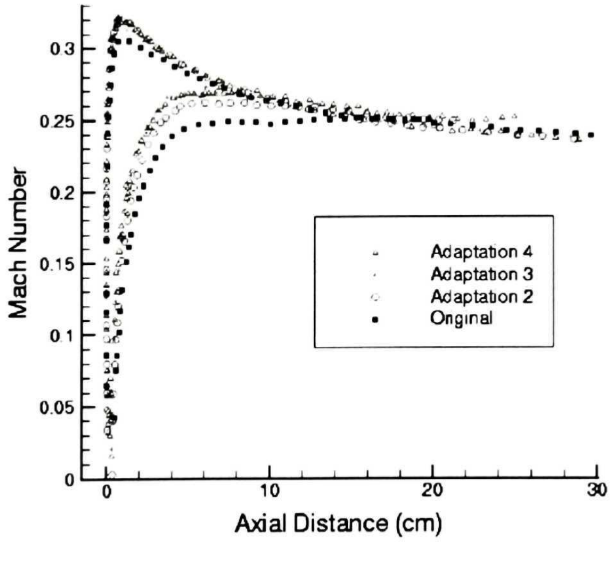

Figure 6.20: Influence of mesh adaptation on the 15 deg AoA Navier-Stokes solution, comparison at 0 deg circumferential position.

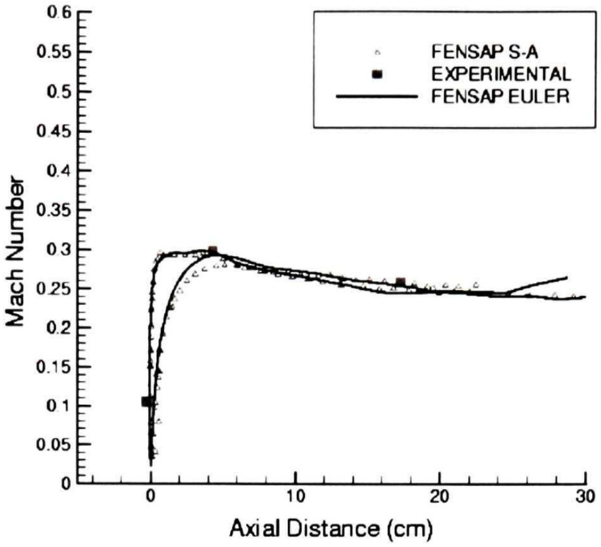

Figure 6.21: Mach number distribution for the Boeing 737-300 inlet for 15 deg AoA and an inlet mass flow rate of 10.4 kg/s; comparison at 45 deg circumferential position between Navier-Stokes solution (FENSAP S-A), Euler solution (FENSAP EULER) and Experiments.

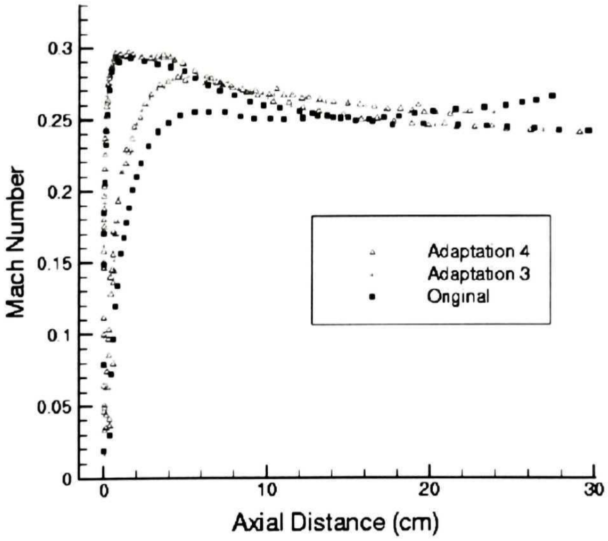

Figure 6.22: Influence of mesh adaptation on the 15 deg AoA Navier-Stokes solution, comparison at 45 deg circumferential position.

The calculated Euler Mach number distributions compared to experimental data and LEWICE results for both incidence and all circumferential positions are presented in Appendix, figures A-3 and A-4. The calculated Mach number distributions are in very good agreement with both experimental data and with LEWICE results, for all circumferential positions, at both incidences.

6.2.2. Droplet impingement

In order to compute the local catch efficiency β, DROP3D was run for a Langmuir-D droplet distribution with a droplet mean volumetric diameter (MVD) of $20.36 \mu m$ and the same ambient conditions of the airflow solution, figure 6.23. The comparison of local catch efficiency distribution along the same circumferential cuts is presented in figures 6.25 and 6.26 pages 145 and 146. The comparison between DROP3D and experimental data is very good for most circumferential positions for both incidences. The limits of impingement are correctly predicted and the local catch efficiency peak in amplitude is shown to be within experimental capability estimated in reference 75 to be between 0.2 and 0.25. The results show that, while DROP3D and LEWICE catch efficiency results agree over most of the nacelle, the impingement limits predicted by DROP3D are closer to experiments. The curves for 15 deg. incidence and 135 deg. circumferential positions are, however, not in close agreement with the experimental data. Nevertheless, the predictions of LEWICE are even further from experiments. Since the comparison at zero incidence for the same circumferential position is very good and all other comparisons at 15 deg. incidence are also quite acceptable for both codes, it is only logical to conclude that the difference for that particular curve may be due to experimental inaccuracies.

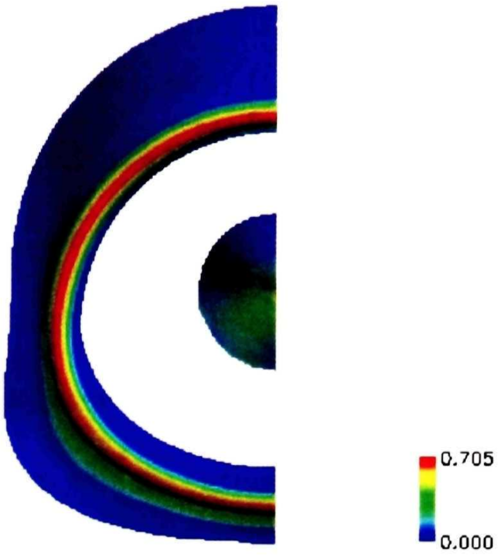

Figure 6.23: 3D impingement solution (Langmuir-D distribution: 20.36μm MVD) on the Boeing 737-300 inlet, at 0° AoA and an inlet mass flow of 10.4 kg/s.

6.2.3. Ice accretion

Two icing conditions were calculated for each incidence of the Boeing 737-300 inlet. The conditions were chosen to represent a rime and a glaze ice situation. The rime conditions are the following: an accretion time of 30 minutes with a LWC of 0.2 g/m^3 and a static temperature of -29.9°C. For the mixed condition, the time of exposure is still 30 minutes but the LWC is 0.695 g/m^3 and the static temperature is -9.3°C. Both LEWICE[72] and ICE3D-SWIM have performed one-shot ice accretion simulations since no experimental data were available. A 3D view of the ice shape obtained on the nacelle is shown in figure 6.24, page 144.

In the rime ice case, the comparison between LEWICE and ICE3D-SWIM is very good for all circumferential positions and for both incidences, figures 6.27 (page 147) and 6.28

(page 148). For the glaze ice condition, the LEWICE and ICE3D-SWIM predicted ice shapes, figures 6.29 and 6.30 (pages 149 and 150), agree pretty well for all circumferential positions and for both incidences.

Although no experimental data was available, it is comforting that the results obtained by the two codes are in good agreement and looked consistent with the conditions for which the shapes were generated and with the airflow and droplet solutions.

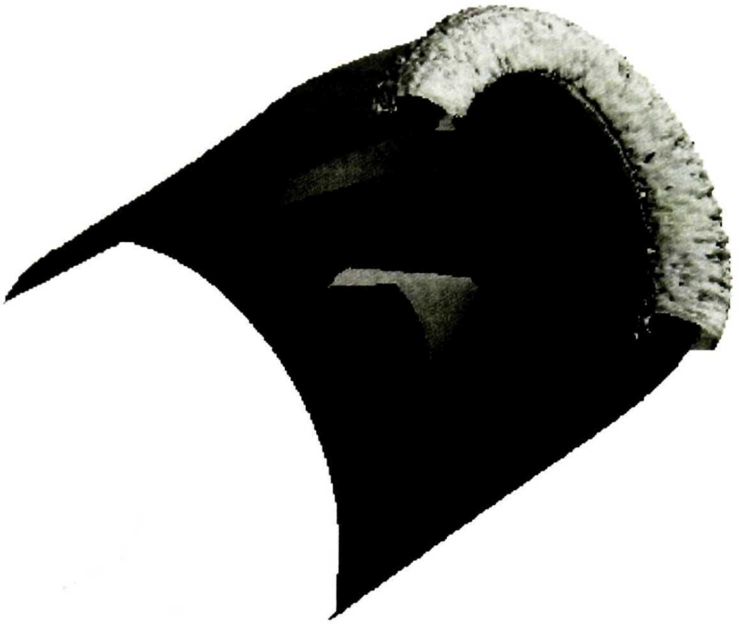

Figure 6.24: 3D ice accretion on the Boeing 737-300 inlet, rime ice accretion for 15° AoA and an inlet mass flow of 10.4 kg/s.

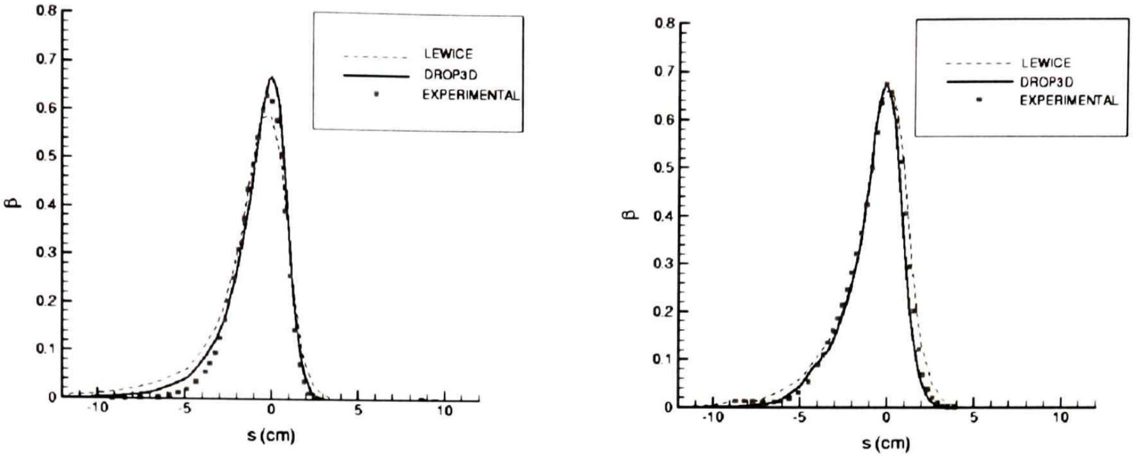

circumferential position: $\theta = 0°$ circumferential position: $\theta = 45°$

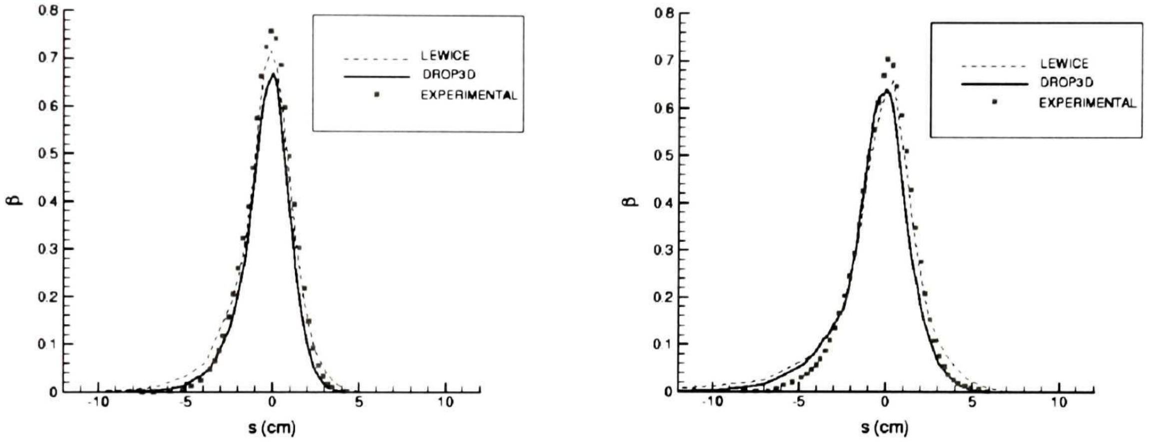

circumferential position: $\theta = 90°$ circumferential position: $\theta = 135°$

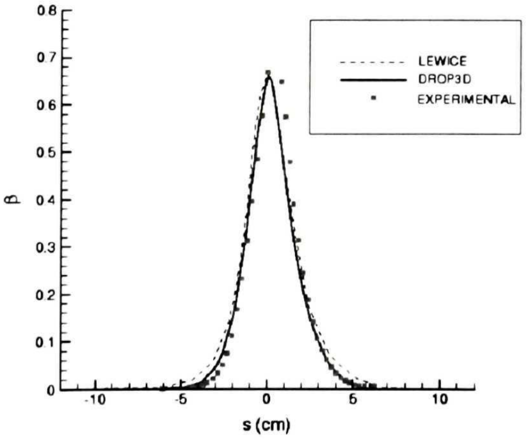

circumferential position: $\theta = 180°$

Figure 6.25: Local collection efficiency distribution for 0° AoA, comparison between DROP3D, LEWICE and Experiments.

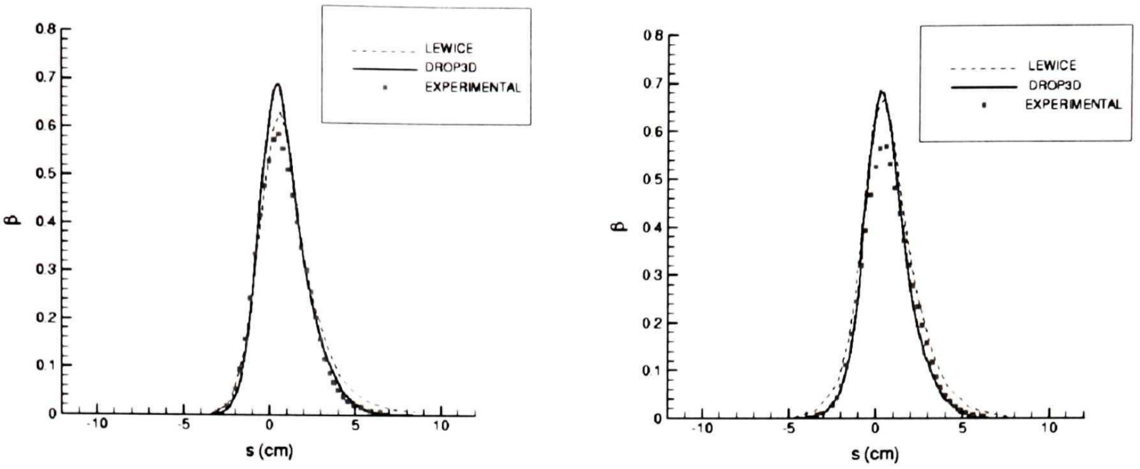

circumferential position: $\theta = 0°$ circumferential position: $\theta = 45°$

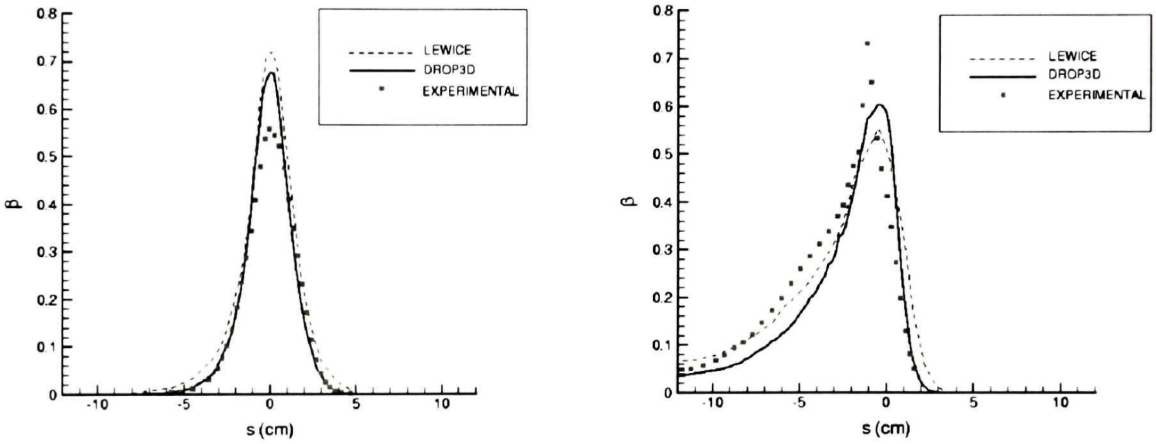

circumferential position: $\theta = 90°$ circumferential position: $\theta = 135°$

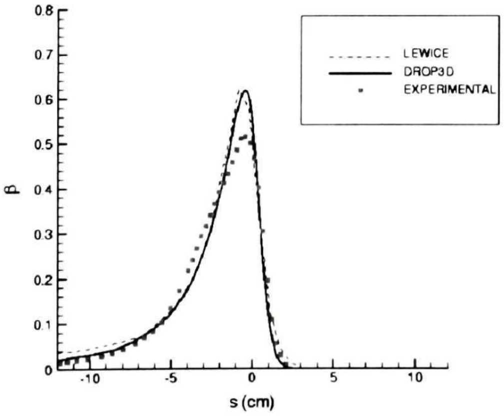

circumferential position: $\theta = 180°$

Figure 6.26: Local collection efficiency distribution for 15° AoA, comparison between DROP3D, LEWICE and Experiments.

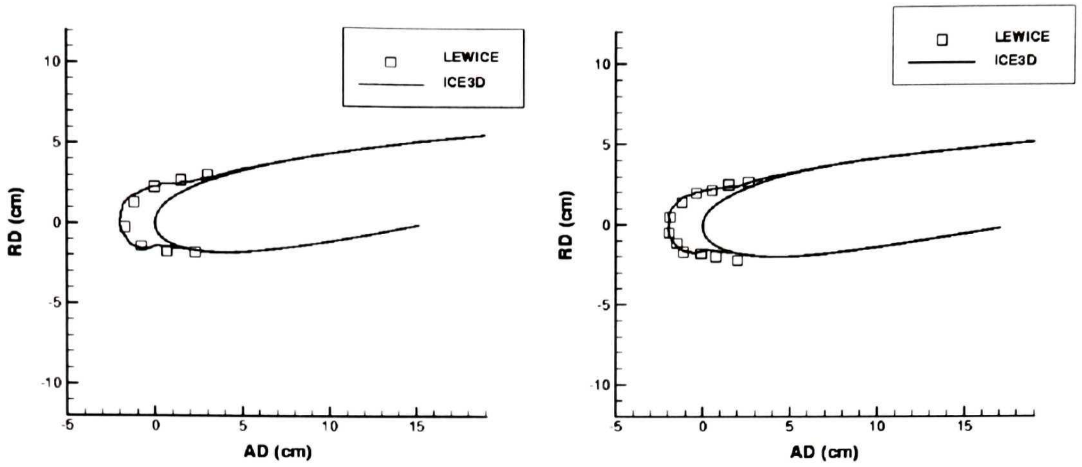

circumferential position: $\theta = 0°$ circumferential position: $\theta = 45°$

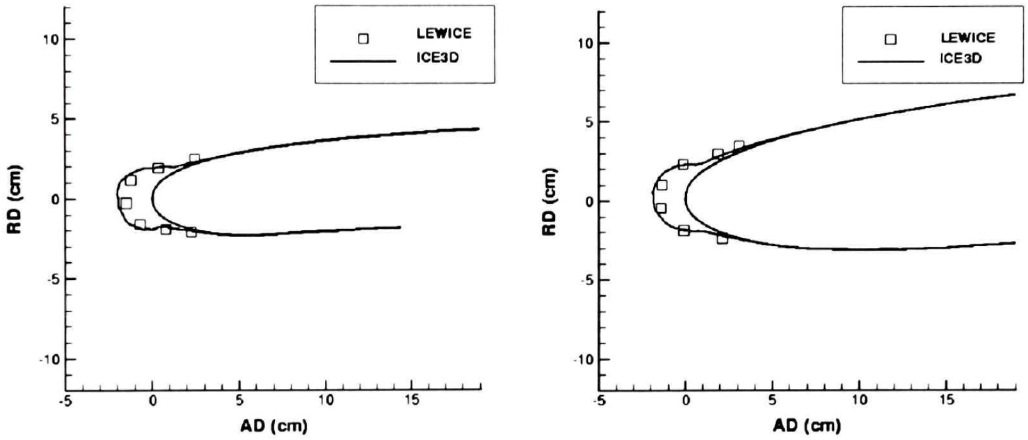

circumferential position: $\theta = 90°$ circumferential position: $\theta = 135°$

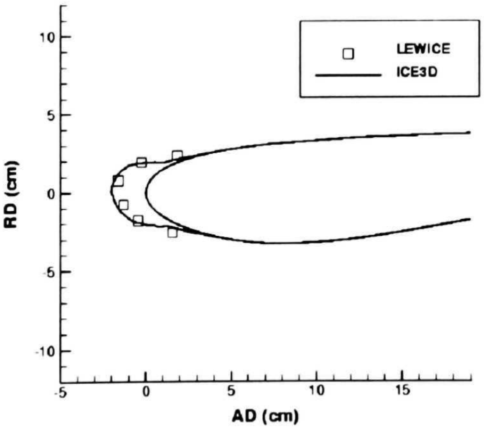

circumferential position: $\theta = 180°$

Figure 6.27: Rime ice for the Boeing 737-300 nacelle, 0° AoA, comparison between ICE3D-SWIM and LEWICE.

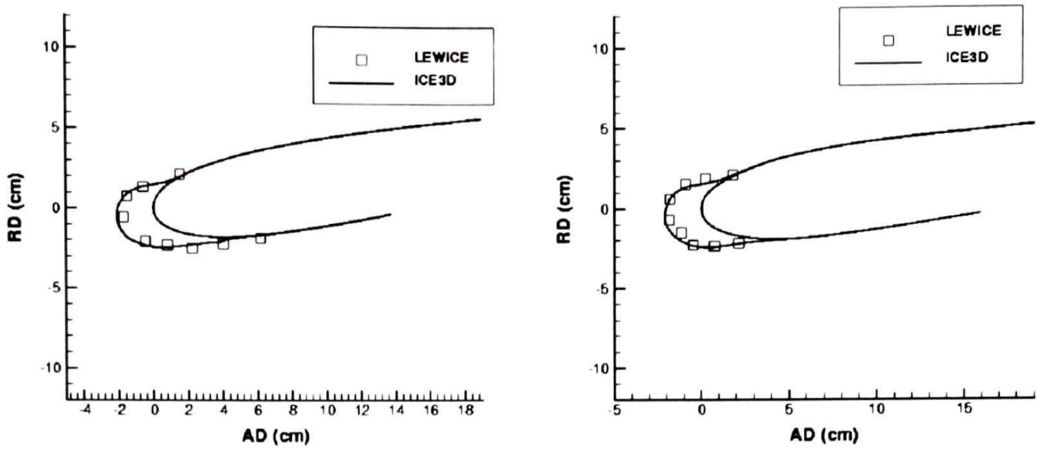

circumferential position: $\theta = 0°$ circumferential position: $\theta = 45°$

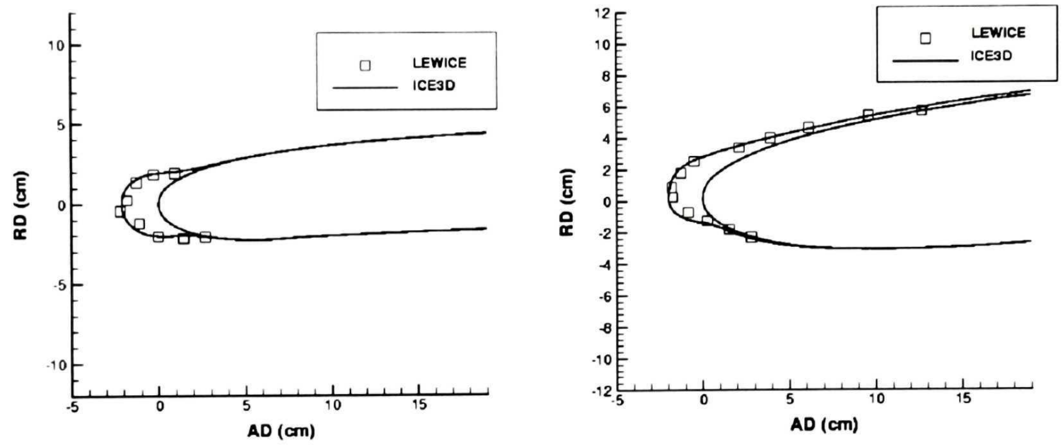

circumferential position: $\theta = 90°$ circumferential position: $\theta = 135°$

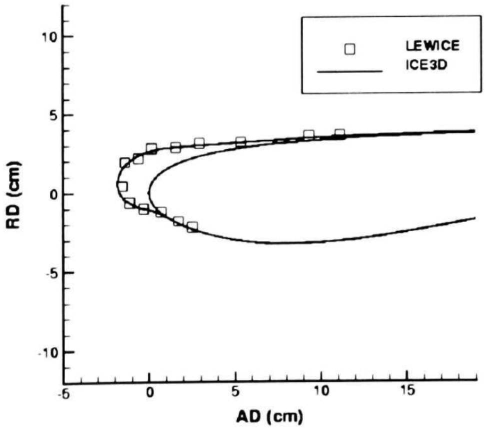

circumferential position: $\theta = 180°$

Figure 6.28: Rime ice for the Boeing 737-300 nacelle, 15° AoA, comparison between ICE3D-SWIM and LEWICE

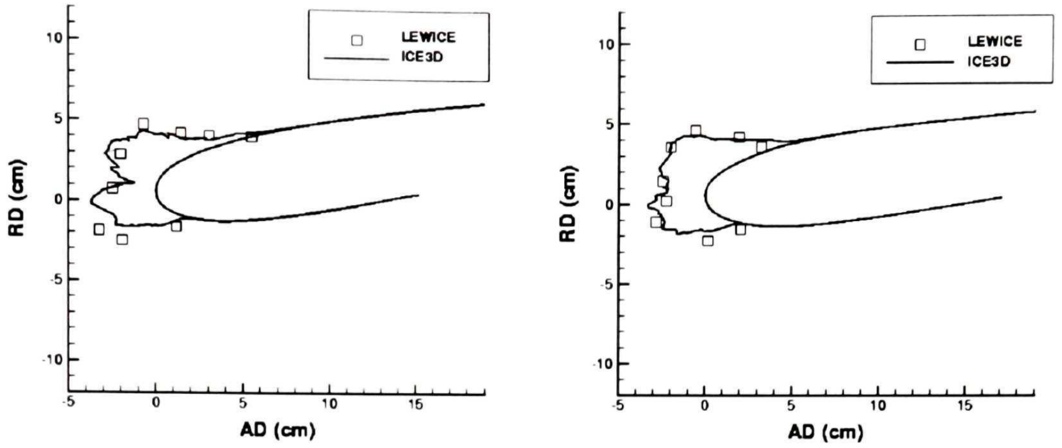

circumferential position: $\theta = 0°$ circumferential position: $\theta = 45°$

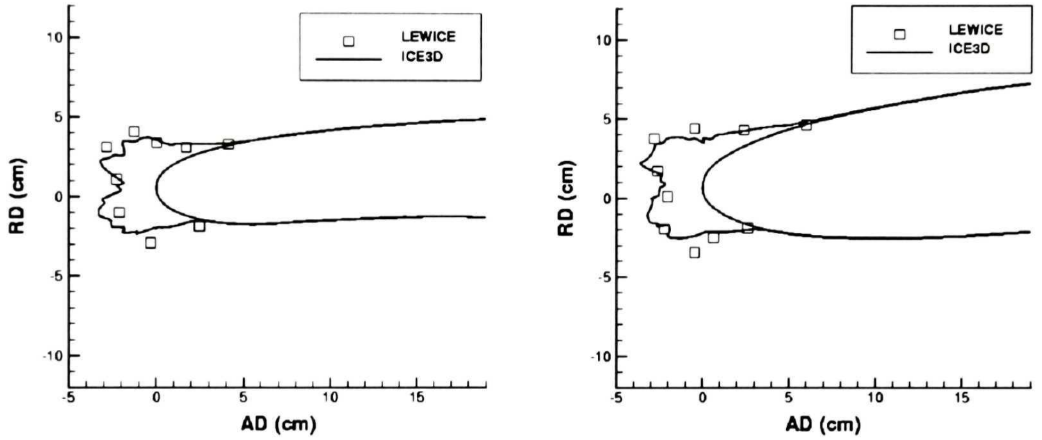

circumferential position: $\theta = 90°$ circumferential position: $\theta = 135°$

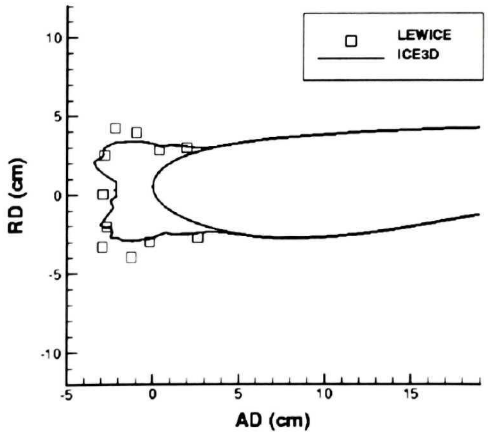

circumferential position: $\theta = 180°$

Figure 6.29: Glaze ice for the Boeing 737-300 nacelle, 0° AoA, comparison between ICE3D-SWIM and LEWICE.

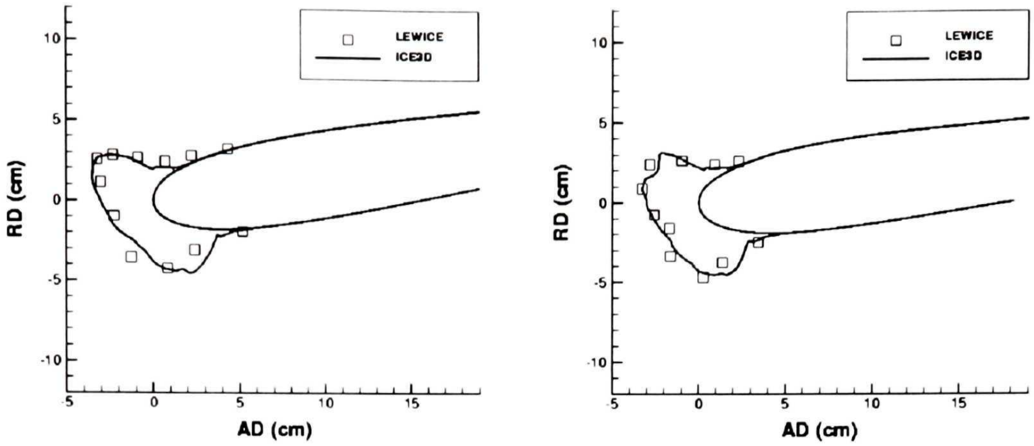

circumferential position: $\theta = 0°$ circumferential position: $\theta = 45°$

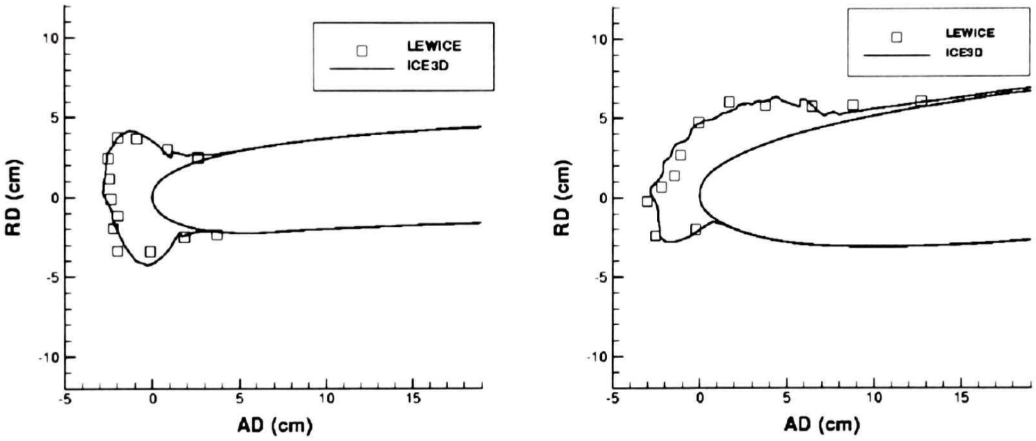

circumferential position: $\theta = 90°$ circumferential position: $\theta = 135°$

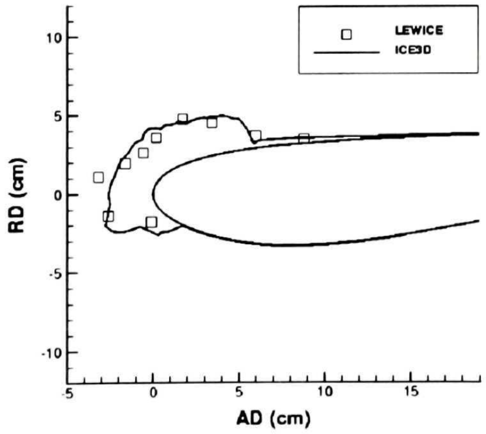

circumferential position: $\theta = 180°$

Figure 6.30: Glaze ice for the Boeing 737-300 nacelle, 15° AoA, comparison between ICE3D-SWIM and LEWICE.

6.2. Conclusions

A fully 3D ice accretion prediction has been completed on a 3D helicopter rotor blade tip and on a Boeing 737-300 nacelle inlet. ICE3D-SWIM yields a fully three-dimensional ice shape, as opposed to selected 2D cuts of a 3D geometry. The preliminary 3D validations of the proposed in-flight icing system are encouraging and should continue. Unfortunately, three-dimensional ice accretions with publicly available experimental results are still rare. Indeed, it would have been interesting to identify a test case as an installed system, with available experimental results, for which the three-dimensional features would be more pronounced.

Conclusions and Summary

Icing is a serious and not yet totally mastered meteorological hazard that may affect aircraft and helicopter operations. It is due to supercooled water droplets that impact on aerodynamic surfaces. Icing results in substantial performance penalties and flying qualities deterioration. During the in-flight icing certification process, manufacturers have to demonstrate that an airplane can fly into known icing conditions. Certification can be carried out through a combination of flight tests, wind and icing tunnel tests and tanker tests. Because not all the natural icing conditions required by the certification process can be explored during flight tests, shapes obtained from icing computer codes are manufactured from a light material and attached as disposable profiles on a test aircraft to investigate it for stability and control under icing.

It is evident that icing analysis methods that remain 2D and not based on CAD systems perpetuate the compartmentalization of the icing and aerodynamic activities and are not able to capitalize on the wealth of dry air solutions obtained by aerodynamicists at design time. Therefore, a new modular ice accretion tool and methodology based on modern CFD algorithms was long needed and its accretion part has been developed in the present thesis. The fundamental goal behind this work is the simplification of the aerospace industry's task by proposing a partial differential equations-based three-dimensional icing analysis procedure that uses a single mesh through all concurrent engineering processes, from aerodynamic analysis to manufacturing and performance degradations due to ice accretion on complex geometries, or complete aircraft. The objective has been reached. The approach suggested here views ice accretion simulation as:

- The solution of the 3D compressible turbulent Navier-Stokes equations;
- The computation of the collection efficiency by an Eulerian method (no particle has to be tracked through the mesh as in a Lagrangian method and the recovery of the collection efficiency on complex 3D geometries is done in an automatic way, without a painful determination of launching areas);
- The solution of the three-dimensional mass balance and heat transfer at the aerodynamic surface using partial differential equations.

The three modules are set in an interactive loop. Each system of PDEs (airflow / impingement / accretion) is solved independently, with selected variables exchanged and updated between modules when required. To complete this project many milestones have been reached.

First, in Chapter 3, the one-equation Spalart-Allmaras turbulence model has been implemented in the existing three-dimensional finite element flow solver. This model has been chosen for its robustness and its simplicity in use, to code and to impose transition. The high Reynolds number model, $k-\varepsilon$, was already available in the code. But the transition is not an easy task to impose inside a $k-\varepsilon$ model. Moreover, high-Reynolds number models require special mesh elements for the first layer off the wall.

The coding of the turbulence model has been verified by solving the boundary layer over a flat plate for different Reynolds numbers. To test the model in flow fields with pressure gradients and streamlines curvature, two transonic cases of flow over an airfoil RAE 2822 have been performed and the results compared to experimental data.

An important requirement to predict reliable ice shapes is to be able to model the roughness of the iced surface. The effects of surface roughness have been taken into account by the turbulence model and validated against numerical and experimental results. The skin friction coefficient has been compared to analytical results (Mills and Hang) for rough flat plates. The roughness calibration for convective heat fluxes on a rough flat plate has also been verified through comparison of the Stanton number with experiments performed by Blanchard. Velocity profiles distribution in rough pipes has also been compared to Nikuradse experiments.

Coming back to icing, roughness effects on ice shape have been demonstrated through some test cases on a NACA 0012 airfoil. Ice shapes computed with and without roughness have been compared to LEWICE and experimental ice shapes for the Run 209 of the NASA CD-ROM. The results show that roughness has a significant effect on ice accretion and that the Spalart-Allmaras model does an excellent job of modeling it. To conclude, this turbulence model appears to be robust and easy to use even with complex 3D geometries or complex flow patterns containing separations. The good agreement of the results with theory and experiments are encouraging and makes it a valuable tool for in-flight icing simulations.

In Chapter 4, a new three-dimensional equilibrium ice accretion model, based on PDEs, has been developed. For rime, glaze and mixed ice conditions this model predicts ice shapes on impacted surfaces, using the shear stress and the convective heat fluxes from the airflow solver and the water catch from the droplets solver. The model includes some features for continuous film runback prediction on two- and three-dimensional geometries and compatibility relations to ensure a physical solution and the well-posedness of the problem. By using a PDE-based model, a distinction can be made between the physical modeling and the numerical resolution of the icing phenomena. This allows the inclusion of time derivatives in the model, thus carefully accounting for unsteady effects of the underlying phenomena. An explicit numerical scheme using the finite volume method and based on a Roe scheme is derived to solve the problem.

No special mesh is needed to predict runback paths, as the present model predicts runback across lateral grid edges and can use the same mesh as the aerodynamic solution. One limitation of this model is that it considers the water film continuous. Indeed, sometimes in icing, the water film breaks down into rivulets and dry patches appear on the surface.

Another point to mention is that by doing large ice accretion simulations (to be able to compare with experiments) the effects of the unsteady terms are not visible. It would have been interesting to carefully study the effects of these unsteady terms accounted for by the time derivatives. This can be done by solving the ice accretion for the first few seconds of the phenomenon and taking into account unsteady parameters like the thermal inertia of the solid structure.

The CFD methodology (airflow/impingement/accretion modules) proposed in this work has been shown to be a comprehensive icing system for in-flight ice accretion simulations in three-dimensions, as well as in two dimensions.

This in-flight icing system has been shown to successfully predict ice shapes on two-dimensional symmetrical (NACA 0012, NASA Runs 209, 403, 404 and 308) and cambered (NLF 0414, NASA Run 623) airfoils (2D results are obtained on 3D meshes of one element thickness). For each test case of chapter 5, the ICE3D-SWIM ice shape is compared to LEWICE's numerical ice shape and the experimental one obtained in the IRT. These preliminary 2D validations are encouraging because ICE3D-SWIM shows good agreements with LEWICE and experiments. ICE3D-SWIM is able to predict ice shapes in rime and glaze ice situations. The complexity of details of the ice shape will increase if a finer grid is used and/or if a multi-stepping approach, with airflow and impingement updates, is selected to perform the simulation. Concerning CPU time, the overall process is not competitive for 2D calculations compared to the traditional two-dimensional ice accretion codes. While it is no more costly to test 3D geometries than 2D ones, it is much easier to find two-dimensional publicly available numerical and experimental results. The reason is simple: the non-existence of 3D ice simulation codes makes the exercise not of much use for comparison purposes. The 2D validation becomes then mandatory but cannot be, in such a time, as exhaustive as LEWICE validation for example.

Finally, the last step is to test the model for what it has been developed: 3D ice accretion predictions. For that, a 3D ice accretion prediction has been completed on a 3D helicopter rotor blade tip and on a Boeing 737-300 nacelle inlet, in Chapter 6. The objective is reached: the proposed ice accretion module yields a fully three-dimensional ice shape, as opposed to selected 2D cuts of a 3D geometry. The helicopter rotor blade tip demonstrates that it is possible to observe drastically different spanwise behavior of the ice accretion process, on a single geometry. For the Boeing 737-300 nacelle inlet, it is comforting that the results obtained by the two codes, ICE3D-SWIM and LEWICE3D, are in good agreement and look consistent with the conditions for which the shapes were generated and with the airflow and droplet solutions.

These preliminary 3D results of the proposed in-flight icing system are encouraging and should continue. Unfortunately, three-dimensional ice accretions with publicly available experimental results are still rare.

To simplify the three-dimensional process when the multi-stepping approach is used an automatic mesh movement will be coupled to the ice accretion module, so that even large and complex 3D ice shapes will be automatically meshed.

It is generally observed that wind tunnel experimental ice shape limits on the pressure side of the airfoil are further than those predicted by numerical codes. This phenomenon requires some investigations to be explained. This discrepancy between the numerical results and experiments may be due to:

- The fact that droplet diameter distributions exist in the wind tunnel and are not monodispersed;
- Wind tunnel blocking effects;
- The absence of rivulets modeling.

An interesting challenge facing an ice accretion code is the simulation of scallop ice. Indeed some ice shapes characteristics, like the scalloping effects that are not predictable by any icing code currently, seem to be partially due to 3D flow patterns. At least this physical phenomenon is observed on finite or infinite swept wings not on airfoils. The in-flight icing system, proposed into this work, being truly 3D, it will be interesting, after the thesis, to try to capture this type of ice shapes.

A natural evolution of a numerical icing code is the addition of anti- or de-icing capabilities inside the thermodynamic ice accretion module. Today, computer codes are used to predict or optimize the protection efficiency of thermal anti-(de-)icing systems. In other words, for an imposed thermal heat flux distribution, the ice accretion code should be able to determine if any ice is forming on a given geometry. Further developments of the runback model will be required for that, like criteria for the break-up of thin liquid film and the creation of rivulets. The partial differential equation expressing the energy conservation also has to be modified as the conduction through the metal skin and the ice/water layer becomes an important factor in this case. To properly model the conduction through the solid structure, special care has to be taken since the external solid wall boundary condition will depend on the surface state (dry, wet, iced, or melted: liquid water + ice).

References

[1] Kind R.J., "Icing, frost and aircraft flight", *Canadian Aeronautics and Space Journal,* Vol. 4, N°2, pp 110-118, June 1998.

[2] Brunet L., "Conception et Discussion d'un modèle de Formation du givre sur des Obstacles Varies", *Rapport interne de l'ONERA*, 1985.

[3] Guffond D., "Le Givrage des Aéronefs", *Revue l'aéronautique et l'Astronautique*, Edition Spéciale : Salon du Bourget, No 148 et 149, pp. 51-54, 1991.

[4] Wright W.B., "Simulation of Two-Dimensional Icing, De-Icing and Anti-Icing Phenomena", Ph.D. thesis, University of Toledo, December 1991.

[5] Al-Khalil K. M, Keith T.G., and De Witt K.J., "Further Development of an Anti-Icing Runback Model", AIAA Paper 91-0266, Reno, January 1991.

[6] Morency F., "Simulation Numérique d'un Système Antigivre pour les Ailes d'Avions", thèse de doctorat de l'Université de Montréal, École Polytechnique de Montréal, 1999.

[7] Henry R., Guffond D., Aschettino S. and Duprat G., "Characterization of Ice Roughness and Influence on Aerodynamic Performance of Simulated ice Shapes", *AIAA Paper 2001-0092*, Reno, January 2001.

[8] Wright William B., "Advancements in the LEWICE Ice Accretion Model", *AIAA Paper 93-0171*, Reno, January 1993.

[9] Brahimi M.T., Tran P., Paraschivoiu I. and Tezok F., "Prediction of Ice Accretion on Supercritical and Multi-Element Airfoils", AIAA Paper 95-0754, Reno, January 1995.

[10] Gent R.W., "Ice accretion prediction on aerofoils", *1er Colloque International Bombardier*, École Polytechnique de Montréal, Québec, Septembre 1993.

[11] Mingione G., Brandi V. and Saporiti A., "A 3D Ice Accretion Simulation Code", *AIAA Paper 99-0247*, Reno, January 1999.

[12] Mingione G. and Brandi V., "Ice Accretion Prediction on Multielement Airfoils", *Journal of Aircraft*, Vol. 35, No. 2, March-April 1998.

---

[13] Lynch F.T., Khodadoust A., "Effects of ice accretions on aircraft aerodynamics", *Progress in Aerospace Sciences 37* pp 669-767, 2001.

[14] Ruff G.A. and Berkowitz B.M., "Users Manual for the NASA Lewis Ice Accretion Prediction Code (LEWICE)", *NASA Contractor Report 185129*, May 1990.

[15] Hedde T., "Modélisation tridimensionnelle des dépôts de givre sur les voilures d'aéronefs", *thèse de doctorat*, Université Blaise-Pascal, Clermont-Ferrand II, 1992.

[16] Myers T.G., Charpin J.P.F. and Thompson C.P., "Slowly accreting ice due to Supercooled Water Impacting on a Cold Surface", *Journal of Physics of Fluids*, Volume 14, No 1, January 2002.

[17] Brahimi M.T., Tran P. and Paraschivoiu I., "Numerical Simulation and Thermodynamic Analysis of Ice Accretion on Aircraft Wings", Projet C.D.T. C159 for Bombardier/Canadair Aerospace Group, May 1994.

[18] Wright W.B., Gent R.W. and Guffond D., "DRA/NASA/ONERA Collaboration on Icing Research" part II - Prediction of Airfoil ice Accretion, *NASA Technical Reports*, NASA-CR-202349, May 1997.

[19] Anderson J.D., "Fundamentals of Aerodynamics", McGraw-Hill.

[20] Wirz H.J. and Smolderen J.J., "Numerical Methods in Fluid Dynamics", A von Karman Institute Book, *McGraw-Hill Bokk Company*, chapter 4.

[21] Bidwell C., Pinella D. and Garrison P., "Ice Accretion Calculations for a Commercial Transport Using the LEWICE3D, ICEGRID3D and CMARC Programs", *AIAA Paper 99-0250*, Reno, January 1999.

[22] Cebeci T. and Besnard E., "Progress Towards the Prediction of the Aerodynamic Performance Degradation of an Aircraft in Natural Icing Conditions", the First Bombardier International Workshop Aircraft Icing/Boundary Layer Stability and Transition pp 57-85, Montréal, CANADA, 20-21/09/1993.

[23] Hedde T. and Guffond D., "ONERA Three-Dimensional Icing Model", *AIAA Journal, Vol. 33, No. 6*, June 1995.

[24] Von Doenhoff A.E. and Horton E.A., "Low-Speed Experimental Investigation of the Effect of Sandpaper Type of Roughness on Boundary-Layer Transition", *NACA TN 3858*, 1956.

[25] White F.M., "*Viscous Fluid Flow*", McGraw-Hill, Inc, 1974.

[26] Kays W.M. and Crawford M.E., "*Convective Heat and Mass Transfer*", 2nd Edition, MacGraw-Hill Book Company, New York, 1980.

[27] Hobbs P.V., "Ice Physics", *Oxford University Press*, Ely House, London, 1974.

[28] Messinger B.L., "Equilibrium Temperature of an Unheated Icing Surface as a Function of Air Speed", Journal of the Aeronautical Sciences, Vol. 20, No. 1, pp. 29-42, 1953.

[29] Sogin H.H., "A Design Manual for Thermal Anti-Icing Systems", *Wright Air Development Center (WADC) Technical Report 54-313*, 1954.

[30] Lozowski E.P., Stallabrass J.R., and Hearty, P.F. "The Icing of an Unheated Non-rotating Cylinder in Liquid Water Droplet-Ice Crystal Clouds", *National Research Council of Canada (NRC) Report LTR-LT-96*, 1979.

[31] Cansdale J.T. and Gent R.W., "Ice Accretion on Aerofoils in Two-Dimensional Compressible Flow – A Theoretical Model", *Royal Aircraft Establishment Technical Report 82128*, 1983.

[32] Baruzzi G.S., Habashi W.G., Guèvremont G. and Hafez M.M., " A Second Order Finite Element Method for the Solution of the Transonic Euler and Navier-Stokes Equations", *International Journal for Numerical Methods in Fluids*, Vol. 20, pp. 671-693, 1995.

[33] Tsao J., "Cross Flow Effects on Glaze Ice Roughness Formation", AIAA Paper 2003-1219, Reno, January 2003.

[34] Potapczuck M.G., Papadakis M. and Vargas M., "LEWICE Modeling of Swept Wing Ice Accretions", AIAA Paper 2003-0730, Reno, January 2003.

[35] Bourgault Y., Habashi W.G., Dompierre J. and Baruzzi G.S., "A Finite Element Mothod Study of Eulerian Droplets Impingement Models", *International Journal for Numerical Methods in Fluids*, Vol.29, pp. 429-449, 1999.

[36] Boutanios Z., Bourgault Y., Habashi W.G., Isaac G.A. and Cober S.G.,"3-D Droplets Impingement Analysis Around an Aircraft's Nose and Cockpit Using FENSAP-ICE", AIAA Paper 98-0200, Reno, January 1998.

[37] Crowe C.T., "Review-Numerical models for dilute gas-particle flows", *Trans. ASME, J. Fluids Engin.*, 104: pp. 297-303, 1982.

[38] Hughes T.J.R. and Brooks A., "A theoretical Framework for Petrov-Galerkin Methods with Discontinuous Weighting Functions: Application to the Streamline-Upwind Procedure", Finite Elements in

Fluids, Volume 4, Chapter 3, Edited by R.H. Gallagher, D.H. Norrie, J.T. Oden and O.C. Zienkiewicz John Wiley, 1982.

[39] Morency F., Beaugendre H. and Habashi W.G., "Effect of Pressure Gradient on Eulerian Droplet Impingement Models", the 10th Annual Conference of the CFD Society of Canada, Windsor, pp 299-304, June 2002.

[40] Wilcox D.C., "Turbulence Modeling: An Overview", *AIAA paper* 2001-0724, 2001.

[41] Hellsten A., Rautaheimo P., *Proceedings*, "8th ERCOFTAC/IAHR/COST Workshop on Refined Turbulence Modelling", Report 127, 17-18 June, 1999, Helsinki University of Technology.

[42] Lepage C., "A Guide to FENSAP" Version 7.1, July 2000.

[43] Spalart P.R. and Allmaras S.R., "A One-Equation Turbulence Model for Aerodynamic Flows" *AIAA Paper* 92-0439, 1992.

[44] Hellsten A., " Implementation of a One-Equation Turbulence Model into the FINFLO Flow Solver", *Report No B-49, Series B*, 1996.

[45] Remaki L., Beaugendre H. and W.G. Habashi, "ISOD, An Anisotropic Isovalue-Oriented Diffusion Artificial Viscosity for the Euler and Navier-Stokes Equations", *Journal of Computational Physics*, VOL. 186, No. 1 pp. 279-294, 2003.

[46] Coles D.E. and Hirst E.A., "Computation of Turbulent Boundary Layers-1968" AFOSR-IFP-Stanford Conference, Vol. II, Stanford Univ. Press, Stanford, CA, 1969.

[47] Spalart P.R., "Trends in turbulence treatments", *AIAA Paper* 2000-2306, 2000.

[48] Hellsten A. and Laine S., "Extension of the $k-\omega$-SSt Turbulence Model For Flows Over Rough Surfaces", *AIAA paper 97-3577*, 1997.

[49] Blanchard A., "Analyse Expérimentale et Théorique de la structure de la Turbulence d'une Couche Limite sur Paroi Rugueuse", *Ph.D. thesis*, Université de Poitiers, France, U.E.R.-E.N.S.M.A. 1997.

[50] Aupoix B. and Spalart P.R., "Extensions of the Spalart-Allmaras Turbulence Model to Account for Wall Roughness", *ONERA/DMAE*, 2002.

[51] Schlichting H., "Boundary-Layer Theory", sixth Edition, *McGRAW-HILL BOOK COMPANY*, 1968, Chapter 20, p. 581.

---

[52] Henry R.C., Guffond D., Bouveret A. and Gardette G., "Heat Transfer Coefficient Measurement on Iced Airfoil in a Small Icing Wind Tunnel", *AIAA Paper 99-0372*, Reno, January 1999.

[53] Makkonen L., "Heat Transfer and Icing of a Rough Cylinder", *Cold Regions Science and Technology*, Elsevier Science Publishers B.V., Amsterdam, pp 105-116, 1985.

[54] Bourgault Y., Beaugendre H., Habashi W.G., "Development of a Shallow-Water Icing Model in FENSAP-ICE", *Journal of Aircraft*, Volume 37, N°4, July-August 2000.

[55] Morency F., Tezok F. and Paraschivoiu I., "Anti-icing System Simulation Using CANICE", *Journal of Aircraft*, Vol. 36, pp. 999-1006, November-December 1999.

[56] MacArthur C.D., Keller J.L. and Luers J.K., "Mathematical Modeling of Ice Accretion on airfoils", *AIAA 20th Aerospace Sciences Meeting*, January 11-14, 1982.

[57] Pueyo A., "Simulation Numérique de la Format ion de la Glace pour des Ecoulements Tridimensionnels ", Thèse, École Polytechnique, Université de Montréal, juillet 1992.

[58] Meyer C.A., "ASME Steam Tables", New York, *American Society of Mechanical Engineers*, 6th edition, 1993.

[59] Ruff G.A. and Berkowitz M., "Users Manual for the NASA Lewis Ice Accretion Prediction Code (LEWICE)", NASA Contractor Report 185129, May 1990.

[60] Hirsch Ch., "Numerical Computation of Internal and External Flows", volume 2: "Computational Methods for Inviscid and Viscous Flows", John Wiley & sons, 1988.

[61] Toro E.F., "Riemann Solvers and Numerical Methods for Fluid Dynamics, A Practical Introduction", Springer, 1999.

[62] Roe P.L., "Approximate Riemann Solvers, Parameter Vectors, and Difference Schemes", Journal of Computational Physics, Vol. 43, pp357-372, 1981.

[63] Bertsekas, D., "Nonlinear Programming", Athena Scientific, Belmont, Mass, 1995, p. 780.

[64] Ciarlet P.G., "Introduction à l'analyse matricielle et à l'optimisation", *Masson*, 1989.

[65] Glowinski R., "Numerical Methods for Nonlinear Variational Problems", *Springer-Verlag*, 1984.

[66] Wright W.B. and Rutkowski A., "Validation Results for LEWICE 2.0" and CD-ROM, January 1999.

---

[67] SAE Recommended Practice for Droplet Impingement and Ice Accretion Computer Codes, *ARP5903*, 2003.

[68] Kind R.J., "Ice Accretion Simulation Evaluation Test", NATO RTO Technical Report 38, *RTO-TR-038*, France, November 2001.

[69] Ruff G.A. and Anderson D.N., "Quantification of Ice Accretions for Icing Scaling Evaluations", *AIAA Paper 98-0195*, Reno, January 1998.

[70] Wright W.B, "A Summary of Validation Results for LEWICE 2.0", *AIAA Paper 99-0249*, Reno, January 1999.

[71] Beaugendre H., Morency F. and Habashi W.G., "FENSAP-ICE's Three-Dimensional In-Flight Ice Accretion Module: ICE3D", *Journal of aircraft*, Vol. 40, No. 3, May-June 2003 (Tentative).

[72] Bidwell C.S., "Collection Efficiency and Ice Accretion Calculations for a Boeing 737-300 Inlet", *SAE 965570*, 1996.

[73] Beaugendre H., Morency F. and Habashi W.G., "FENSAP-ICE: Roughness Effects on Ice Shape Prediction", *AIAA Paper 2003-1222*, Reno, January 2003.

[74] Lepage C.Y., Suerich-Gulick F., and Habashi W.G., "Anisotropic 3D Mesh Adaptation on Unstructured Hybrid Meshes", *AIAA Paper 2002-0859*, January 2002.

[75] Papadakis M., Elangonan R., Freund G.A., Breer Jr., M., Zumwalt, G.W. and Whitmer L., "An Experimental Method for Measuring Water Droplet Impingement Efficiency on Two- and Three-Dimensional Bodies", NASA CR-4257, DOT/FAA/CT-87/22, November 1989.

[76] Tran P., Benquet P., Baruzzi G., and Habashi W.G., " Design of Ice Protection Systems and Icing Certification Through Cost-Effective Use of CFD", *AIAA Paper 2002-0382*, Reno, January 2002.

[77] Papadakis M., Breer M., Craig N. and Liu X., " Experimental Water Droplet Impingement Data on Airfoils, Simulated Ice Shapes, an Engine Inlet and a finite Wing", *NASA Contractor Report 4636*, 1994.

Appendix

Boeing 737-300 inlet nacelle

A variety of test models and conditions were selected for the Boeing 737-300 inlet to provide an extensive data base. According to NASA[75], the engine inlet angle of attack was limited to 15 degrees to keep the inlet models well within the uniformity region of the IRT tunnel. The installation of the nacelle inside the tunnel is shown in figure A.1.

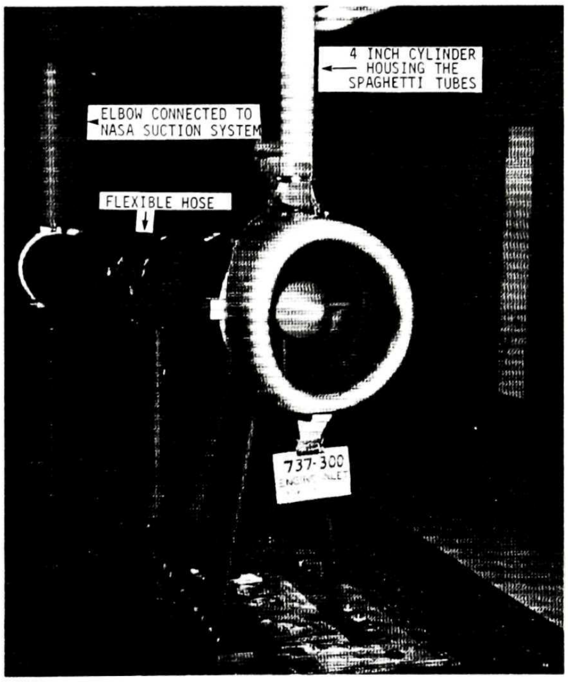

Figure A.1: Installation of Boeing 737-300 inlet in the IRT test section (Ref. 75).

The spray pressure ratios chosen correspond to water droplet clouds which are representative of realistic icing cloud conditions. Blotter paper strips are used experimentally to measure the local collection efficiency. Their location on the nacelle is shown in figure A.2.

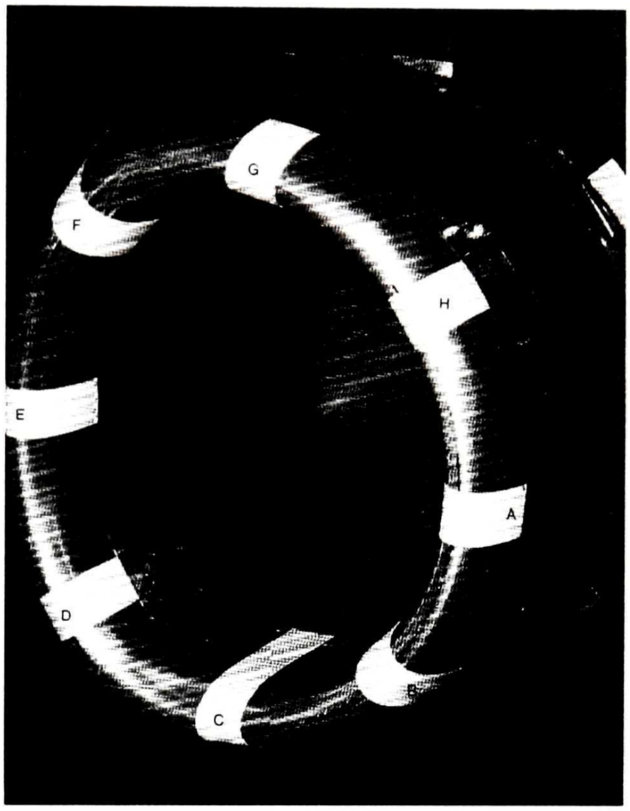

Figure A.2: Blotter strip locations on Boeing 737-300 inlet for 0 deg and 15 deg AoA (Ref. 75).

In the paper by Tran *et al.*[76] the solutions obtain with FENSAP has been compared to experimental data and LEWICE solution. The results of these comparisons are presented in figures A.3 and A.4. For all circumferential cuts and both incidence, the FENSAP solution agrees very well with LEWICE solution and experiments.

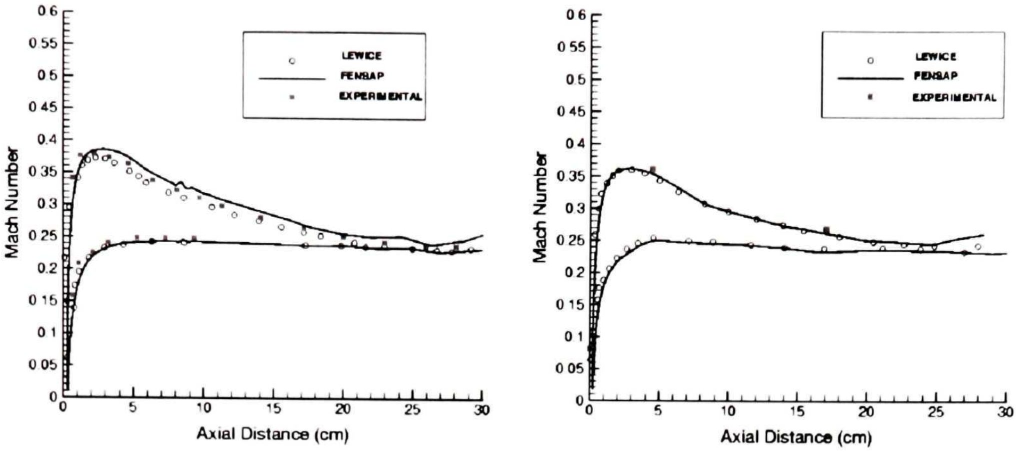

circumferential position: $\theta = 0°$ circumferential position: $\theta = 45°$

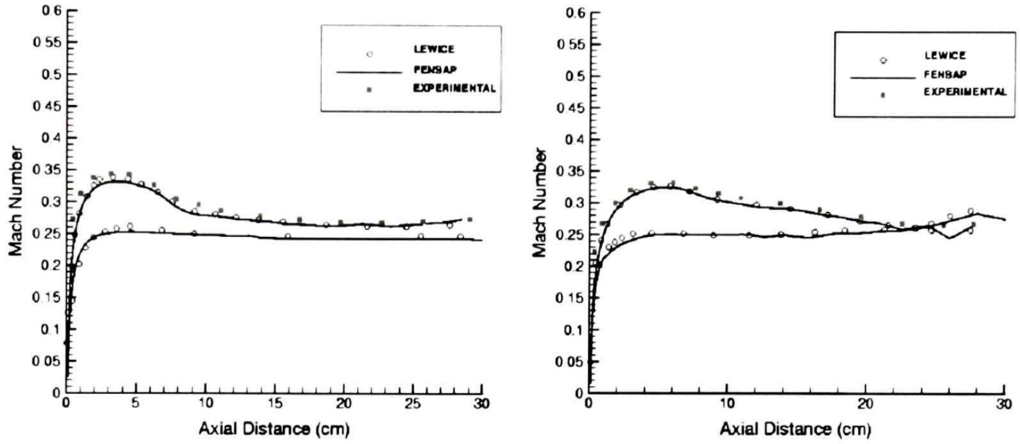

circumferential position: $\theta = 90°$ circumferential position: $\theta = 135°$

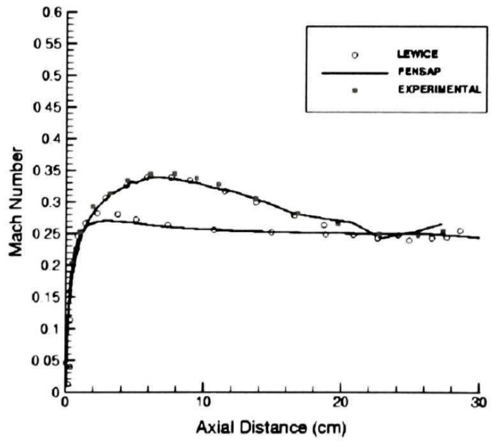

circumferential position: $\theta = 180°$

Figure A.3: Mach number distribution for the Boeing 737-300 inlet for 0 deg AoA and an inlet mass flow rate of 10.4 kg/s, comparison between FENSAP, LEWICE and Experiments.

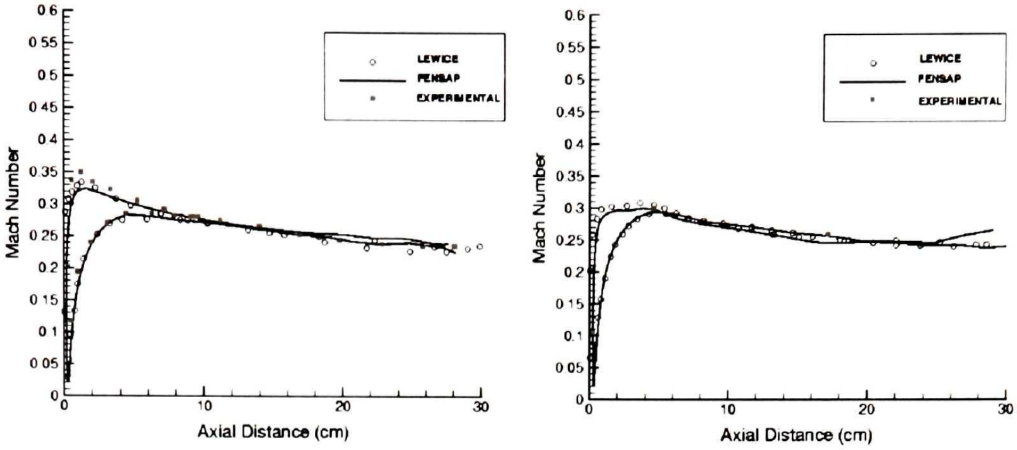

circumferential position: $\theta = 0°$ circumferential position: $\theta = 45°$

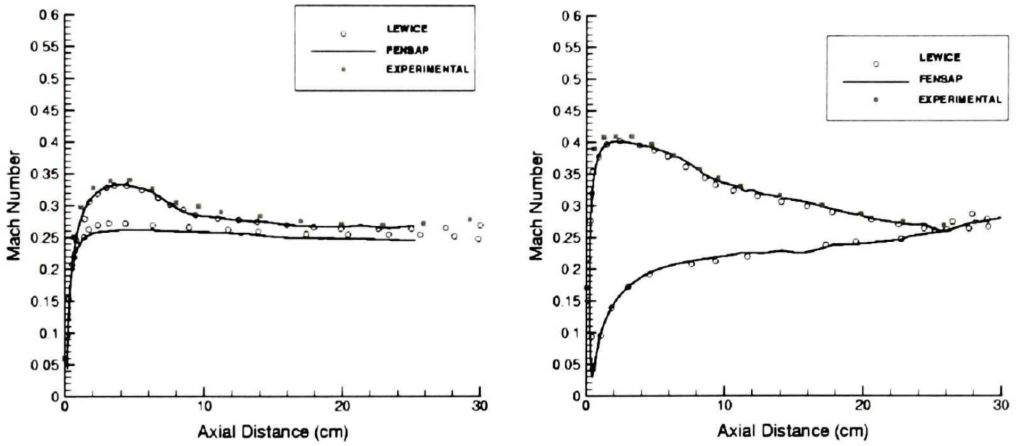

circumferential position: $\theta = 90°$ circumferential position: $\theta = 135°$

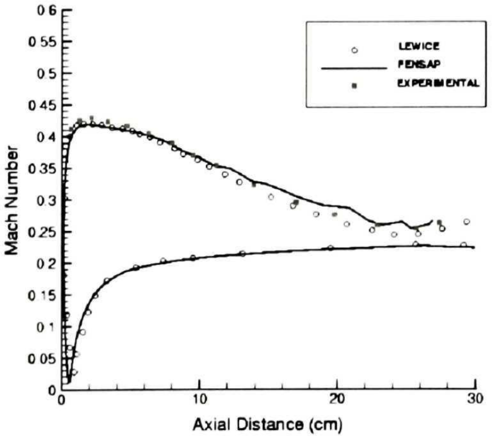

circumferential position: $\theta = 180°$

Figure A.4: Mach number distribution for the Boeing 737-300 inlet for 15 deg AoA and an inlet mass flow rate of 10.4 kg/s, comparison between FENSAP, LEWICE and Experiments.